

國立交通大學

材料科學與工程學系

博士論文

新穎仿生奈米材料三部曲：

蛾眼結構、壁虎膠帶和玫瑰花瓣表面

A Trilogy of Novel Biomimetic Nanomaterials:

Moth Eye Structures, Gecko Tapes

and Rose Petal Surfaces

研究生：吳佳典

Chia-Tien Wu

指導教授：柯富祥

Fu-Hsiang Ko

中華民國一百年三月

新穎仿生奈米材料三部曲：

蛾眼結構、壁虎膠帶和玫瑰花瓣表面

A Trilogy of Novel Biomimetic Nanomaterials:

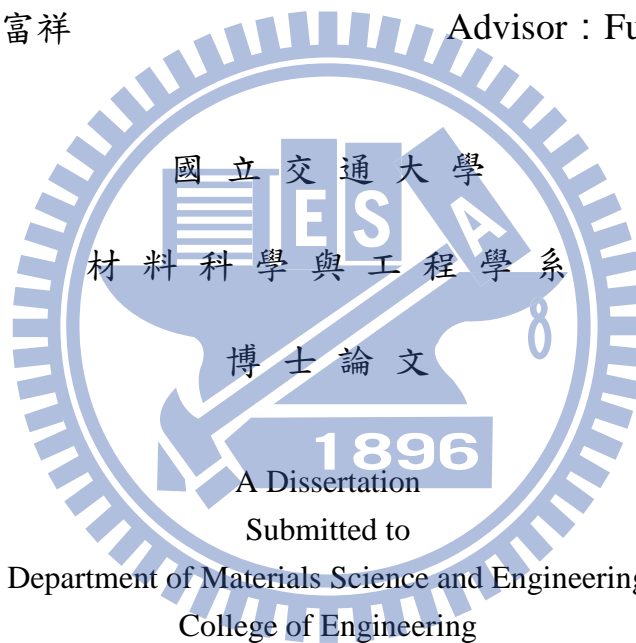
Moth Eye Structures, Gecko Tapes and Rose Petal Surfaces

研究生：吳佳典

Student : Chia-Tien Wu

指導教授：柯富祥

Advisor : Fu-Hsiang Ko



Department of Materials Science and Engineering
College of Engineering

National Chiao Tung University

in partial Fulfillment of the Requirements

for the Degree of

Doctor of Philosophy in

Materials Science and Engineering

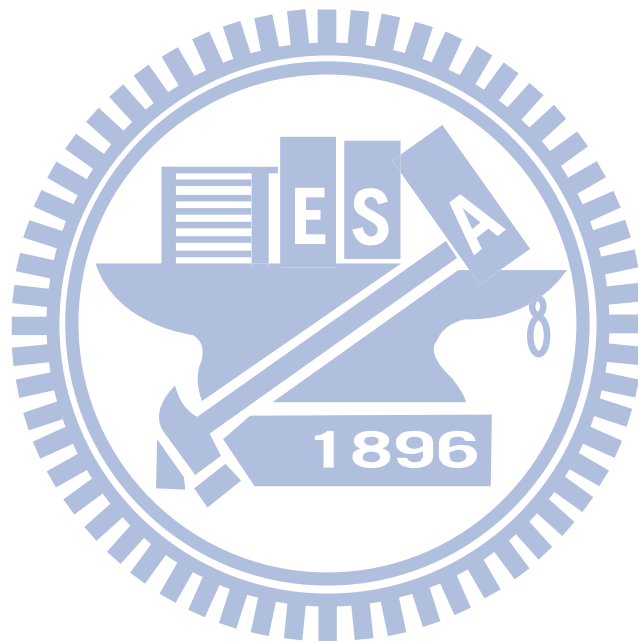
March 2011

Hsinchu, Taiwan, Republic of China

中華民國一百年三月

Acknowledgment

『因為需要感謝的人太多了，就感謝天吧。無論什麼事，不是需要先人的遺愛與遺產，即是需要眾人的支持與合作，還要等候機會的到來。越是真正做過一點事，越是感覺自己的貢獻之渺小。』



新穎仿生奈米材料三部曲：

蛾眼結構、壁虎膠帶和玫瑰花瓣表面

研究生：吳佳典

指導教授：柯富祥

國立交通大學材料科學與工程學系

摘要

仿生科技近年來成為研究材料科學一個熱門的領域。科學家透過模仿大自然的生物研究出各種具有不同功能的人造材料，其效能甚至遠高於自然本身所具備的。在本篇論文中，我們提出三種新穎的功能性仿生奈米材料起源於蛾眼結構、壁虎腳和玫瑰花瓣。

蛾眼是由約300奈米高和間隔的突起物所組成之類最密堆積結構，可以有效地降低其反射率。因此，我們將金屬沉積在鋁和基板之中，利用陽極氧化的方式處理，這層金屬也會隨之氧化而形成奈米結構點狀陣列，有如蛾眼結構。並且我們可操控這些結構，由空心到實心，或由半球形到錐狀的陣列。利用這些次波長的奈米錐狀陣列，我們可以應用在不同的基本上形成抗反射層對於任何角度的入射光，並具有良好的機械性質。此外，這種空心的錐狀結構也被我們拿來開發成新穎的光電極結構並應用在增進染敏太陽能電池的效率。透過自主裝的二氧化鈦空心錐狀陣列和二氧化鈦奈米管壁並用陽極氧化鋁相互隔開已經被我們沉積在在導電透明基板上。此種結構應用在染敏電池上可以增加染料接觸面積、提供更直接的電子傳輸路徑並能降低電子電洞的的復合，因此可提升光電轉化之效率。

由壁虎腳所引起的乾式黏附力已引起了各界的關注，透過表面的粗糙度和指向性的改變，使其擁有強大的黏附力和微弱的脫附力且可重複使用為其迷人之處。近來，關於壁虎腳的仿生結構在理論及實驗方面的研究已被相繼提出。然而，這

些研究與自然的壁虎相比之下，有著受限於材料方面的缺點；但在我們的研究中，我們設計了一有效的方法來製作出創新的結構來更符合理想的乾式吸附力。我們首次提出，以去耦兩階段硬式陽極氧化的方式，來製作出長1.3微米、直徑380奈米的錐形陽極氧化鋁模板；經過翻模的過程後，得到了具有傾斜角度的錐狀奈米陣列。此錐狀奈米陣列在大面積的表現上具備了出色的方向性、可重複使用性及水潔淨的特性。與一般的柱狀奈米陣列相比，錐狀奈米陣列有更好的穩定性和自潔淨的特性。藉由錐狀奈米陣列在各具方向性的力上亦有出色的表現：剪力可達到每平方公分8牛頓之強，而反方向的脫附力卻僅需要每平方公分1.4牛頓。

不同於蓮葉效應，最近幾年科學家被玫瑰花表面所深深吸引，其表面具有超疏水的特性和高水滴吸附力。此種現象是由花瓣上面微米尺度的凸起和奈米結構所產生。直至今日，許多研究者仍對如何去製造出此等複雜的結構並使其應用而感到困擾。我們發展出一種由下而上的方法：藉由簡單的酸雕刻技術來製作具有高水滴吸附力和自潔淨特性的超疏水聚二甲基矽氧烷(PDMS)。此類花瓣的聚二甲基矽氧烷其有30微米的寬度、奈米皺褶約在500奈米和小於100奈米的奈米結構。在長時間的檢測下，其也能展現大於150度的水滴接觸角。更甚者，此類花瓣展現了高水滴吸附力達到 35.8 N/m^2 。除此之外，從酸雕刻技術得來的兩種超疏水表面讓我們得以用來製造一個新型無殘留的印章。其超疏水且對水滴具吸附力的區域可用於將染料從印章轉移至紙上。而超疏水具備自潔淨的區域可以避免染料沾附上去。

**A Trilogy of Novel Biomimetic Nanomaterials:
Moth Eye Structures, Gecko Tapes and Rose Petal Surfaces**

Student: Chia-Tien Wu

Advisor: Fu-Hsiang Ko

Department of Materials Science and Engineering
National Chiao Tung University

Abstract

Biomimetics is a freshly explored area of materials science that deals with the science of copying or improving upon that which is found in nature. Scientists commonly produce artificial materials with properties that improved from what occurs naturally. In this thesis, we demonstrate three types of novel functional nanomaterials inspired by moth eyes, gecko feet and rose petals.

Moth eyes consist of quasi-close-packed nipples having heights and spacings typically of less than 300 nm, which reduces reflection from their compound eyes. We found, a metal whose oxide form has a higher ionic conductivity than alumina was used as an underlayer preceding an Al anodization process, the underlying metal would be also oxidized and thereby form metal–oxide nanostructures as Moth-eye structures. We modulate the metal–oxide nanomaterials to form, hollow-to-solid and hemisphere-to-cone nanostructure arrays. We employ subwavelength nanocone arrays as Moth-eyes structures for high-performance antireflection coatings. These oxide nanostructures greatly suppress reflectance over a large range of wavelengths and angles of incidence and display a good mechanical stability. Also, we introduce these

nanocones as a new photoelectrode architecture for improved efficiency of dye-sensitized solar cells (DSSCs). A facile synthesis of self-organized hollow TiO₂ nanocones under porous anodic alumina (PAA) featuring TiO₂ nanotubes (NTs) within was grown directly on a fluorine-doped tin oxide (FTO) substrate. The novel structure combines two types of TiO₂ materials—0-D nanocones and 1-D NTs—to benefits from a large contact area, direct electron transport path, and slow recombination of electrons.

A gecko is the largest animal that can produce high dry-adhesion to support its weight with a high factor of safety. The secret of the gecko's adhesive properties lies in the hairy microstructure and nanostructure of gecko feet. We designed the efficient method of an innovate structure for ideal dry adhesives. A taper anodic alumina oxide mold with a length of 1.3 μm and a diameter of 380 nm was fabricated using decoupling two-step hard-anodization process which was firstly reported by us. After molding, taper-shaped nanohair array with slanted angle was presented. The approach to fabricate angled taper nanohair arrays obtained an excellent directional, reusable, and water cleanable use in large area. A remarkably directional force exhibited by angled taper nanohair arrays was showing here with strong shear attachment (8 N/cm²) in the gripping direction and easy releasing (1.4 N/cm²) in the reverse direction.

Unlike “Lotus effect”, the petal's surface which has superhydrophobicity and high water adhesion was fascinated by scientists in recent years. The phenomenon is induced by the microscale convex and nanostructures upon the petal. To mimic the petal's surface, we developed a bottom-up method by the simple acid texture technique to fabricate the superhydrophobic PDMS surface with high water adhesion and self-cleaning ability. The resulting petal-like PDMS had convexes about 30 μm in diameter, nanowrinkles around 500 nm in width and nanostructures less than 100 nm. A high water contact angle larger than 150° was displayed. Moreover, the petal-like

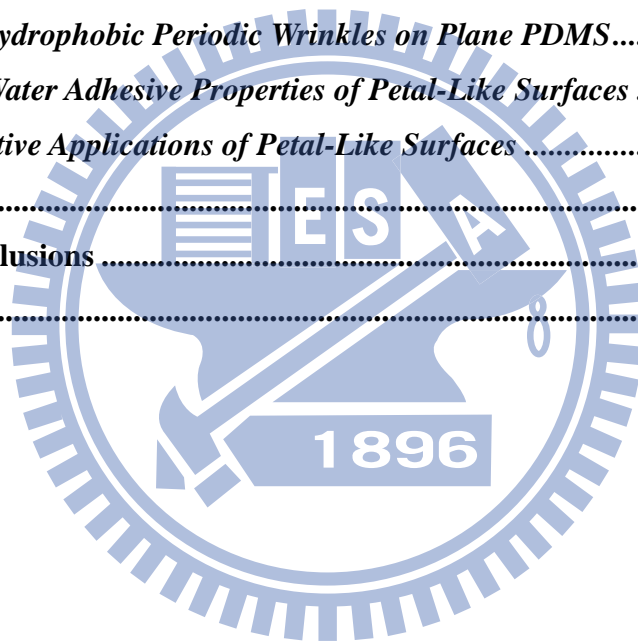
PDMS exhibited the high water adhesion up to 35.8 N/m^2 . In addition, the two superhydrophobic surfaces from the acid texture technique allowed us to fabricate a modern nonresidual stamp. The superhydrophobic and water adhesive area is applicable to transport the dye from the stamp to a paper. The superhydrophobic and self-cleaning region avoids the adhesion of dye.



Contents

Acknowledgment.....	i
Abstract (Chinese)	ii
Abstract (English)	iv
Contents	vii
List of Tables.....	ix
List of Figures.....	x
List of Abbreviations.....	xx
Chapter 1: Overview.....	1
1.1 Nanotechnology	1
1.2 Biomimetic Nanomaterials	2
1.3 Thesis Organization	3
Chapter 2: Design of Hollow-to-Solid Moth-Eye Structures Using Anodic Nanocones for High-Performance Optics and Improved Photovoltaic Cells.....	7
2.1 Introduction	7
2.1.1 Nanostructures under Porous Anodic Alumina	7
2.1.2 Subwavelength Moth-Eye Structure for Antireflection	8
2.1.3 Nanomaterials for Improved Dye-Sensitized Solar Cells	10
2.2 Materials and Methods	13
2.3 Results and Discussions	19
2.3.1 Self-Organized NDAs onto a Substrate.....	19
2.3.2 Antireflection Properties of NCAs on Si	22
2.3.3 Design of Artificial Hollow NCA for High-Performance Optics	25
2.3.4 TiO ₂ NTs and Hollow NCAs for the Improved Efficiency of DSSCs	32
2.4 Summary	40
Chapter 3: An Anisotropic, Highly Stable and Water-Cleanable Gecko Adhesion via Innovative Design of Taper Nanohairs.....	73
3.1 Introduction	73
3.1.1 Gecko-Inspired Artificial Structure for Adhesion	75
3.1.2 Geometry-Controllable Templates from PAA	85
3.2 Materials and Methods	89
3.3 Results and Discussions	91

3.3.1 <i>Fabrication of Desirable Taper PAA Templates</i>	91
3.3.2 <i>Design of Ideal Nanohairs for Gecko Adhesion</i>	93
3.3.3 <i>Adhesive Properties for Taper Nanohairs</i>	97
3.4 Summary	101
Chapter 4: Kiss from a Rose: Bioinspired Superhydrophobic and High-Water Adhesive Surfaces for Innovative Imprint Technique	124
4.1 Introduction	124
4.1.1 <i>Lotus Effect: A Superhydrophobic and Self-Cleaning Surface</i>	124
4.1.2 <i>Rose-Petal Effect: A Superhydrophobic and High Adhesive Surface</i>	126
4.2 Materials and Methods	129
4.3 Results and Discussions	131
4.3.1 <i>Superhydrophobic Periodic Wrinkles on Plane PDMS</i>	131
4.3.2 <i>High-Water Adhesive Properties of Petal-Like Surfaces</i>	135
4.3.3 <i>Innovative Applications of Petal-Like Surfaces</i>	138
4.4 Summary	139
Chapter 5: Conclusions	167
Reference	170



List of Tables

Table 2.1	71
DSSC performance metrics.	
Table 3.1	103
MA versus HA in 2.5% H ₃ PO ₄ .	
Table 3.2	103
The comparison between different types of polymer-based gecko adhesives (N/A represents “no information”).	
Table 3.3	105
Measurement of contact angle for various cases with a dry adhesive pad.	
Table 4.1	141
The treatment conditions were listed above, in which, S/N presented the volume ratio of sulfuric acid over nitric acid.	
Table 4.2	142
Expected absorption band in FT-IR spectra of PDMS and common functional groups.	
Table 4.3	143
The wetting properties of different structure levels.	

List of Figures

Figure 2.1.	43
The illustrated geometry of the RCWA configuration	
Figure 2.2.	44
Top-view SEM image of PAA film anodizing in 0.3 M oxalic acid at 40 V after a pore-widening treatment	
Figure 2.3.	45
A typically chronoamperical curve was recorded during the anodization.	
Figure 2.4.	46
Top-view SEM images of the specimens terminated at point (a) A, (b) B, (c) C and (d) D in Figure 2.3. The scale bar is 200 nm.	
Figure 2.5	47
(a) Cross-sectional SEM image of the nanodots embedded in porous alumina film. (b) Slide-view SEM image of nanodot arrays after removing alumina film. The scale bars are 100 nm.	
Figure 2.6.	48
Schematic diagrams showing the principal steps of modification of the underlying metal/alumina interface.	
Figure 2.7	49
XPS depth-profile analysis of Ta 4f spectrum for tantalum oxide nanodots on Si substrates at normal incidence. The bombardment of Ar ⁺ sputtering was used to examine the inner composition; each sputter cycle lasted 5 min.	
Figure 2.8	50
(a) Slide-view SEM image of tantalum oxide NCA in unfinished anodization. (b) Slide-view SEM image of tantalum oxide NCA in complete anodization. (c) Top-view SEM image of tantalum oxide NCA. (d) TEM image of the NCA under the porous alumina film.	
Figure 2.9	51
A schematic diagram to describe the formation mechanism of the tantalum oxide NCA	

at the Ta/Al interface.

Figure 2.1052

XPS depth-profile analysis of Ta 4f spectrum for tantalum oxide NCA on Si substrates at normal incidence. The Ar⁺ sputtering of 5 and 30 min was used to examine the inner composition.

Figure 2.1153

The spectroscopic measurements of broadband reflectance for the blank silicon wafer, the anodic tantalum oxide film and tantalum oxide NCA, respectively.

Figure 2.1254

Experimental reflectivities of NCAs on AlN substrates, formed from Ta films having dimensions ranging from 7 to 30 nm.

Figure 2.1355

A typically chronoamperical curve was recorded during the anodization of Al on glass substrates with $t_{\text{Ta}} = 0$ (general PAA), 10 (hollow NCA), and 30 nm (solid NCA).

Figure 2.1456

SEM and TEM images of cone-like nanostructure arrays. (a) Side-view SEM image (scale bar: 500 nm) of hollow NCA after alumina had been removed selectively. Inset: Magnified image. (b) Top-view SEM image (scale bar: 1 μm) of hollow NCA that had been ground using a diamond emery paper. TEM images of hollow (c), (d) and solid (e) nanostructures under porous alumina (scale bar: 100 nm). Inset (e): SAED pattern revealing the amorphous composition. (f) Schematic representation of a close-packed hexagonal NPC for theoretical calculation: period, 200 nm; base diameter, 200 nm; height, 200 nm.

Figure 2.1557

Schematic representation of the mechanism of the formation of the hollow nanocones. (a) Tantalum oxide nucleus formed as the anodization approached the Ta–Al interface. (b) Tantalum oxide hillocks grew, leaving voids caused by O₂ pressure. (c) Cone-like hollow nanostructures formed with pore-wall obstructing.

Figure 2.1658

XPS depth-profile analysis of tantalum oxide NCAs on glass substrates at normal incidence. (a) Ta 4f spectrum of solid NCA ($t_{\text{Ta}} = 30$ nm); (b) Ta 4f spectrum of

hollow NCA ($t_{Ta} = 10$ nm).

Figure 2.1759

Refractive index profiles—for samples of various t_{Ta} —through air, the nanostructure and the substrate (wavelength: 488 nm). The x-axis represents the distance from the interface of the nanostructure and the substrate.

Figure 2.1860

Schematic diagrams for effective refractive-index calculation.

Figure 2.1961

RCWA simulation of transmittance for single-sided coated Pyrex glass with various porosity and sizes NCAs. The nanocone structures was assumed to be a hexagonal close-packed period of (a) 100 nm, (b) 200 nm and (c) 300 nm with a height of (a)100 nm, (b) 200 nm and (c) 300 nm. A NCA owning a period and height of 200 nm and a porosity of 65% obtains the best transmittance.

Figure 2.2062

The optical performance of antireflective properties for NCA-coating glasses. (a) Measured transmissions of bare glass (green line) and NCA-coated (single side) glass substrates of initial Ta thicknesses of 10 nm (red line), 20 nm (blue line), 30 nm (black line) and 10 nm for double sides (orange line). Inset: Photographs of the structured (right) and unstructured (left) glass samples (30 mm × 30 mm) demonstrate the antireflective effect at a large tilted angle. (b) Measured wavelength and angle resolved absolute reflectance. The glass substrates were coated without (upper curve) and with double-sided NCA coating (lower curve).

Figure 2.2163

The improvement of reflectivity before and after the treatment for NCA coated on (a) sapphire and (b) AlN substrates. Experimental (solid) and RCWA-simulated (dotted) specular reflectivities at normal incidence were compared for a blank substrate (red lines), NCA coating (blue line) and NCA coating with treatment (green line).

Figure 2.2264

Schematic representation of our assembled DSSC featuring TiO₂ NTs and nanocones within PAA.

Figure 2.2365

Typical anodization results of Al/FTO and Al/Ti/FTO samples. (a) Chronoamperical curve recorded during the anodization process. (b, c) Photographs of systems prepared in the (b) absence and (c) presence of Ti as the adhesion layer between the Al layer and the FTO substrate.

Figure 2.2466

(a) Top-view SEM image (scale bar: 500 nm) of hollow TiO₂ nanocone arrays after alumina had been removed selectively. In the left part of the image, focused ion beam (FIB) milling had been used to reveal the hollow inner sections of the nanocones. (b) Cross-sectional TEM image of hollow TiO₂ nanocones (scale bar: 100 nm). (c–e) Schematic representation of the mechanism of formation of the hollow nanocones. (c) TiO₂ nucleus formed as the anodization approached the Ti–Al interface. (d) TiO₂ hillocks grew, leaving voids caused by O₂ pressure. (e) Cone-like hollow nanostructures formed with obstructing pore-walls

Figure 2.2567

Grazing incident X-ray diffraction (GIXRD) analysis for TiO₂ nanocones on FTO.

Figure 2.2668

(a–c) Morphology of the TiO₂ NTs grown onto the pore walls of PAA. (a, b) Top-view SEM images (scale bar: 500 nm) of PAA (a) before and (b) after deposition of the TiO₂ NTs. (c) Cross-sectional SEM image (scale bar: 200 nm) of the sample in (b). (d) GIXRD analysis of a TiO₂ NT, revealing the desirable crystalline anatase phase.

Figure 2.2769

Schematic and microscopic images of samples NT–A–NC and NT–A. (a) Schematic representation of sample NT–A. (b) The AFM image of TiO₂ film onto FTO substrate. The arithmetic average roughness (Ra) and root mean square roughness (RRMS) were 2.45 and 5.13 nm, respectively. The thickness of TiO₂ film is 100 nm from cross-sectional SEM observation. (c) Schematic representation of sample NT. (d) Top-view SEM image (scale bar: 500 nm) of anodic TiO₂ NTs of sample NT. The average inner diameter of the nanotube was 110 nm and outer diameter 160 nm. The depth of anodic TiO₂ NTs was estimated at about 700 nm from cross-sectional SEM observation. As we can see, cracks and interconnections appear in TiO₂ NTs.

Figure 2.2870

Photovoltage performances of cells constructed with various TiO₂ morphologies as electrodes: hollow TiO₂ nanocones under porous alumina and TiO₂ NTs (NT-A-NC); a

TiO₂ film under porous alumina and TiO₂ NTs (NT-A); and anodic TiO₂ NTs without alumina (NT). (a) Current–voltage characteristics of the three DSSC devices. (b) The incident photon–to–current conversion efficiency (IPCE) spectra of the three DSSC devices.

Figure 2.2972

Absorption spectra of N719 sensitizer in absolute ethanol solution. The molar extinction coefficients of MLCT absorption band for N719 dye is $1.36 \times 10^4 \text{ M}^{-1} \text{ cm}^{-1}$, which is as well as that of ILCT absorption band ($1.36 \times 10^4 \text{ M}^{-1} \text{ cm}^{-1}$).

Figure 3.1106

SEM image of our taper shape PAA. (a) The cross-sectional image showed a length of 1.4 μm . (b) The magnified image of channel tips. Top-view images of the pore-widening time in (c) 3 min and (d) 15 min.

Figure 3.2107

Chronoamperical curves during HA in 0.25 M H₃PO₄. A conventional MA (0.25 M H₃PO₄, 160 V) is also plotted (blue line) for comparison.

Figure 3.3108

SEM images of taper PAA with different lengths: (a) 600 nm, (b) 1.1 μm , (c) 1.8 μm , and (d) 2.3 μm .

Figure 3.4109

Processing anodization in H₃PO₄ with different concentration. (a) 1% which cannot offer enough ionic species. (b) 5% and (c) 10% with excess jeoul heat from current densities.

Figure 3.5 110

(a)-(d) Demonstrated that the ordered condition increased as voltage parameter increased. (e) The relationship between interpore distances, current densities and voltage.

Figure 3.6 111

SEM images of decoupling system. (a)-(b) Optimal processing widows in both first and second step. Unmatched voltage cause a bad result because the applied voltage at second step is (c) insufficient and (d) excess to fit the optimal condition.

Figure 3.7	112
(a) Taper shaped pillars profile sketch map. (b) Pillar shape profile sketch map. (c) SEM image of taper shaped pillars and (d) Illustration of taper's advantage.	
Figure 3.8	113
Force measurements versus cycles of attachment and detachment, and the force remained the same for over hundreds of time.	
Figure 3.9	114
Taper pillars with different lengths. (a) 600 nm from tilted SEM image (b) 600 nm from cross SEM image. (c) 1.4 μm from cross SEM image. (d) 1.4 μm from cross SEM image. The insets showed the molds of replicating or SEM images of high magnification, respectively.	
Figure 3.10	115
SEM images of taper and pillar nanohairs. (a) Low magnification of our structure and the inset is the top view image that displays the taper edge and hexagonal arrays. (b) Tilted SEM image of the pillar shape showing this type cannot support the same height as the taper shape and (c) SEM image from cross-section. (d) Stable pillar with decreasing the length.	
Figure 3.11	116
Illustrated hierarchy (a) of gecko and (b) of taper shape as a hierarchy-like by "cake" model. (c) Illustration of Eq. 8.	
Figure 3.12	117
Displays the simulation of E_{eff} versus slanted angle. Clearly, the E_{eff} drops below 100 kPa, which fits the Dahlquist criterion, with decreasing slanted angle after 73° .	
Figure 3.13	118
Theoretical analysis of directional adhesion mechanism of the slanted taper shaped pillars. An illustration showed the change of leaning angle of the slanted taper nanohairs when the adhesive is pulled in (a) the gripping, (b) initial state and (c) releasing direction.	
Figure 3.14	119
Taper shaped pillars with slanted angle we fabricated by pressure technique. (a) Low magnification. (b) High magnification of tilted SEM image of the structure. (c) Low	

magnification and (d) high magnification from cross-sectional view.

Figure 3.15120

Simulation of critical peeling-off forces as a function of peeling angle.

Figure 3.16121

Measurement of shear force for various cases with an adhesive patch of 1.0 cm^2 . The taper nanohairs were composed of soft PUA.

Figure 3.17122

Giving a comparison between taper shape and pillar shape, we can find out the higher adhesion of taper shape than pillars' can account for the higher density, longer length or adhere efficiently we have discussed previously.

Figure 3.18122

Photographs of (a) tape of PUA after replicating and the mold. (b) Counter weight measured system. (c) The high CA of tape after detaching from the glass.

Figure 4.1144

A liquid droplet in contact with (a) a smooth solid surface (b), (c) a rough solid surface. (b) Illustrate Wenzel's wetting state. (c) Illustrate Cassie's wetting state.

Figure 4.2145

The scheme showed the protocol of manufacturing a petal-like PDMS.

Figure 4.3146

Optical microscopy images of PDMS through acid treatment. The acid solution was a mixture of sulfuric acid and nitric acid in the volume ratio of 1/1, etching with different treatment times of (a) 5 s, (b) 15 s, (c) 30 s, and (d) 60 s.

Figure 4.4147

Optical microscopy images of PDMS through acid treatment. The acid solution was a mixture of sulfuric acid and nitric acid in the volume ratio of 2/1, etching with different treatment times of (a) 5 s, (b) 15 s, (c) 30 s, and (d) 60 s.

Figure 4.5148

The diagram showed the periodic wrinkles resulted from the increasing immersion time at different acid composition of sulfuric acid/nitric acid = 1/1 and 2/1 in volume

ratio.

Figure 4.6149

The diagram indicated that width of the periodic wrinkles at the same etching time was proportional to the reaction temperature. The acid was composed of sulfuric acid and nitric acid in a volume ratio of 1/1.

Figure 4.7150

Plane PDMS treated with acid producing a superhydrophobic surface. (a) Optical microscope image of periodic wrinkles PDMS caused by acid corrosion. (b), (c) SEM images showing micro- and nano-structures on the sample respectively. (d) A 5 mg water droplet located on the superhydrophobic PDMS surface, showing a contact angle of 151.5°.

Figure 4.8151

The formation mechanism of periodic wrinkles under plane PDMS. PDMS was fixed onto a clean wafer then underwent an acid corrosion. Outer layer of PDMS was reacted by acid which caused a different thermal expansion coefficient between inner layer (bulk PDMS) and outer layer (reaction region). During cooling process, it formed periodic wrinkles.

Figure 4.9152

The chemical structure of PDMS and its intergradients.

Figure 4.10153

(a) The FTIR spectra of PDMS for different treatments. (b) No treatment. (c) Treated by pure sulfuric acid. (d) Treated by mixture acid, sulfuric acid/nitric acid = 1/1 in volume ratio.

Figure 4.11154

(a)-(n) Images showed the contact angle changed from different condition solution, pH values changed from 1-14. The superhydrophobic property of the treated PDMS surface maintained as similar as the pure water. A high contact angle around 150° was revealed during the wide range of pH values.

Figure 4.12155

Wetting phenomena of different [H⁺] solutions on acid-treated PDMS.

Figure 4.13	156
Graph showing the relationship between time and contact angle on the treated PDMS.	
Figure 4.14	157
The SEM images of dehydrated rose petals. (a) The surface showed the large-scaled convex about 30 μm in width (b) The surface showed the sub-fold of approximately 800 nm in width.	
Figure 4.15	158
Scheme showed the formation of PS spheres assembled on a silicon wafer caused by the water flow.	
Figure 4.16.	159
(a) The SEM image show the close-packed convex. (b), (c) Showing SEM images for the manufactured surface with the topography which was similar to the rose-petal (d) SEM image indicated the nanostructure of the surface.	
Figure 4.17	160
Scheme of the three level structures on PDMS.	
Figure 4.18	161
A 5 mg water droplet pinned on (a) a flat PDMS surface, (b) a PDMS with micro-scaled convex, and (c), (d) a PDMS surface with petal-like morphology when turning the surface vertically (90°) and upside (180°) respectively.	
Figure 4.19	162
Water penetrate the microscale convex and partial wetting the upper part of nanoscale wrinkles.	
Figure 4.20	163
The graph of water contact angles and adhesive force between different morphology, flat, micro-scaled convex and petal-like topography.	
Figure 4.21	164
The histogram of water contact angles and adhesive forces on the petal-like surface changed with decanting times. Blue rectangles indicated that adhesive force increased from 28.9 N/m^2 to 35.8 N/m^2 . Orange rectangles showed the contact angle changed from 137.9° to 150.1° .	

Figure 4.22165

A 5 mg water droplet transported from a hydrophobic and non-sticky surface to a hydrophilic surface by the petal-like surface PDMS.

Figure 4.23166

(a) Scheme indicated the two different superhydrophobic surfaces on the PDMS. (b) Several hundreds of patterns on the paper by using the fabricated PDMS stamp continuously. (c) The image showed the PDMS stamp remained cleaning after imprinting upon a paper with the stamp for several hundred times.



List of Abbreviations

AFM	atomic force microscopy
AR	antireflection
ARS	antireflection structure
ASTM	American society for testing and materials
CA	contact angle
CNT	carbon nanotube
DSSC	dye-sensitized solar cell
ESCA	electron spectroscopy for chemical analysis
FTIR	Fourier transform infrared spectroscopy
FTO	fluorine-doped tin oxide
GIXRD	grazing incident X-ray diffraction
HA	hard anodization
IPCE	incident-photon-to-electron conversion efficiency
LED	light-emitting diode
MA	mild anodization
NC	nanocone
NCA	nanocone array
ND	nanodot
NDA	nanodot array
NT	nanotube
NP	nanoparticle
PAA	porous anodic alumina
PDMS	polydimethylsiloxane
RCWA	rigorous coupled wave analysis
SEM	scanning electron microscopy
TEM	transmission electron microscopy
TCO	transparent conductive oxide
VLS	vapor-liquid-solid
XPS	X-ray photoelectron spectroscopy

Chapter 1: Overview

1.1 Nanotechnology

“There’s plenty of room at the bottom” is the title of a classic talk given on December 29, 1959, in which the great physicist Richard Feynman introduced a new field of physics to the annual meeting of the American Physical Society at the California Institute of Technology. Over 40 years ago, Feynman imagined a new physical world of ultra-small volumes and highlighted some difficulties that researchers might encounter when visiting it. His talk provided a vision for engineers and scientists to establish a new field, which—with subsequent developments in novel equipment and manufacturing skills—is now known as “nanotechnology.”

In recent years nanotechnology has become one of the most important and exciting forefront field in physics, chemistry, engineering and biology which the characteristic dimensions are below ca. 1000 nm. It shows great promise for providing us in the near future with many breakthroughs that will change the direction of technological advances in a wide range of applications. This kind of work is often called nanotechnology. Sub-micron lithography is clearly very profitable—ask anyone who uses a computer—but it is equally clear that conventional lithographic techniques will not let us prepare semiconductor devices in which individual dopant atoms are located at specific lattice sites. Although computer hardware capability has exhibited steady exponential growth for the last 50 years—and there is a fairly widespread belief that these trends are likely to continue for at least several more years—conventional lithographic techniques are beginning to reach their limits.

As semiconductor devices become scaled down to ever-smaller sizes within the nano-regime, a variety of technological and economic problems arise, the rules of

classical physics give way to quantum mechanics, and the term “molecular-scale” becomes more accurate than “nanoscale.” At this point, the scaling of sizes that has successfully reduced device features from the microscale to the nanoscale reaches its limits, and, therefore, alternative manufacturing methods, materials, device structures, and architectures are required.

1.2 Biomimetic Nanomaterials

Nature has gone through evolution over the 3.8 G year since life is estimated to have appeared on the Earth. Nature has evolved objects with high performance using commonly found materials. These function on the macroscale to the nanoscale. The understanding of the functions provided by objects and processes found in nature can guide us to imitate and produce nanomaterials, nanodevices and processes. On nanoscale, many of the atoms are still located on the surface, or one layer removed from the surface, as opposed to the interior. Thus, different properties are observed on this scale due to the interface that is not observed in the bulk or individual atoms. Since the properties depend on the size of the structure, instead of the nature of the material, reliable and continual change can be achieved using a single material. As to nanoscale structure, nature is the best teacher giving from God. Biologically inspired design or adaptation or derivation from nature is referred to as ‘biomimetics’. It means mimicking biology or nature and is defined as ‘the study of the formation, structure or function of biologically produced substances and materials and biological mechanisms and processes especially for the purpose of synthesizing similar products by artificial mechanisms which mimic natural ones’. Nature uses commonly found materials, and properties of the materials and surfaces result from a complex interplay between the surface structure and the morphology and physical and chemical properties. Many materials, surfaces and devices provide multifunctionality.

Molecular-scale devices, superhydrophobicity, self-cleaning, drag reduction in fluid flow, energy conversion and conservation, high adhesion, reversible adhesion, aerodynamic lift, materials and fibers with high mechanical strength, biological self-assembly, antireflection, structural coloration, thermal insulation, self-healing and sensoryaid mechanisms are some of the examples found in nature that are of commercial interest. The emerging field of biomimetics is already gaining a foothold in the scientific and technical arena. It is clear that nature has evolved and optimized a large number of materials and structured surfaces with rather unique characteristics. As we understand the underlying mechanisms, we can begin to exploit them for commercial applications.

1.3 Thesis Organization

In Chapter 2, we demonstrate an innovative approach for the fabrication of self-organized, hollow-to-solid nanocone arrays, using an anodization of Al/Ta interlayer on a substrate. The porosity of the hollow nanostructures is calculatedly controlled by the deposited thickness of Ta film. We also employ subwavelength nanocone arrays as Moth-eyes structures for high-performance antireflection coatings. These oxide nanostructures greatly suppress reflectance over a large range of wavelengths and angles of incidence and display a good mechanical stability. By designing a corresponding porosity, these nanostructures can be applied to various substrates for an effective antireflection coating. Also, we introduce a new photoelectrode architecture inspired by Moth-eyes structure, fabricated through facile synthesis of self-organized hollow TiO_2 nanocones under porous anodic alumina (PAA) featuring TiO_2 nanotubes (NTs) within. PAA was grown directly on a fluorine-doped tin oxide (FTO) substrate, which provided good contact for PAA-based dye-sensitized solar cells (DSSCs). The TiO_2 nanocones grew as

anodization proceeded for the growth of the PAA and the underlying Ti, preventing the delamination of PAA from the substrate and the formation of an undesirable barrier layer. Ordered TiO₂ NT arrays having (inner diameter: 120 nm; length: 800 nm) were grown along the pore walls of the PAA by infiltrating with Ti(OiPr)₄. The hybrid structure was integrated into a DSSC device using a commercially available ruthenium-based N719 dye. The cell incorporating hollow TiO₂ nanocones under PAA and TiO₂ NTs as the working electrode generated a photocurrent of 5.15 mA/cm², an open-circuit voltage of 0.64 V, and a power conversion efficiency of 1.71%—superior performance relative to those of corresponding TiO₂ NT/PAA and TiO₂ NT-alone devices.

In Chapter 3, we explored another biomimetic material: dry adhesion inspired by gecko's feet. It has attracted much attention because it provides strong, yet reversible attachment against surfaces of varying roughness and orientation. Recently, theoretical and experimental investigations into the field of mimicking gecko adhesives have reported; however, they suffered from some disadvantages due to materials' limitation compared with nature material from gecko. In this study, we designed the efficient method of an innovate structure for ideal dry adhesives. A taper anodic alumina oxide mold with a length of 1.3 μm and a diameter of 380 nm was fabricated using decoupling two-step hard-anodization process which was firstly reported by us. After molding, taper-shaped nanohair array with slanted angle was presented. The approach to fabricate angled taper nanohair arrays obtained an excellent directional, reusable, and water cleanable use in large area. The angled taper nanohair facilitated the stability and self-cleaning properties compared with pillar nanohairs. A remarkably directional force exhibited by angled taper nanohair arrays was showing here with strong shear attachment (~8 N/cm²) in the gripping direction and easy releasing(~1.4 N/cm²) in the reverse direction (pulled against the angled

direction of hairs). The smart adhesive presented here would enable the climbing robots, cleaning transport system such as LCD factory and non-residue sticker for future generation. We believe such a novel structure which is a low-cost, brilliant adhesion; highly stable and even self-cleaning is integral and promising for the future using.

In Chapter 4, we explored final biomimetic material: a rose petal. Many bio-inspired superhydrophobic surfaces with self-cleaning property have been fabricated since “Lotus effect” was discovered. However, scientists were fascinated by the petal’s surface which has superhydrophobicity and high water adhesion in recent years. The phenomenon is induced by the microscale convex and nanostructures upon the petal. So far, researchers have perplexed how to manufacture the complicated topography and applied it to reality. To mimic the petal’s surface, we developed a bottom-up method by the simple acid texture technique to fabricate the superhydrophobic PDMS surface with high water adhesion and self-cleaning ability. The resulting petal-like PDMS had convexes about 35 μm in diameter, nanowrinkles around 500 nm in width and nanostructures less than 100 nm. A high water contact angle larger than 150° was displayed, even after a long-time duration test. These results caused only by morphology changing instead of chemical modification. The superhydrophobicity could maintain at least a month. Besides, the corrosive solutions range from pH value 1 to 14 also displayed high contact angles on the PDMS surface. Moreover, the petal-like PDMS exhibited the high water adhesion up to 35.8 N/m^2 . We used the petal-like PDMS surface as a sticky palm to transport a 5 mg water droplet from the superhydrophobic and self-cleaning PDMS to the hydrophilic silicon wafer. In addition, the two superhydrophobic surfaces from the acid texture technique allowed us to fabricate a modern nonresidual stamp. The superhydrophobic and water adhesive area is applicable to transport the dye from the stamp to a paper. The

superhydrophobic and self-cleaning region avoids the adhesion of dye. Thus, the new-generation superhydrophobic surface can be widely applied to biotechnology, MEMS and industry.

Finally, we concluded the experimental results and discussion; plus, some future works are also involved in Chapter 5.



Chapter 2: Design of Hollow-to-Solid Moth-Eye Structures Using Anodic Nanocones for High-Performance Optics and Improved Photovoltaic Cells

2.1 Introduction

2.1.1 Nanostructures under Porous Anodic Alumina

Porous anodic alumina (PAA) formed by anodization has been widely studied during the last few decades.¹ Because of their relatively regular structure with narrow size distributions of pore diameters and interpore spacings, porous alumina membranes are used for the fabrication of nanometer scale composites. The pore structure is a self-ordered hexagonal array of cells with cylindrical pores of variable sizes with diameters of 25 nm to 500 nm with depths exceeding 100 nm depending on the anodizing conditions used. The geometry of anodic porous alumina may be schematically represented as a honeycomb structure which is characterized by a close-packed array of columnar hexagonal cells,² each containing a central pore normal to the substrate.³ These properties make anodized aluminum a desirable material for many microfabricated fluidic devices, quantum-dot arrays, polarizers, magnetic memory arrays, high-aspect-ratio microelectromechanical systems, and photonic crystals.

The majority of previous studies used Al foils to prepare PAA films, which must eventually be separated from the Al foil for later applications. This is apparently not suitable for most integrated device applications. Recently, nanoporous PAA has been prepared directly on Al films coated on silicon wafers for integrated microelectronic

applications.⁴⁻⁸ Researches has shown that the microstructure of PAA prepared from Al films on semiconductor⁴ or glass⁹ substrates are very different from that of PAA obtained directly from Al foils. Beneath each pore bottom, a semispherical nanovoid is formed at the alumina barrier layer/substrate interface. If anodization of Al films is formed at the alumina barrier layer/substrate interface. If anodization of Al films deposited on a different metal film,¹⁰⁻¹¹ the anodization process is reported to include two oxidation stages, i.e., anodic oxidations of the Al layer and the underlying metal layer. In these cases, a metal whose oxide form has a higher ionic conductivity than alumina was used as an underlayer preceding an Al anodization process, the underlying metal would be also oxidized and thereby form metal–oxide nanostructures with a similar pattern as the upper PAA.¹²⁻¹⁵ The oxides of Ti, Ta, Nb and W are known to penetrate the barrier layer of PAA and grow into nanodot or nanorod arrays. The nanoporous array is formed, which can then be used as a mask for local anodization of the underlying metal layer, thereby forming a metal–oxide nanostructured array with a similar pattern as the upper PAA nanoporous array.

2.1.2 Subwavelength Moth–Eye Structure for Antireflection

Antireflection (AR) coating is one of the most important optical designs and it makes up more than 50% of the total optical thin-film market.¹⁶ It is used to suppress surface reflection and to increase transmission of light for optical applications, such as flat panel displays, lasers, photovoltaic devices, and all kinds of lenses. Rayleigh firstly observed a thin film whose refractive index (n) is the geometric mean of the air and then substrate's indices reduced the reflection on the surface of the substrate optimally. In early 19th century, interference AR (antireflection) coating was discovered using one quarter of the light's wavelength in thickness. Thus a single layer structure was applied in general AR coatings by following the aforementioned two conditions, but it only works at a specific wavelength and a normally incident light source. Over the past few decades, the AR coatings primarily consisted of

multi-layer coatings comprising layers of high- and low- n . Through the algorithm design, multi-layer coatings were applied to achieve a wider broadband AR across a visible region for incident angles ranging from 0 to 50.¹⁷ However, complicated stacking processes and unsatisfied angle-independence ability on multi-layer AR coatings forced scientists to develop next-generation AR structures for future optical devices.

According to optical theory, the refractive index of the AR layer should gradually decrease from air to the substrate.¹⁸ Apparently, the refractive index of any dense material is not small enough, but Nature provides a solution for such antireflective structure (ARS). The moth eye consists of quasi-close-packed nipples having heights and spacings typically of less than 300 nm, which reduces reflection from their compound eyes.¹⁹ The ARS on the corneas of these insects gradually match the optical impedance of one medium with its neighbour across the interface.²⁰ This concept has been applied to realize a variety of photonic systems, particularly semiconductor photovoltaic devices. Many techniques on the basis of top-down etching like lithography,²¹ self-organized templates,²²⁻²⁴ and mask-less etching²⁵⁻²⁶ have been used to fabricate tip-like nanostructure for ARS surfaces. Other ARS surfaces based on bottom-up growth like conical nanorods fabricated by the vapor-liquid-solid (VLS) method^{10,27} and oblique-angle deposition^{11,28} also succeed in enhancing light coupling in solar cells or more efficient light extraction from LEDs.

For optical transparencies with low- n (e.g., glass, quartz), it remains a challenge to improve the transmission over a broad wavelength and incidence by using ARS. Unlike Si and other semiconductor materials, these transparent substrates are arduous to etch anisotropically and selectively. Few ARS surfaces on fused silica or glass have been reported recently.²⁹⁻³⁰ For the low-cost and large-scale fabrication, hence porous polymer films have been developed to achieve ideal AR efficiency. Walheim et

al. and Ibn-Elhaj et al. pioneered in nano-corrugated surfaces by removing one component of phase-separated polymer films and showed improved transmittance as high as 99%.³¹⁻³² A further nanoporous multilayer film with a gradual porosity ratio for each layer demonstrated an advantage in omnidirectional reflection of incident light.³³⁻³⁴ Other hybrid porous films composed of nanoparticles and polymer matrix were assembled by a layer-by-layer (LBL) technique and also resulted in an increase of light transmission.³⁵⁻³⁶ Nevertheless, polymer-based ARSs continue to exhibit several fundamental problems, such as layer ablation and surface abrasion. In addition, polymer-based materials suffer from thermal decomposition at a high temperature and/or radiation damage when subjected to ultraviolet light.

2.1.3 Nanomaterials for Improved Dye-Sensitized Solar Cells

With the growing interest in green energy, solar cells have become a potential solution to mitigate the problems of global warming. Scientists and engineers are seeking next-generation photovoltaic systems exhibiting high efficiencies, low costs, and the possibility of high-throughput manufacture. Since the pioneering studies of Grätzel et al., dye-sensitized solar cells (DSSCs) have blossomed to have great potential for commercialization.³⁷ DSSCs provide some advantages over conventional solid state solar cells: insensitivity to oblique light incidence and temperature effects; very-low-cost, simple fabrication; transparency; and flexibility. DSSCs comprise four main building blocks: a photoanode of TiO₂ nanoparticles (NPs), a light-absorbing dye, an iodide electrolyte, and a Pt counter-electrode.³⁸ Photo-excitation of the dye results in injection of electrons into the TiO₂ NPs, while holes are released to the iodide/triiodide couples in the electrolyte. Carriers are transported in the conduction band of TiO₂ and diffuse to the charge collector of the transparent conductive oxide (TCO). The iodide is reduced to triiodide at the counter-electrode. The circuit is completed through electron migration through the external load.³⁹

In the past few years, increases in DSSC efficiencies have been attributed to improvements in the syntheses of ruthenium complex dyes and in the nanoscale architectures of the TiO₂ networks.⁴⁰⁻⁴¹ Several ruthenium dyes have been synthesized that provide excellent IPCEs, some reaching greater than 11%.⁴²⁻⁴³ Although the development of photoanodes has been relatively lagging, it remains one of the most promising avenues toward enhancing device performance. The ability to fabricate modern TiO₂ networks is expected to have a positive impact on solar cell performance by providing more-direct migration pathways with improved charge transport efficiencies.⁴⁴ Porous networks of TiO₂ NPs typically serve as the photoanode of DSSCs on the surface of transparent conducting glass. Unfortunately, the broad distribution of interconnections resulting from a randomly packed NP network significantly retards the transport dynamics.⁴⁵ The structured disorder associated with the contacts between the TiO₂ NPs enhances the scattering of free electrons, thereby reducing electron mobility.⁴⁶

Recently, TiO₂ nanotube (NT) arrays have been considered as alternative modern electrodes, replacing TiO₂ NPs, for highly efficient DSSCs.⁴⁷⁻⁵⁰ TiO₂ NT arrays, which possess an ordered and strongly interconnected nanoscale photoanode architecture, provide superior electron lifetimes and more-direct migration pathways for electron percolation; they also result in markedly higher charge-collection efficiencies and light-harvesting efficiencies relative to those of traditional NP films. TiO₂ NT arrays are prepared through anodization of thick-film Ti foils or Ti films on transparent conducting glasses. Intuitively, NT-based DSSCs should have higher efficiencies than their NP-based counterparts; practically, however, the overall conversion efficiencies that have been reported previously are similar for both types of film structures. The results are imputed to aggregation of the NTs, arising from the capillary forces, during the fabrication process. The individual NTs are transformed

into clusters of bundled NTs during the anodization process or electrolyte injection, and may be accompanied by cracking of the film. Similar phenomena have been observed for other one-dimensional nanostructures (e.g., Si nanowires and carbon NTs).⁵¹ The bundling of NTs, much like porous NP films, produces many unnecessary interconnections. These contacts substantially retard electron transport and the dye-loading capacity, thereby leading to poor efficiency.⁵²

Hupp and co-workers have developed one solution to this problem by separating the TiO₂ NTs using commercial porous anodic alumina (PAA) membranes.⁵³⁻⁵⁴ The reactive gas precursor was coated into PAA conformably using an atomic layer deposition (ALD) system to form TiO₂ NTs along the pore wall. Kang et al. fabricated highly ordered TiO₂ NTs using the same PAA templating method.⁵⁵ A modified sol-gel route was used to infiltrate the commercial PAA with Ti(OiPr)₄, which was subsequently converted into TiO₂ NTs. The photovoltaic performance of such TiO₂/PAA cells was, however, barely acceptable. Theoretically, the separating of NTs, without interconnection, should improve electron transport, leading to higher photoefficiencies; in addition, the alumina layer should slow the recombination of photogenerated electrons on the TiO₂ conduction band and holes in the electrolyte or the oxidized dye. A problem inherent to these devices is poor contact between commercial PAA and the TCO layer, resulting in a loss of current transportation. Besides, macro/micro-crack formation during the transfer of freestanding PAA films onto TCO substrates can also have a negative effect on photovoltaic performance.

Growing PAA directly on TCO substrates might overcome the aforementioned problems. A uniform PAA, with sufficient adhesion to the TCO layer to withstand thermal and surface treatment, is imperative for DSSC fabrication.⁵⁶⁻⁵⁷ Although promising in theory, practical implementation of this approach has two major challenges. The first is poor anodization on the Al/TCO bilayer, mainly due to poor

adhesion between Al and TCO. When a noble metal or TCO serves as the underlying substrate, the evolution of gaseous O₂ produces stress that damages the PAA/TCO adhesion. As many previous reports have described, the upper PAA eventually delaminates from the underlayer, weakening the performance of the resulting cells.^{9,58} The second major challenge is forming a thick alumina barrier at the interface between the PAA and the TCO layer.⁵⁹⁻⁶⁰ The formation of PAA, either from Al foil or from Al and a substrate, accompanies a barrier layer at the bottom of the pore channels. The isolated barrier layer would prohibit the connection of the pore channels and the substrate; in the DSSC application, it would block current transport between the TiO₂ NTs and the TCO layer. In addition, because the current density is inversely proportional to the exponent of barrier thickness for a given anodization voltage,⁶¹ the high current density produced by a highly conductive TCO would result in a thick alumina barrier, which would be difficult to remove selectively using dilute phosphoric acid while also widening the pores.⁶²

2.2 Materials and Methods

Chemicals and Materials. Phosphoric acid (H₃PO₄, 86%), anhydrous ethanol (99.5%), Iodine (98%), lithium iodide (99%) and dihydrate oxalic acid (C₂H₂O₄·2H₂O, 99.8%) were purchased from J. T. Baker (Phillipsburg, NJ, USA). 4-*tert*-butylpyridine (TBP, 96%), 3-methoxypropionitrile (MPN, 99%), and Ti(O*i*Pr)₄ (97%) were purchased from Aldrich. Chromium trioxide (CrO₃, 99%) and perchloric acid (HClO₄, 70%) were purchased from Showa (Tokyo, Japan). A hot-molten film (SX-1170), FTO glass (10 Ω/sq, TCO10-10), and ruthenium 535-*bis*-TBA (N719) were purchased from Solaronix. Dihydrogen hexachloroplatinate (H₂PtCl₆) solution was purchased from Alfa Aesar. Aluminum nitride substrate (AlN, 99.95%) and Pyrex 7740 glass were purchased from Corning (Corning, NY, USA). Silicon Wafer (*p*-type) Tantalum target

(99.995%), Titanium target (99.995%) and aluminum slugs (99.995%) were purchased from Praxair (Danbury, CN, USA). Ultrapure water used in all experiments was purified with a Milli-Q apparatus (Millipore, Billerica, MA, USA) to a resistivity of 18.2 M Ω cm. All chemicals were used without further purification.

Al/Ta Bilayers Preparation. The tantalum film was deposited onto cleaned silicon wafer, borosilicate glass (Pyrex 7740), AlN and sapphire substrates by an ultrahigh vacuum DC sputtering system (ULVAC, SBH-3308). Before film deposition, the base pressure of the sputtering chamber was adjusted to approximately 5×10^{-7} Torr. Subsequently, the sample was followed by deposition of an aluminum film (5 μ m) using thermal evaporation (ULVAC EBX-6D) in a high vacuum chamber (2×10^{-6} Torr). The Al/Ta sample then was electrochemically polished in a vigorously stirred 1:4 mixture solution of HClO₄ and ethanol (1 °C) at fixed 20 V in order to reduce the surface roughness during high-field anodization.

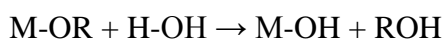
Al/Ti Bilayer Preparation. Ti (15 nm) and Al (1 μ m) films were deposited sequentially onto cleaned FTO glass using an ultrahigh vacuum DC sputtering system (ULVAC, SBH-3308). Prior to film deposition, the base pressure of the sputtering chamber was adjusted to approximately 5×10^{-7} torr. Subsequently, the sample was annealed under Ar/H₂ ambient at 400 °C for 2 h to reduce the defects and improve the adhesion. The Al/Ti/FTO sample then was polished electrochemically (20 V, 1 °C) in a vigorously stirred mixture of HClO₄ and EtOH (1:4) to reduce the surface roughness during high-field anodization.

Anodization Process. Anodization was performed in a glass beaker cooled by a powerful cooling system with vigorous magnetic stirring and maintained at the temperature of 1 °C. A DC power supply connected to a computer system was used to control the variations of potential and current during anodization. A Cu foil was used as the support for the working electrode. The substrate was positioned on top of the

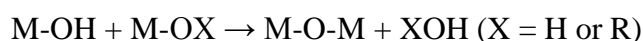
support while Cu tapes were used to connect the Cu support to the Al film upon the sample. The design advances the uniform current distribution from Cu support to underlying Al, leading to a homogeneous anodization. Two acrylic caps were used to fasten the sample and the Cu support inside within O-ring.

Synthesis of TiO₂ NTs. Titanium isopropoxide (5 mL) was added to absolute EtOH (25 mL) with vigorous magnetic stirring while maintaining the temperature at 1 °C. Separately, water (0.5 mL) and 0.1 mol/L HCl (0.5 mL) were added to EtOH (25 mL). Thereupon, the Ti(OiPr)₄/EtOH sol was slowly added to the EtOH/HCl/H₂O mixture at room temperature. After the resulting gel solution turned a milky color (60 s of homogenization), the PAA/FTO substrates (subjected to pre-treatment with EtOH) were immediately immersed into the gel solution for 1 min to form TiO₂ NTs. The residual gel solution on the back of the sample was washed away with EtOH. After drying in air at room temperature, the sample was placed in a furnace, heated at a rate of 2 °C/min up to 450 °C, and held at that temperature for 5 h to crystallize it into anatase TiO₂. There are two main steps in the mechanism of Ti(OiPr)₄ sol-gel process; the first one is hydrolysis and the other is poly-condensation. The reaction is described as below:

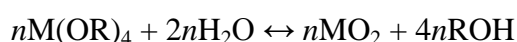
Hydrolysis reaction:



Poly-condensation reaction:



Net reaction:



,where R and M(OR)_n represent alkyl-group and titanium isopropoxide.

Cell assembly. The sample was sensitized in absolute EtOH solution containing $6.7 \times$

10^{-4} M N719 dye for 12 h. The dyed electrodes were rinsed with absolute EtOH and dried under a N_2 stream. A Pt counter electrode was prepared by spin-coating H_2PtCl_6 solution onto the FTO glass and then sintering it at 450 °C for 30 min. The dye-covered TiO_2 electrode and Pt counter electrode were assembled into a sandwich-type cell. The electrode spacing between them was sealed using a 25- μ m-thick hot-molten film as a spacer. The electrolyte (0.5 M LiI, 0.05 M I_2 , and 0.5 M TBP in MPN) was introduced into the cell through a hole (diameter: 1 mm) drilled in the counter electrode. A second spacer was sealed over the hole using a soldering iron.

Characterization. The morphology was observed by a field-emission scanning electron microscopy (JEOL, JSE-6700F) and field-emission transmission electron microscopy (JEOL, JEM-2100F). The XPS employed to analyze the chemical composition in depth profiles was performed on a Physical Electronics ESCA PHI1600 system with $Al-K\alpha$ excitation. The reflectance and transmittance were measured by variable-angle optical spectrometer (Hitachi, U-4100) with an integrating sphere. The refractive index was confirmed by a variable-angle spectroscopic ellipsometer. Grazing-incidence X-ray diffraction (GIXRD, PANalytical X'Pert Pro system) was used to examine the composition. A one-sun AM-1.5 solar simulator (Sciencetech, SF150) served as the standard light source for the photovoltaic devices. The current–voltage characteristics were examined using Keithley 2400 source-meter instruments with a probe station system. UV–Vis spectroscopy (Hitachi, U3100) was used to measure the absorption of the organic materials.

Mechanical Test. After NCAs were fabricated on AlN and sapphire substrates, a serial test including abrasion, corrosion, and temperature resistance was acquired. In the beginning, abrasion resistance was performed on a Taber 5750 abraser according

to the ASTM standard. The test involved 100 cycles of abrasion using a CS10-F resilient wheel with a 350 g load. Next, corrosion resistance was performed in 2 M H₂SO₄ solution at a temperature of 60 °C for 2 hours. Finally, a high temperature test was conducted in a furnace with a heating rate of 5 °C/min and kept at 800 °C for 2 hours.

Rigorous Coupled–Wave Analysis. The Rigorous coupled–wave analysis (RCWA) method describes the propagating fields inside the nanostructure with periodic structures by a plane wave expansion. Maxwell’s equations are then converted into a system of linear ordinary differential equations by applying spatial Fourier expansions of the field and the permittivity. The speed and accuracy of the RCWA method depend on the number of retained orders. The advantage of using the RCWA is that the reflected and transmitted fields from the nanostructure has been expressed in terms of the spatial Fourier expansion, which can be directly employed in the following aerial image analysis. Moreover, when simulating the 3D structures with symmetric crossed gratings, the computing efficiency can be much more improved by applying the symmetry properties of the grating diffraction problem.

As shown in Figure 2.1, the whole structure can be divided into three regions: the incident region (Region I), the structured region (Region II) and the exit region (Region III). The incident normalized electric field can be expressed in the form

$$\mathbf{E}_{inc} = \hat{u} \exp[-j(k_{inc,x}x + k_{inc,y}y + k_{inc,z}z)]$$

where \hat{u} is the unit polarization vector; $k_{inc,x} = k_0 n_1 \sin \theta \cos \varphi$; $k_{inc,y} = k_0 n_1 \sin \theta \sin \varphi$; $k_{inc,z} = k_0 n_1 \cos \theta$; $k_0 = 2\pi/\lambda$; and n_1 is the refractive index of the incident region.

The total electric fields in the external regions (I, III) can be expressed as

$$\mathbf{E}_I = \mathbf{E}_{inc} + \sum_{m,n} \mathbf{R}_{mn} \exp[-j(k_{xm}x + k_{yn}y - k_{lz,mm}z)]$$

$$\mathbf{E}_{III} = \sum_{m,n} \mathbf{T}_{mn} \exp\{-j[k_{xm}x + k_{yn}y + k_{IIIz,mm}(z-h)]\}$$

where \mathbf{R}_{mn} and \mathbf{T}_{mn} are the complex amplitudes of $(m,n)^{\text{th}}$ reflected and transmitted orders, respectively. The wave vector components k_{xm} and k_{yn} can be determined from the Floquet conditions and are given by

$$k_{xm} = k_{inc,x} + m\left(\frac{2\pi}{\Lambda_x}\right)$$

$$k_{yn} = k_{inc,y} + n\left(\frac{2\pi}{\Lambda_y}\right)$$

$$k_{xm}^2 + k_{yn}^2 + k_{lz,mm}^2 = (k_0 n_l)^2, \quad l = \text{I, III}$$

where Λ_x and Λ_y are the periods of the grating along the x and y directions in the substrate scale. n_I and n_{III} are the refractive indices of the incident and exit regions.

The magnetic fields in the external regions can be obtained from Maxwell's equation

$$\mathbf{H} = -\frac{1}{j\omega\mu_0} \nabla \times \mathbf{E}$$

where μ_0 is the permeability of free space and ω is the angular optical frequency.

In the grating region, the periodic permittivity can be expressed in the Fourier expansion

$$\varepsilon_{II}(x, y) = \sum_{g,h} \varepsilon_{gh} \exp\left[jk_0\left(\frac{\lambda}{\Lambda_x}gx + \frac{\lambda}{\Lambda_y}hy\right)\right]$$

The electric and magnetic fields in the grating region can be expressed with a Fourier expansion in terms of the space-harmonic fields

$$\mathbf{E}_{II} = \sum_{m,n} \mathbf{S}_{mn}(z) \exp[-j(k_{xm}x + k_{yn}y)]$$

$$\mathbf{H}_{II} = -j\sqrt{\frac{\varepsilon_0}{\mu_0}} \sum_{m,n} \mathbf{U}_{mn}(z) \exp[-j(k_{xm}x + k_{yn}y)]$$

where ε_0 and μ_0 are the permittivity and permeability of free space, respectively. \mathbf{S}_{mn} and \mathbf{U}_{mn} are the complex amplitudes of the $(m,n)^{\text{th}}$ space-harmonic fields. Finally, by

applying the Maxwell's equation in the grating region and matching the boundary conditions at the interface of the three regions, the unknown amplitudes \mathbf{R}_{mn} and \mathbf{T}_{nm} of the diffracted waves can be determined.

2.3 Results and Discussions

2.3.1 Self-Organized NDAs onto a Substrate

First of all, we started from a 200-nm-Ta film as an interlayer between upper Al and a Si substrate to fulfill a typical PAA process in 0.3 M oxalic acid at 40 V. Figure 2.2 shows the top-view scanning electron microscopy (SEM) image of the porous anodic alumina film after a pore-widening treatment. The self-organized nanopores with a uniform size distribution have a pore diameter about 60 nm and an interpore distance about 100 nm. The pores do not show a long-range order but within a pore array domain. Figure 2.3 recorded chronoamperical curves during the anodization process. At the first stage, the current started high, following a decline as an oxide barrier of PAA formed. The current then reached to a steady level accompanying the growth of pore channel. When the oxide barrier layer at the bottom of the pore approached the Ta–Al interface, anodization of the underlying Ta started. Successively, the currents would decrease gradually and a visible change in color of the sample from metal gloss to charcoal could be observed. Once anodization was completed, the values for current density dropped considerably and remained at a background level.

To investigate the morphological evolution of the resulting structures chronologically, we terminated the anodization process at four different time points, named A, B, C and D in Figure 2.3. After selectively removing upper alumina, the SEM images of these four specimens were displayed in Figure 2.4. It is noted that none of the structure was observed for point A, yet the growth of nanostructure was prohibited. From Figure 2.4b, it is clearly seen that the preliminary tantala nuclei

arose from the scalloped Al concaves as inverted U-shape barrier layer approached the Ta layer. We assume that tantalum nuclei commenced growing at the commencement of current decay. Figure 2.4c reveals the fact that the tantalum nuclei grew and expanded in horizon and vertical. The residual Al metal around the tantalum nanostructures were simultaneously anodized pending it is completely consumed by anodic oxidation. Finally, the cone-like tantalum nanostructures are shown in Figure 2.4d. The average geometric features of tantalum nanodot arrays were a period of 100 nm, a base diameter of 80 nm, a height of 50 nm and a density of $8 \times 10^9 \text{ cm}^{-2}$. During the growth of nanodot arrays (NDAs), the ionic current was distributed unevenly across the barrier layer, concentrating along nanometer sub-channels, which merged inside the hillocks and resulted in appearance of the root-like structure and distorted hexagonal bases. The interpore distance of NDA is in common with the relation $d = -1.7 + 2.81Ua$,⁶³ which d represents the interpore distance and Ua is a constant for the electrolytes of sulfuric, oxalic, and phosphoric acid solutions. Cross-sectional SEM images in Figure 2.5 reveal that an isolated nanostructure was embedded at the bottom of each alumina pore, i.e., at the interface between the porous alumina and un-oxidation Ta.

The aforementioned information inspired us to propose the mechanism of the formation of NDA and illustrate in Figure 2.6. The anodization behavior of the Ta/Al film on the silicon wafer is different from the case of the Al film directly deposited on semiconductor substrates or foil aluminum. In the first instance, the above aluminum layer oxidized to alumina, accompanied by the outward migration of Al^{3+} and inward diffusion of O^{2-} driven by the applied electric field, leading to the vertical pore channel growth. Furthermore, the bottom of the alumina film consisted of an array of convex hemispheres during the initial anodization, and the position of nanodot had been decided. The alumina dissolution at the alumina/electrolyte interface is in equilibrium with the alumina growth at the Al/ Al_2O_3 interface. As the oxide barrier

layer at the pore bottom approaches the Ta/Al interface, the O^{2-} migrating inwards through the alumina barrier layer are continuously injected into the Ta layer and form the tantalum oxide. The O^{2-} released from the dissociated barrier layer at the Ta_2O_5/Al_2O_3 interface are also injected into the Ta_2O_5 layer, while the released Al^{3+} migrate outwards through the remaining barrier layer and are mostly expelled in the electrolyte. The O^{2-} injected into the Ta_2O_5 layer then migrate inwards and the Ta layer is anodized normally to form new oxide at the Ta/ Ta_2O_5 interface. In brief, the underlying tantalum oxide by O^{2-} transported through/from the barrier layer of the initially formed porous alumina without direct contact of Ta with the electrolyte. The tantalum oxide nanodot resulting from oxidation of the Ta layer is accompanied by a volume expansion. Eventually, the aluminum completely transferred into alumina accompanied the end of the all anodic process.

To obtain the insight into the chemical composition of tantalum nanodots, XPS depth profiling analysis was performed for the anodized samples after selectively removing the exposed PAA by mixed chromic and phosphoric acid for 10 min. The bombardment of Ar^+ sputtering was used to examine the inner composition. Each sputter cycle lasted 5 min, which was estimated to remove a 10-nm film of dense anodic tantalum oxide. The measured spectra were calibrated using a Shirley background subtraction. Binding energies were referenced to the carbon-hydrogen peak at 285.0 eV. The Ta^{5+} 4f spectrum consists of two doublet peaks ($4f_{7/2}^{5+}$ and $4f_{5/2}^{5+}$) with binding energies at 26.5 eV and 28.4 eV respectively while Ta^0 4f spectrum consists of two doublet peaks ($4f_{7/2}^0$ and $4f_{5/2}^0$) with binding energies at 21.3 eV and 23.1 eV respectively. Figure 2.7 shows the measured spectrum of the Ta 4f which consists of two doublet peaks ($4f_{7/2}$ and $4f_{5/2}$) have chemical shift relative to the Ta^{5+} state at the handbook of XPS. In the beginning of Ar ion sputtering, the shapes of the Ta 4f doublets gave us an evidence for a mere presence of lower valency oxides in the

film composition. It appeared mostly Ta_2O_5 at the surface of nanodot in anodization [16]. The intensity of the tantalum pentoxide doublet decreases with increasing sputtering time. The shift of the Ta 4f peaks toward to lower valency tantalum oxide with sputtering time increased suggests that there may exist different oxidation states of Ta in the depth of the nanodot in despite of the most stable Ta_2O_5 oxide in anodic tantalum oxidation.⁶⁴ This implies the transition from stoichiometric Ta_2O_5 at the surface to metallic tantalum with the coexistence of different oxidation states of Ta. One assumption of various tantalum oxides is that the oxidation occurred too rapidly to form the most stable oxide state. Supposing that unoxidised tantalum does not remain in the hillock composition, it is likely that the presence of metallic tantalum double peak even at the surface of the unsputtered specimen is consistent with metallic tantalum gaps around the hillocks. Yet, the support by Surganov et al.⁶⁵ indicated that the presence of lower valency tantalum oxides such as TaO, TaO₂ and Ta₂O₃ in the composition of oxide columns formed in similar work. In other words, the top of the nanodot are Ta_2O_5 , and the rest of the nanodot is aluminum-free and composed of tantalum pentoxide mostly and comprises other oxidation states of Ta presumably; the degree of tantalum oxidation decreases from the tops of the nanodot towards the interface.

2.3.2 Antireflection Properties of NCAs on Si

After succeeding in the fabrication of NDA, we associated this nanostructure with another subwavelength nanostructure, so-called “Moth-eye”. The moth eye consists of quasi-close-packed nipples having heights and spacings typically of less than 300 nm, which reduces reflection from their compound eyes. The ARS on the corneas of these insects gradually match the optical impedance of one medium with its neighbour across the interface. We expected NDA may serve as an antireflection structure. However, the present NDA suffered from some problems as follows. First,

the moth eye usually consists of a larger height and a closer arrangement. Further and more even importantly, the un-oxidized Ta layer must be removed. Therefore, we attempt to reduce the thickness of Ta layer and to alter our anodization parameter such as the applied voltage or the electrolyte.

We found, occasionally, a satisfied outcome appeared when the sample composed of Al/30-nm-Ta/Si was anodized in 0.5 M H₃PO₄ electrolyte and an applied voltage of 100 V. Figure 2.8 shows slide-view SEM images of NCAs at various anodization periods. The insufficient anodization in Figure 2.8a was incapable of forming the close-packed arrays. Also, tantalum bulges jutted out over the residual aluminum, exhibiting a poor antireflection property. This observation is attributed to the Al residue from the incomplete anodization. In contrast, the cone-like structures after an adequate anodization time with a $2 \times 10^9/\text{cm}^2$ density in Figure 2.8b demonstrate an intensely dense arrangement with an average diameter of 200 nm and an average height of 200 nm. The close-packed cone-like structure of 200 nm period, which is the surface-relief grating with a period smaller than the incident light wavelength, behaves as an advantaged AR surface. A glance at the horizontal projection of NCA bases manifests a distorted hexagon rather than a circle that occurs in most metal-oxide nanostructures under PAA. Furthermore, the steric structure manifests a pyramidal or a cone-like shape distinct from other reports.^{9,20} Figure 2.8d shows cross-sectional TEM image of the bottom of the alumina pores. An isolated NC was embedded at the interface between porous alumina and the underlying layer.

The anodization mechanism for formation of cone-like tantalum structures was presented as follows. The top aluminum layer in Figure 2.9a is oxidized to alumina, accompanied by the outward migration of Al³⁺ and inward diffusion of O²⁻ driven by the applied electric field, leading to the vertical pore channel growth. As the oxide barrier layer at the bottom of the pore approaches the Ta/Al interface, the O²⁻

migrating inwards through the alumina barrier layer is injected into the Ta layer and the tantalum oxide nanodot is formed as the released Al^{3+} migrating outwards through the remaining barrier layer are expelled, for the most part, into the electrolyte (see Figure 2.9c). The growth of the tantalum oxide nanodot resulting from the continuously injecting O^{2-} accompanies the volume expansion of anodic oxidation while the barrier layer is simultaneously thinned by the wet etching of the phosphoric acid. The continuous consumption of the adjacent aluminum enhances the expansion of nanodots and, simultaneously, is accompanied by dissolution of the barrier layer until the electrolyte contacted the top of nanodots directly without a barrier alumina layer (see Figure 2.9c). The direct contact of tantalum with the electrolyte causes further oxidation of tantalum. Although the top of the nanodots can reach the electrolyte, the residual alumina of sideward pores blocks the growth of the base part of the nanodots. As a result, a cone-like nanodot array appeared, as shown in Figure 2.9d. We are unaware of any other report describing the fabrication of nanostructure arrays for an antireflection purpose, especially with a self-organization approach.

Figure 2.10 shows XPS depth profiles of tantalum oxide NCAs on silicon substrates. Ar^+ sputtering of 5 and 30 minutes was used to examine the inner composition of solid and hollow NCAs. Each sputter cycle lasted 1 min, which was estimated to remove a 2-nm film of dense anodic tantalum oxide. The measured spectra were calibrated using a Shirley background subtraction. Binding energies were referenced to the carbon-hydrogen peak at 285.0 eV. The Ta^{5+} 4f spectrum consists of two doublet peaks ($4f_{7/2}$ and $4f_{5/2}$) with binding energies at 26.5eV and 28.4 eV, respectively. The analysis of both reveals that the Ta 4f lines are almost composed of Ta^{5+} 4f peaks, which indicates the formation of tantalum oxide referred to as stoichiometric Ta_2O_5 .

We prepared various samples with bare silicon, 200 nm tantalum oxide thin film,

and a tantala NCA for antireflection evaluation. Figure 2.11 shows the reflection spectrum as a function of the wavelength with different surface texturing structures. The surface of silicon and tantalum oxide without nanostructure exhibits a strong reflection. Interestingly, the surface with the NCA morphology demonstrates better antireflection performance than the film structure. This observation suggests that the cone-like array of tantalum oxide in nanometer dimension possesses a more graded index property than the thin film structure with the abrupt index. By means of the con-like structure, the reflectance of film is uniformly reduced to below 10% in the wavelengths between 300 and 900 nm. In addition to a better antireflection property, the tantalum oxide materials also exhibit better corrosive tolerance and thermal oxidation tolerance than the well-known silicon-based materials.

2.3.3 Design of Artificial Hollow NCA for High-Performance Optics

Apparently, the foregoing tantala NCA is incapable of a good antireflection result to silicon substrate. Tantalum oxide has a similar refractive index to that of alumina nitride (AlN). Thus, we supposed that tantalum oxide NCA may be the excellent antireflection structure for AlN substrate. We prepared six species from different t_{Ta} ranging from 7 to 30 nm to demonstrate how the hollow interiors of the NCAs affect the reflectivity. An integrating sphere was used in the measurement to collect the diffuse and specular reflectance from all directions (Figure 2.12). Interestingly, the hemispherical reflectance of the NCAs increases upon increasing the hollow portion of the NCA. These results brought us a great curiosity over what was the difference.

Figure 2.13 recorded chronoamperical curves during the anodization of Al on AlN substrates within t_{Ta} (the deposited thickness of Ta film) = 0, 10, and 30 nm which represented the growth of general PAA, hollow NCA and solid NCA, respectively. At the first stage, the current drops were initially due to barrier layer formation, followed by an escalation in current. During anodization of Al/AlN sample,

it is known that the current saturated after the alumina barrier had reached the interface, and an inverted U-shape was formed.⁶⁷ For Ta interlaid samples, when the oxide barrier layer at the bottom of the pore approached the Ta–Al interface, anodization of the underlying Ta started. Since Ta has higher ionic conductivity than Al (comparing 1.8 nm V^{-1} with 1.0 nm V^{-1} for Ta_2O_5 and barrier layer of Al_2O_3 under similar anodization),⁶⁸ anodic tantalum oxide forms preferentially and responds by an increasing surge of current density. The increase in t_{Ta} brings the larger current density due to better conductivity and, of course, brings the shorter anodization time. Successively, the currents would decrease gradually and a visible change in color of the sample from opaque to transparency could be observed. Once anodization was completed, the values for current density dropped considerably and remained at a background level. It should be noted that chronoamperical curves of the anodization in corresponding t_{Ta} on insulating glass, AlN and sapphire substrates revealed an identical feature and magnitude, which depended on the electric conductivity of substrates.⁵⁹

As shown in Figure 2.14, the average geometric features of our tantala NCAs were a period of 200 nm, a base diameter of 200 nm, a height of 200 nm and a density of $2 \times 10^9 \text{ cm}^{-2}$. These quasi-closely-packed taper nanostructures, featuring a surface-relief grating and a period smaller than any of the wavelengths of visible light, served as Moth-eye structures. Cross-sectional TEM images reveal that clearly recognizable hollow-to-solid nanocones formed from Ta films that had initial thicknesses of 10 (Figure 2.14c), 20 (Figure 2.14d) and 30 nm (Figure 2.14e), respectively. An isolated nanostructure was embedded at the bottom of each alumina pore, i.e., at the interface between the porous alumina and the substrate. The tilt and cross-sectional images of NCAs display the tapered profile which benefits the gradient change in refractive index. A decline in porosity with increasing thickness of

initial Ta is found, which corresponds to an increase in solid part of tantalum oxide. The outer morphology of nanocones is almost the same from electron microscopy observation.

Currently, the mechanism of metal-oxide nanostructures formed between the pores of PPA and the substrate was referred to the oxidation of metal layer.^{14,59,69} The O^{2-} ions migrating inward through the alumina barrier layer were injected into metal layer and the metal-oxide nucleus was formed as shown in Figure 2.15a. The growth (volume expansion) of the metal-oxide nanostructure resulted from the continuous combination of O^{2-} and metal ions. However, unlike those cases of solid nanostructure, our thin metal film of $t_{Ta} = 10$ nm was insufficient for oxidation. The excessive O^{2-} ions, relative to the limited Ta^{5+} ions, combined themselves to release O^2 gas at the anode. The gaseous O^2 , acting as a porogen, exerted great pressure to expand the tantalum oxide hillocks and left a void between them and the underlying substrate (Figure 2.15b). The stress produced by the oxygen was observed in the formation of the void under the pore of anodic PPA.⁷⁰ As the voids expanded as a result of the effects of gaseous O^2 , the barrier layers eventually dissolved entirely and the hollow hillocks grew upward. With pore-wall obstructing, the cone-like hollow nanostructures were ultimately obtained (Figure 2.15c). Like our previous report of solid NCA,³⁵ the outer shape of nanocones was not affected by t_{Ta} because it was restricted by the alumina pore-wall. It was, however, dependent on the anodizing parameters. We also noted that the distance between nanocone bases approximates to 0 nm which is much smaller than other similar tantalum nanostructures fabricated by anodization of Al/Ta bilayer.^{12,14-15} We supposed that the key is the deposited thickness of metal film.⁵⁸ Thick metal films (> 100 nm) of previous works lead into the incomplete oxidation of underlying metal, which suppresses the transverse expansion of nanostructures.

The porosity of the hollow nanostructures is tuned by varying the deposited thickness of Ta film. Increasing t_{Ta} from 10 to 30 nm leads to a significant decrease in the porosity of nanocones, which turn into a solid structure from a hollow one as is clearly seen in Figure 2.14c-e. The porosities of hollow nanostructures for the samples of $t_{Ta} = 10$ and 20 nm are estimated to be 69.8% and 35.5% upon TEM images while a solid nanostructure is presented for the sample of $t_{Ta} = 30$. More accurate methods for calculating porosity could be implemented by the Pilling-Bedworth (PB) ratio which is defined as the ratio of the volume of the metal oxide produced by the reaction of metal and oxygen to the consumed metal volume. Assuming all metal Ta was transformed into tantalum oxide a hexagonal close-packed array as shown in Figure 2.14f, the value of R_{PB} is expressed theoretically by the following equation:

$$R_{PB} = \frac{V_{metal-oxide_produced}}{V_{metal_consumed}} = \frac{V_{solid_nanocone}}{V_{Ta_film}} = \frac{Ah(1-P)/3}{At_{ta}}$$

,where A , h , and P are the based area, the height and the porosity of nanocones. R_{PB} of Ta anodization has been reported as 2.3,⁷¹ then the relationship between t_{Ta} and porosity is given by $1 - 0.0345 t_{Ta} = P$. Hence the calculated porosities of $t_{Ta} = 10$ and 20 nm were 65.5% and 31.0% which are in agreement with the values of TEM observations. Knowledge of t_{Ta} and corresponding porosity is needed to determine how much Ta should be deposited initially to obtain a desired porosity that will alter the photonic properties of NCAs.

In order to obtain the insight into the chemical composition of NCAs, XPS depth profiling analysis was performed for the anodized samples after selectively removing the exposed PAA by mixed chromic and phosphoric acid for 10 min. Ar^+ sputtering of 60 and 6 minutes was used to examine the inner composition of solid and hollow

NCA. Each sputter cycle lasted 1 min, which was estimated to remove a 2-nm film of dense anodic tantalum oxide. The measured spectra were calibrated using a Shirley background subtraction. Binding energies were referenced to the carbon-hydrogen peak at 285.0 eV. The Ta⁵⁺ 4f spectrum consists of two doublet peaks (4f^{7/2} and 4f^{5/2}) with binding energies at 26.5 eV and 28.4 eV, respectively. The analysis in Figure 2.16 reveals that the Ta 4f lines are almost composed of Ta⁵⁺ 4f peaks, which indicates the formation of tantalum oxide referred to as stoichiometric Ta₂O₅. Control of t_{Ta} avoids the formation of unoxidized tantalum and sub-oxides (TaO or TaO₂)¹⁵ which are commonly manifested in anodic nanostructures from thick metal films. The measured results confirmed mostly the stoichiometric Ta₂O₅ in the depth of hollow and solid NCAs. Any metal-Ta residual could cause the reduction of antireflective ability.

To understand why the hollow interiors of the NCAs improved the transmission, refractive index profile via different t_{Ta} has to be established (Figure 2.17) by effective medium approximations.¹⁸ As shown in Figure 2.18, the structure was assumed to be a hexagonal close-packed period of 200 nm and a height of 200 nm. We divided the structure into 20 horizontal layers with equal thickness. Based on the effective medium theory, the effective refractive index $n_{\text{eff}}(z)$ of the layer at layer z can be estimated by

$$n_{\text{eff}} f(z) = \{ f(z) \cdot N_{\text{Ta}_2\text{O}_5}^2 + [1 - f(z)] \cdot n_{\text{air}}^2 \}^{1/2}$$

, where $f(z)$ is the fraction of tantalum oxide contained in the layer and equal to $(1-P)$. $N_{\text{Ta}_2\text{O}_5} = n + ik$ is the complex refractive index of tantalum pentaoxide (n and k are optical constants). $n_{\text{air}} = 1$. Therefore, we can calculate the change of effective refractive index at $\lambda = 488$ nm from the surface (height = 0) to the vertex plane of the nanostructure from $t_{\text{Ta}} = 0$ to 30 nm.

The taper structure was assumed to be a hexagonal close-packed period of 200 nm and a height of 200 nm, which was divided vertically in terms of gradient size. For blank AlN substrate ($t_{Ta} = 0$ nm), the n leaps abruptly across the air/AlN interface, causing unnecessary reflection. The gradual change of n from air to substrate is crucial for ideal antireflection properties. The coated sample with $t_{Ta} = 30$ nm exhibits the smoothest n change from the air to the substrate, thereby showing the minimum reflectance. For uncoated glass substrate ($t_{Ta} = 0$ nm), the n leaps abruptly from 1.0 to 1.502 (at 488 nm) across the air/glass interface, causing unnecessary reflection. The gradual change of n from air to substrate is crucial for ideal antireflection properties. The coated sample with $t_{Ta} = 10$ nm ($P = 65.6\%$) exhibits the smoothest n change from the air to the substrate, thereby showing the maximum transmission. In other cases of t_{Ta} , in fact, NCA coatings also provide the graded- n -profile for specific substrates due to the different porosity. For example, a value of t_{Ta} of 5 nm ($P = 82.8\%$), when its effective- n changes continuously from 1.0 to 1.32, is suitable for an MgF_2 substrate. In other words, we can customize antireflection coatings for various substrates based on the corresponding value of initial Ta thickness.

We employed our subwavelength NCAs as antireflection coatings on Pyrex glass substrates. The optical performance of the antireflection surfaces exhibited here was evaluated by transmission, wavelength, and variable-angle reflection measurements. An integrating sphere was used in the measurement to collect the diffuse and specular reflectance from all directions. A 200-nm period satisfies the zero-order condition in glasses considering internal reflections,⁷² and the simulated NCA with a period of 200 nm and a height of 200 nm were optimized to the ideal transmittance from RCWA simulation in Figure 2.19. We used $t_{Ta} = 10$ nm on one side of the substrates to fabricate hollow NCA plus $t_{Ta} = 20$ and 30 nm for comparison; Figure 2.20a provides their measurements with that of bare glass. It is found that not all spectra resulted in

positive antireflection properties in the total transmission across the spectral range from 300 to 900 nm. In the case of 10 nm initial t_a , the transmissions of the glass substrates coated with hollow NCA increased across the whole visible range homogeneously corresponding to a simulated NCA owning a period and height of 200 nm and a porosity of 65% in Figure 4.19b. On account of the reflection of the back side, a double-sided coating of $t_{Ta} = 10$ nm was applied to ideal antireflective properties; it provided an average transmittance of 97.8% and a maximum 98.2% at 480 nm while the transmission of a blank substrate is $< 92.5\%$.

One advantage of having a smooth and continuous gradient in n -profile is that it results in the reflection of incident light over a wide angle.¹⁸ To verify the omnidirectional characteristics, we performed comparisons of specular reflectance as a function of wavelength in the visible range from 400 to 800 nm and angles of incidence from 30° to 70° (Figure 2.20b). Generally, the reflectance for coated or uncoated samples is insensitive to the incidence angle from 0° to 30° . For the incidence angle up to 45° , the specular reflectance of double-sided NCA coatings exhibits a result below 3% over a spectral range from 400 to 800 nm, while it is above 7.5% for a planar glass substrate. Unlike the quasi-thin-film coatings prepared from porous materials or particles, our cone-like nanostructures provide broadband antireflective ability over large incident angles. The average reflectivities of coated and uncoated glasses for an incident angle of 70° are 10.3% and 26.4%, which improved over the whole visible spectrum with an average factor of 16%. The inserted photography in Figure 5a supports the result of antireflection properties with a large tilted angle. Two glass substrates with and without NCA coating were exposed to daylight lamps. The glass substrate on the left (without coating) reveals ghost images from the light for oblique incident angles. On the contrary, the glass at the right side (with coating) demonstrates fine suppression of the light reflection. Also,

the improvement of transmission is identical to a virtual elimination of reflectance over the visible spectrum, which means that no scattering and absorption impairment was caused by the hollow nanostructures.²⁹

We also employed NCAs from $t_{\text{Ta}} = 20$ nm on a sapphire substrate because of the satisfactory antireflection coatings according to the n -profile in Figure 2.20. Additionally, to evaluate the mechanical stability and possible passivation behavior of the NCA coating, a serial test including abrasion, corrosion, and temperature resistance was acquired. The specular reflection was measured at an incidence angle of 5° . The resultant reflectance (Figure 2.21), which reveals a very close value before the treatment, also improves the reflectivity significantly. These findings render strong evidence for advantages in mechanical properties compared to other ARS coatings based on nanoparticle or polymer-corrugation on transparent substrates. We supposed that it is very likely for NCA coatings to be used as general protective coatings for optical transparency. The experimental reflectance is further complemented by theoretical calculation using a 3-D rigorous coupled wave analysis (RCWA) model and agrees reasonably well with the simulated reflectivity on both samples.

2.3.4 TiO₂ NTs and Hollow NCAs for the Improved Efficiency of DSSCs

We overcome the challenges described above by using a 15-nm-thick Ti adhesion layer between the Al and the fluorine-doped tin oxide (FTO). During the Al anodization process, the underlying Ti was oxidized to form hollow TiO₂ nanocone arrays,⁷³ which resulted in stable anodization and suppressed the formation of a thick barrier layer. After using a modified sol-gel process to deposit TiO₂ onto the pore wall of PAA, we developed a versatile technique for fabricating a new photoelectrode architecture consisting of hollow TiO₂ nanocones under PAA with TiO₂ NTs inside. Figure 2.22 provides a schematic representation of such an assembled DSSC device. Herein, we discuss the photovoltaic performance in relation to the electrode geometry.

In many nanostructured electro-optical device designs, the desired configuration features PAA grown directly on a TCO substrate. As mentioned above, anodization of an Al/TCO substrate, in the absence of a retardant layer, suffers from a delamination problem. To solve the problem, we deposited a 15-nm-thick Ti layer between Al and the FTO. Figure 2.23.a presents chronoamperic curves recorded during the anodization of Al on bare FTO glass and on FTO glass coated with a Ti layer. During the first stage, the initial decreases in current were due to barrier layer formation, followed by an escalation in current. When the anodizing time reached *ca.* 60 s, a sudden surge occurred in the current of the Al/FTO sample, accompanied by sparks, gas evolution, and delamination, resulting from anodic breakdown of the FTO. The current then remained at a very high level as a result of direct contact between the FTO and the electrolyte. In contrast, when the 15-nm-thick Ti layer was present, the anodization current was noticeably stabilized, allowing anodization to proceed smoothly down to the substrate. Because Ti has a higher ionic conductivity than Al, anodic titanium oxide formed preferentially, resulting in an increasing surge of current density. Once a visible change in color of the sample, from opaque to transparent, had occurred, the current density dropped to the base level. Figs. 2.23.b and c display photographs of the final samples. Several obvious defects appear on the Al/FTO sample. The regions of limpid appearance were bare FTO; the dissolution reaction escalated as more areas of the FTO glass were exposed, causing eventual delamination of PAA from the FTO glass. The regions with residual Al featured a metallic color. The complete formation of PAA resulted in the uniform transparency of the Al/Ti/FTO sample, which featured appropriate adhesion of PAA to the FTO substrate for the fabrication of DSSC devices.

Figure 2.24a presents a top-view SEM image of self-organized hollow TiO₂ nanocones after removing the upper alumina layer. The average geometric features of

the quasi-closely-packed nanocone arrays were a period of 200 nm, a base diameter of 180 nm, and a density of $2 \times 10^9 \text{ cm}^{-2}$. We used an FIB milling technique to expose the inner portion of the nanocones. The left-hand region in the image reveals 20-nm-thick shells with a hollow interior. As the anodization process was completed, TiO₂ hollow nanocones were also formed in the bottom of PAA pores. The upper PAA was selectively removed, subsequently, the sample was conducted in a furnace with a heating rate of 2 °C /min and kept at 450 °C for 5 h to crystalize into anatase TiO₂. A blank FTO substrate was used as a reference. Pronounced peaks of anatase TiO₂ were observed, which confirms that these nanostructures were composed of anatase TiO₂ (Figure 2.25). We expected that such transparent hollow TiO₂ nanostructures organized on TCO glass as an electrode would increase the contact area with the TCO substrate and, hence, provide efficient electron transport.⁷⁴ Films constructed of oriented one-dimensional nanostructures aligned perpendicular to the collecting TCO substrate could also improve the charge-collection efficiency by promoting faster transport and slower recombination.⁷⁵ Furthermore, in many PAA-based solar cells, NTs attached directly to TCO glass result in electrical shorting when the redox electrolyte came into direct contact with the TCO layer; in contrast, we expected our nanocone layer to serve as an insulating layer to avoid direct contact between the electrolyte and the TCO glass.

We used TEM to investigate the morphologies of the contact interfaces between the nanocones, the substrate, and alumina wall (Figure 2.24b). An isolated hollow nanostructure was embedded at the bottom of each alumina pore, i.e., at the interface between the porous alumina and the substrate. Notably, no barrier layer was evident—a very advantageous situation for the subsequent deposition of TiO₂ NTs. The PAA was aligned perpendicular to the substrate, with self-organized hollow TiO₂ nanocones at a height of 150 nm. We suspected that having the ability to control the

nanoscale architecture of the TiO₂ network would positively impact solar cell performance by providing more-direct migration pathways with improved charge transport efficiencies, as well as simplified device architectures.⁷⁶ Template-directed synthesis is an ideal tool for fabricating oxide NTs because their physical dimensions can be controlled precisely and monodisperse samples can be harvested in large quantity. Our PAA template consisted of well-aligned, uniform, cylindrical pores, with good adhesion to the FTO glass, making them highly suitable for subsequent TiO₂ sol-gel synthesis.

Combining the chronoamperical data with the microscopy images, Figs. 2.24c–e presents a proposed mechanism of formation for the TiO₂ nanocones. If a metal whose oxide form has a higher ionic conductivity than alumina was used as an underlayer preceding an Al anodization process, the underlying metal would be also oxidized and thereby form metal-oxide nanostructures with a similar pattern as the upper PAA.⁷⁷⁻⁷⁸ Metal-oxide nanostructures formed between the pores of PAA and the substrate are referred to as the oxidation of metal layer. The O²⁻ ions migrating inward through the alumina barrier layer were injected into the metal layer, forming the metal-oxide nucleus (Figure 2.24c). When the anodization front approached the Ti–Al interface, anodization of the underlying Ti began. The O²⁻ ions migrating inward through the alumina barrier layer were injected into the Ti layer, forming a tantalum oxide nucleus. The growth (volume expansion) of the tantalum oxide nanostructure resulted from the continuous combination of O²⁻ and Ti⁴⁺ ions. We found, however, that the excess of O²⁻ ions, relative to the limited amount of 15-nm-thick Ti, combined to release O₂ gas at the anode. The gaseous O₂, acting as a porogen, exerted great pressure to expand the tantalum oxide hillocks, leaving a void between them and the underlying substrate (Figure 2.24d).⁵⁸ The stress produced by O₂ gas resulted in the formation of a void under each pore of the anodic PAA.⁷³ During the formation of titania nanocones, the

alumina wall and barrier were continuously thinned by H_3PO_4 electrolyte itself. As the voids expanded, as a result of the effects of gaseous O_2 , the barrier layers eventually dissolved entirely and the hollow hillocks grew upward. With the obstructing pore wall, cone-like hollow nanostructures were ultimately obtained (Figure 2.24e).

A typical sol solution of $\text{Ti}(\text{O}i\text{Pr})_4$ includes both EtOH and water, plus a variety of other additives. The water acts to hydrolyze $\text{Ti}(\text{O}i\text{Pr})_4$, leading to the formation of TiO_2 particulates in solution through a series of condensation reactions, which, when brought to completion, result in the formation of the gel. Figs. 2.26a and b display top-view SEM images of PAA before and after performing the $\text{Ti}(\text{O}i\text{Pr})_4$ sol-gel process. The average geometric features of blank PAA were a period of 200 nm, a height of 800 nm, and a density of $2 \times 10^9 \text{ cm}^{-2}$. Hollow TiO_2 gel structures were formed within the pore walls of the PAA; the pore diameters in these two images (ca. 160 and 120 nm, respectively) suggest that the wall thickness of the deposited TiO_2 NTs was ca. 20 nm. The TiO_2 NT layer adhered to the pore wall tightly without forming cracks. Thus, the TiO_2 sol flowed into the pores along the pore wall of the PAA through an infiltration process, due to surface tension and capillary effects. Notably, the affinitive treatment in EtOH for PAA was a necessary step for achieving hollow TiO_2 gel structures; otherwise, shrinking or cracking would occur to separate the NTs from the pore walls during the subsequent heating process.

Figure 2.26c reveals that TiO_2 NTs were hollow and grew along the PAA template to self-organize into hollow TiO_2 nanocones. With the aid of PAA, the TiO_2 NTs were formed without the bundling or microcracking that has been reported previously.⁵¹⁻⁵² This architecture allows electrons to transfer in a more direct route through the well-aligned pathways of the TiO_2 NTs, presumably improving the performance of the DSSC. The arrangement of the highly ordered TiO_2 NT array perpendicular to the surface permits facile charge transfer along the length of the NT

from the solution to the conductive substrate, thereby reducing the losses incurred by charge hopping across NP grain boundaries. Easier access to the NT array surface, as well as better control of the interface, makes this morphology desirable for DSSCs. Enhanced electron transport also allows improved light harvesting because thicker films can be used to increase the optical density, thereby improving the absorption of low-energy photons in the red and infrared spectral regions without losing the additionally harvested charge carriers to recombination.

Anatase-phase TiO_2 is a good candidate for use as a photoelectrode. We converted the as-deposited amorphous TiO_2 NTs to the anatase phase by annealing the sample at 450 °C in O_2 for 5 h. Notably, GIXRD analysis (Figure 2.26d) provided no evidence of the rutile phase. The enhanced (101) peak at a value of 2θ of 25.3° reveals that the NTs were well crystallized. An average crystallite size of 28 nm was estimated from the Scherrer equation.

We investigated the effect of the electrode morphology on the performance of DSSCs by comparing cells featuring different working electrode structures: hollow TiO_2 nanocones under porous alumina and TiO_2 NTs (NT-A-NC); a TiO_2 film under porous alumina and TiO_2 NTs (NT-A); and anodic TiO_2 NTs without alumina. A TiO_2 film was substituted for TiO_2 nanocones under porous alumina in sample NT-A-NC (Figure 2.27a). The TiO_2 film electrode was prepared by the sol-gel spin-coating method (Figure 2.27b). Titanium isopropoxide (5 mL) was added to absolute EtOH (25 mL) maintaining the temperature at 1 °C. Separately, water (0.5 mL) and 0.1 mol/L HCl (0.5 mL) were added to EtOH (25 mL). Thereupon, the $\text{Ti}(\text{O}i\text{Pr})_4/\text{EtOH}$ sol was slowly added to the EtOH/HCl/ H_2O mixture. The resulting gel solution then was spun onto FTO substrates. After drying in air at room temperature, the sample was placed in a furnace, heated at a rate of 2 °C/min up to 450 °C, and held at that temperature for 5 h. An only Al film was deposited onto TiO_2/FTO substrate after.

Anodic TiO₂ NTs (Figure 2.27c) were substituted for sol-gel TiO₂ NTs within PAA in samples NT-A-NC and NT-A. The anodic TiO₂ NTs were prepared by direct anodization of Ti film (800 nm) deposited onto FTO substrate (Figure 2.27d). The anodizing process was performed in an electrolyte of 0.25 wt% NH₄F and ethylene glycol (99.8% anhydrous) solution at a constant voltage of 60 V. The sample was then placed in a furnace, heated at a rate of 2 °C/min up to 450 °C, and held at that temperature for 5 h. Samples NT-A-NC and NT-A allowed us to discern the effect of the hollow TiO₂ nanocones; samples NT-A and NT allowed us to verify the role of the anodic aluminum oxide in the DSSC. The standard back contact used was FTO glass; the standard counter electrode was Pt-coated FTO glass. A panchromatic sensitizer, N719 dye, was used as the standard dye; the standard high-boiling-point iodide-based electrolyte (in MPN) was employed. Photovoltaic measurements were performed using an AM 1.5 solar simulator equipped with a 150-W Xe lamp; the power of the simulated light was calibrated to 100 mW/cm². The photocurrent (*I*) and photovoltage (*V*) of the cell were measured over an active area of 0.25 cm².

Figure 2.28a displays representative current-voltage (*I*-*V*) data for the DSSCs; Table 5.1 lists the photovoltaic performance parameters. For sample NT-A-NC, the device exhibited an open-circuit voltage (*V*_{oc}) of 0.64 V, a short-circuit current density (*J*_{sc}) of 5.15 mA/cm², and a fill factor (FF) of 0.59, giving an overall power conversion efficiency (*η*) of 1.71%. For sample NT-A, of which the TiO₂ film replaced the TiO₂ nanocones as the electrode, these values were all lower. Thus, the hollow TiO₂ nanocones played a predominant role in enhancing the photoconversion efficiency. We suspect that the nanocone structures increased the contact area with the TCO substrate, thereby enhancing electron transport, as reflected by the higher value of *J*_{sc}.⁷⁵ A recent study has revealed that hollow TiO₂ can greatly enhance the photocatalytic activity or photoelectric conversion efficiency as a result of the

multiple reflection of light;^{74,76} for the same reason, we believe that the larger value of J_{sc} for sample NT-A-NC arose from enhanced light harvesting, due to multiple light reflection and scattering between the shells of the self-organized hollow TiO₂ nanocones. In addition, the electron transport path through a hollow cone-like electrode is different from that in a thin film. Because the electrons transferred from the NTs to the FTO layer along the thin TiO₂ shell, this structure provided shorter and more-direct transport paths for electrons, compared with those for the TiO₂ film in sample NT-A, resulting in a greater value of V_{oc} .⁷⁵

To verify the role of porous alumina in DSSC, we compared the performances of sample NT-A (with PAA) and sample NT (without PAA). Because the outer TiO₂ NTs were shielded by the inner PPA wall from the redox electrolyte, the rate of recombination in the NT-A structure was reduced. Sample NT-A resulted in a 20% improvement in efficiency, from 1.22 to 1.45%, revealing that the porous alumina acted as an insulating barrier between the TiO₂ NTs and the dye/electrolyte interface. Furthermore, clumps and cracklike features in TiO₂ NTs have, in fact, been observed (Figure 2.27d). Clusters of bundled TiO₂ NTs could be produced during the anodization of Ti, thereby slowing down the electron transport dynamics in the electrodes. In contrast, with the aid of PAA, the TiO₂ NTs were presented without any bundling or microcracking, thereby providing electrons with a direct pathway toward the FTO glass.

Figure 2.28b presents action spectra for the IPCEs of the DSSC devices featuring the three different electrode structures. IPCE is defined as the number of generated electrons divided by the number of incident photons. Basically, the IPCE intensities were systematically enlarged upon the same dye coinciding with the performances listed in Table 2.1. The IPCE spectra exhibited a peak of ca. 26% at 530 nm, as well as an inflection point at 430 nm, in relatively close agreement with the expected

maximum based on the accompanying absorption spectrum for the N719 dye, which has local maxima at 377 and 526 nm, both corresponding to a metal-to-ligand charge transfer transitions (Figure 2.29). The absorption band in the UV region is due to the intraligand charge transfer transitions (ILCT). Also, the electronic absorption spectrum of N719 shows the characteristic metal-to-ligand charge-transfer transition (MLCT) absorption bands in the visible region at 527 nm. When PAA was applied to the thin-film electrode devices, the IPCE peak height at 530 nm increased from 16 to 21%; the presence of the nanocone electrode promoted the value from 21 to 26%.

The photovoltaic performances of these DSSC devices are similar to those of DSSCs featuring the same N719 dye and a titania NT electrode fabricated through deposition in a commercial PAA template. Note that the average length of the titania NTs in commercial PAA was greater than 20 μm ; i.e., they were much longer than the ones we prepared in this study. In general, higher efficiencies result when using NTs of greater lengths. For example, Varghese et al. found that the power conversion efficiency improved from 2.6 to 6.9% when the average length of the titania NTs increased from 1.2 to 20 μm . Therefore, we believe that the improvement in the power conversion efficiency of our cells resulted from the formation of uniform Al films (tens of micrometers thick) on the FTO glass. Also, the TiCl_4 treatment to NTs is able to enhance the photogenerated current and the power conversion efficiency.⁴⁷

2.4 Summary

We have investigated tantala nanodot and nanocones arrays through the fundamental research. Artificial Moth-eye structures by using hollow-to-solid nanocones were successfully fabricated for high-performance AR coatings. Quasi-closely packed arrays of cone-like nanostructures are fabricated by the anodization of Al/Ta bilayers coated on substrates. We proposed the mechanism of

formation of the hollow NCA due to the stress of gaseous O_2 . The porosity of the hollow nanostructures is calculatedly controlled by varying the deposited thickness of Ta film. The transmissions of the glass substrates coated with hollow NCA of 65.5% porosity reached greater than 97.8% over the whole visible range. Besides, the reflectivity was suppressed greatly in a broadband omnidirection and reached as low as 10% at an incident angle of 70° . In other cases of porosity, NCA coatings were also found as an efficient ARS on sapphire and AlN substrates. Good mechanical stability makes NCA suitable for protective coatings for optical transparency. The availability of the hollow nanostructures has allowed the design of artificial optical properties as new building blocks (e. g. diffractive layer, diffusers, or reflectors) in future photonic devices.

Moreover, we also have fabricated hollow TiO_2 nanocones under PAA featuring TiO_2 NTs within directly on FTO glass and used them as new working electrodes in DSSCs. By depositing a thin layer (15-nm-thick) of Ti on a FTO substrate prior to anodization, we obtained self-organized hollow TiO_2 nanocones, with improved contact between the FTO substrate and the overlaying Al, thereby solving the problems of delamination of an undesirable barrier. This more-stable PAA/FTO structure was highly suitable for use in subsequent sol-gel processing of $Ti(OiPr)_4$. The novel structure combines two types of TiO_2 materials—0-D nanocones and 1-D NTs—to benefits from a large contact area, direct electron transport path, and slow recombination of electrons. The unique morphology provided a photocurrent of 5.15 mA/cm^2 , an open circuit voltage of 0.64 V, and an IPCE peak of 26% from an 800-nm-thick NT array. The relatively short NT array results in a considerably lower photoabsorption than, for example, the current DSSC “gold standard” featuring a tens-of-micrometers-thick layer of TiO_2 NTs. We suspect that increasing the length of the NT array on the electrode might allow us to further improve the efficiencies of

such DSSCs. The facile synthesis of this novel architecture may allow the design of new nanostructures for use as new building blocks in future electro-optical devices.



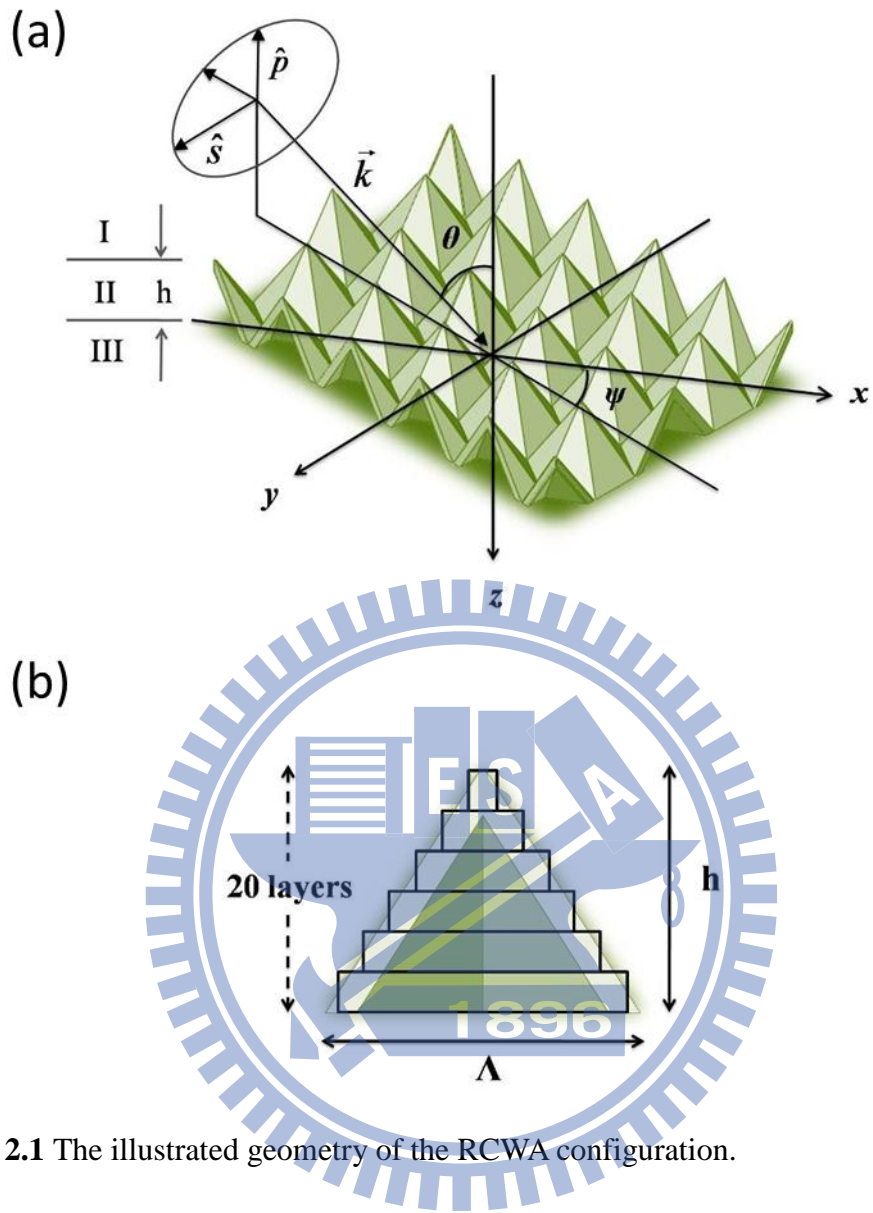


Figure 2.1 The illustrated geometry of the RCWA configuration.

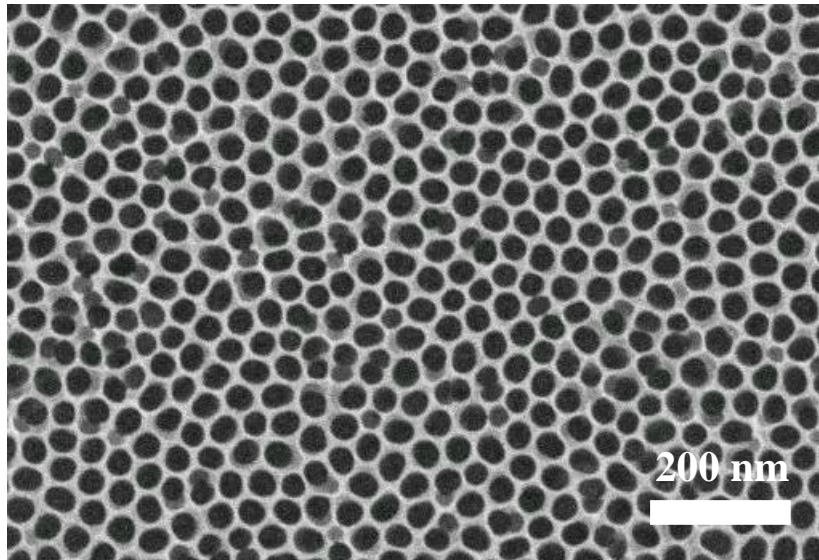


Figure 2.2 Top-view SEM image of PAA film anodizing in 0.3 M oxalic acid at 40 V after a pore-widening treatment.



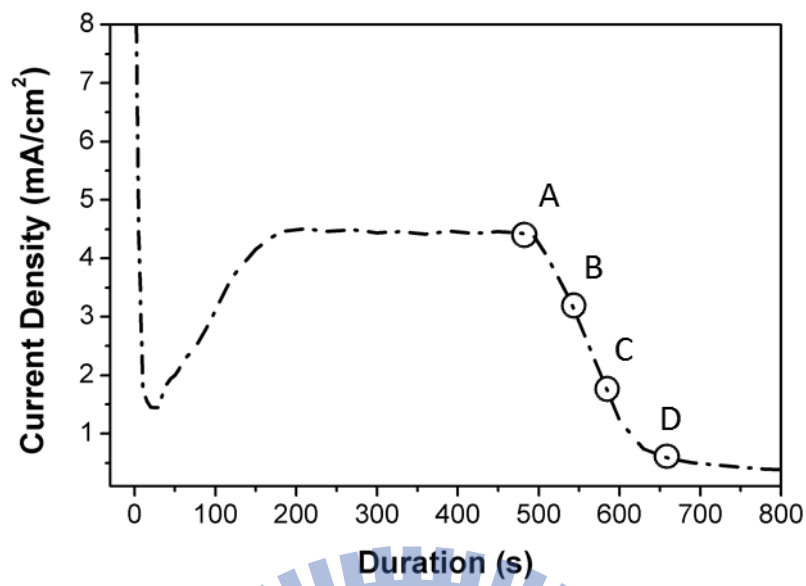
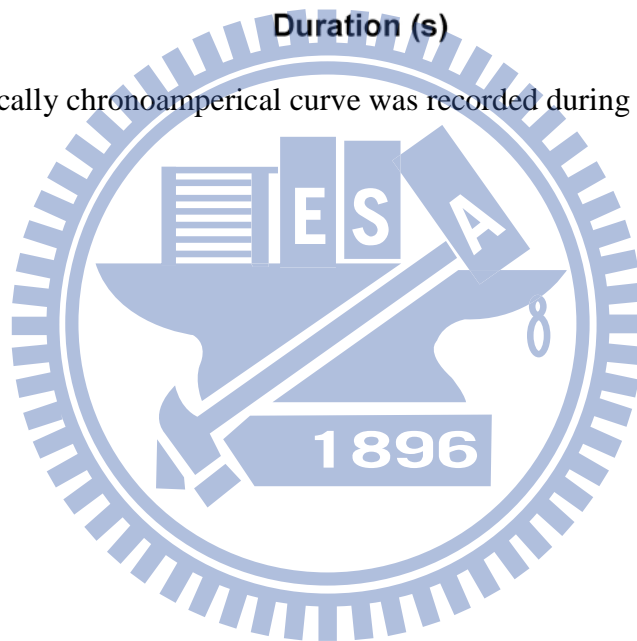


Figure 2.3 A typically chronoamperical curve was recorded during the anodization.



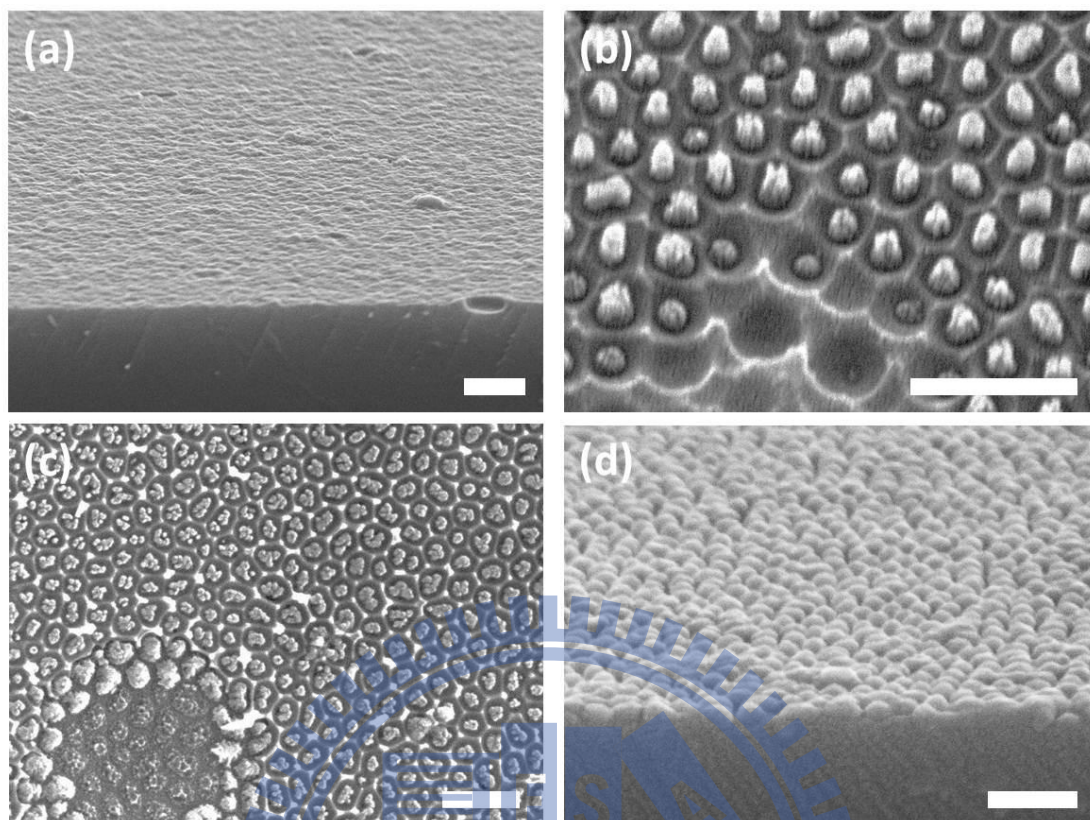
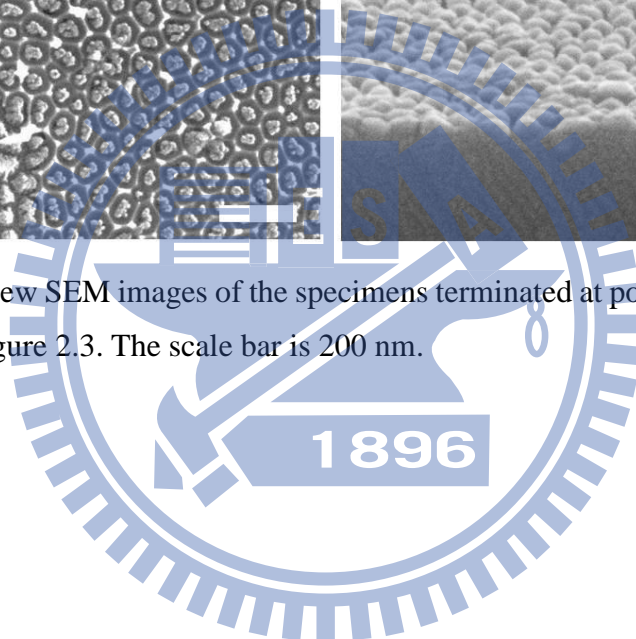


Figure 2.4 Top-view SEM images of the specimens terminated at point (a) A, (b) B, (c) C and (d) D in Figure 2.3. The scale bar is 200 nm.



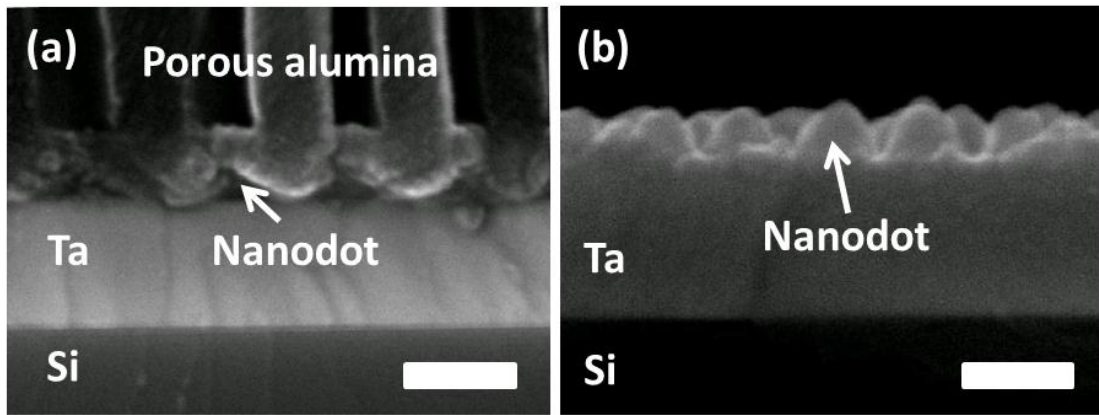


Figure 2.5 (a) Cross-sectional SEM image of the nanodots embedded in porous alumina film. (b) Slide-view SEM image of nanodot arrays after removing alumina film. The scale bars are 100 nm.



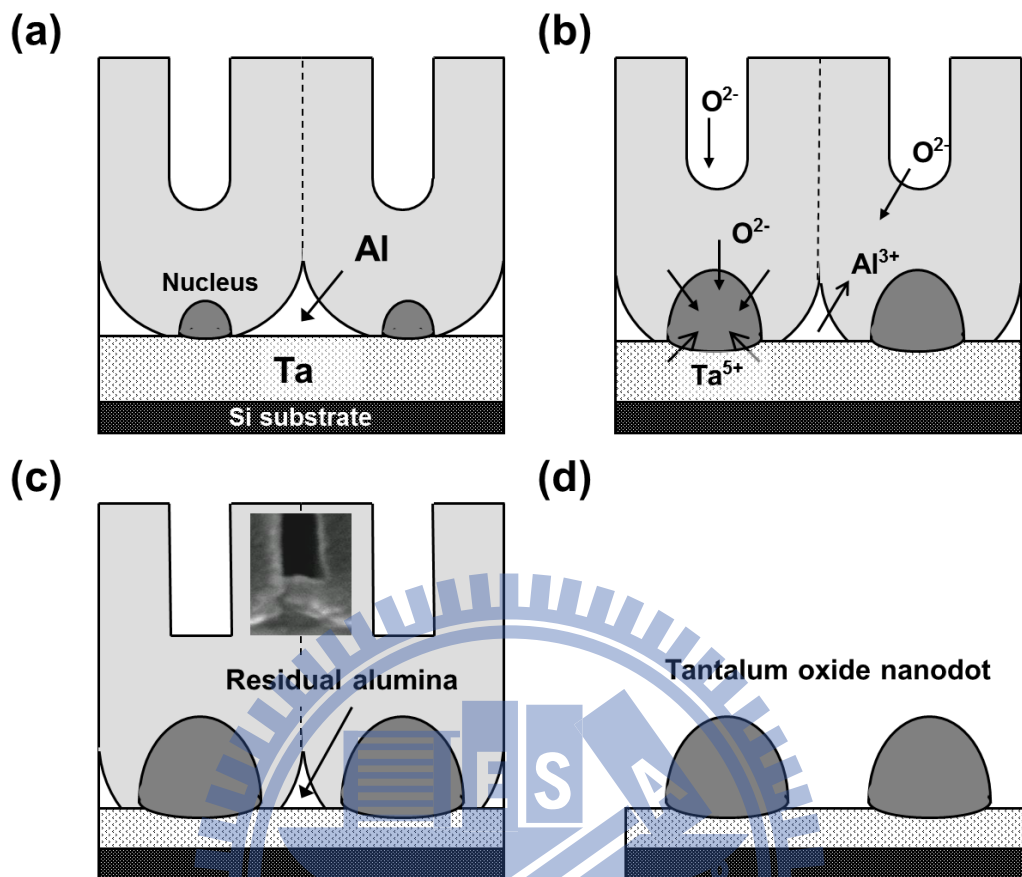


Figure 2.6 Schematic diagrams showing the principal steps of modification of the underlying metal/alumina interface.

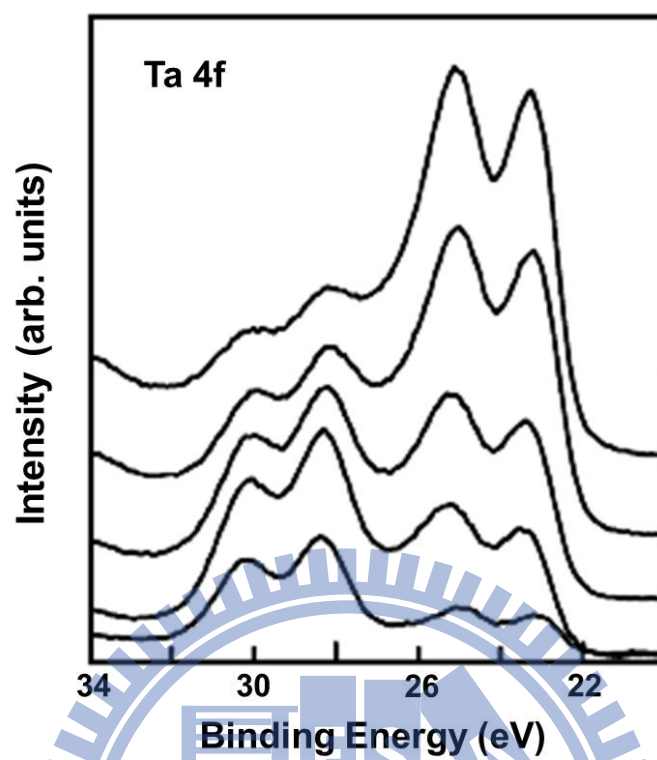


Figure 2.7 XPS depth-profile analysis of Ta 4f spectrum for tantalum oxide nanodots on Si substrates at normal incidence. The bombardment of Ar^+ sputtering was used to examine the inner composition; each sputter cycle lasted 5 min.

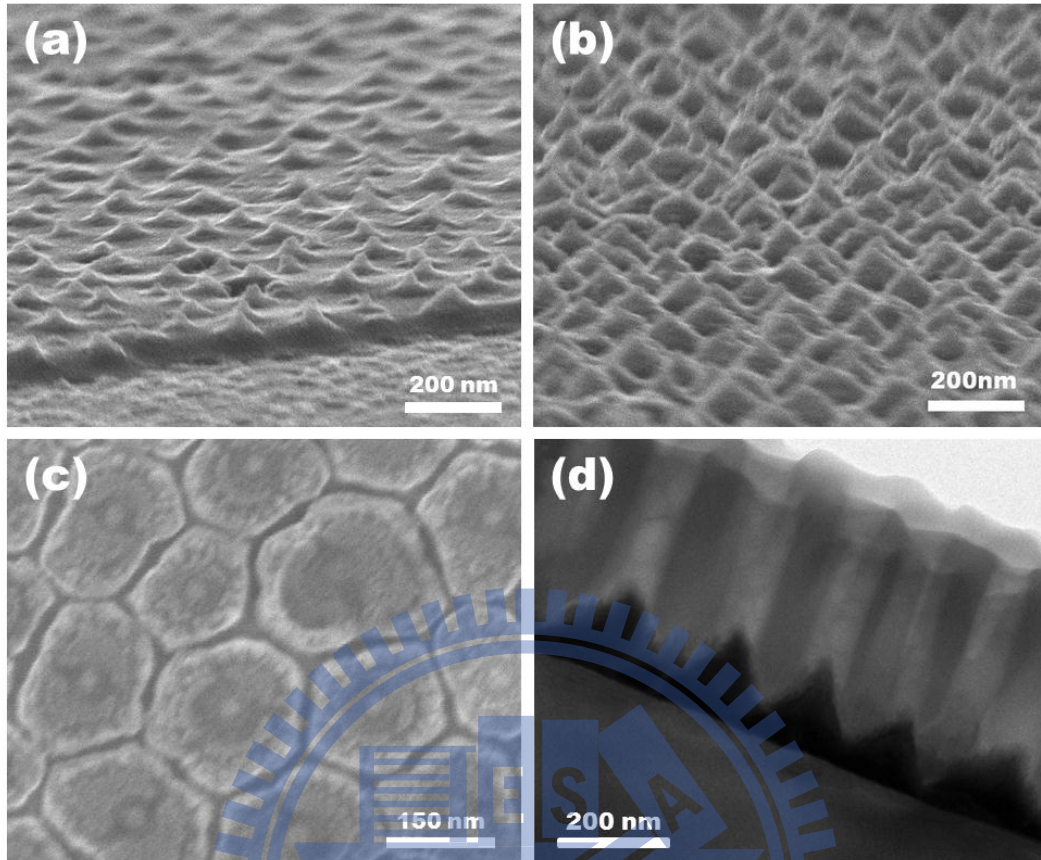


Figure 2.8 (a) Slide-view SEM image of tantalum oxide NCA in unfinished anodization. (b) Slide-view SEM image of tantalum oxide NCA in complete anodization. (c) Top-view SEM image of tantalum oxide NCA. (d) TEM image of the NCA under the porous alumina film.

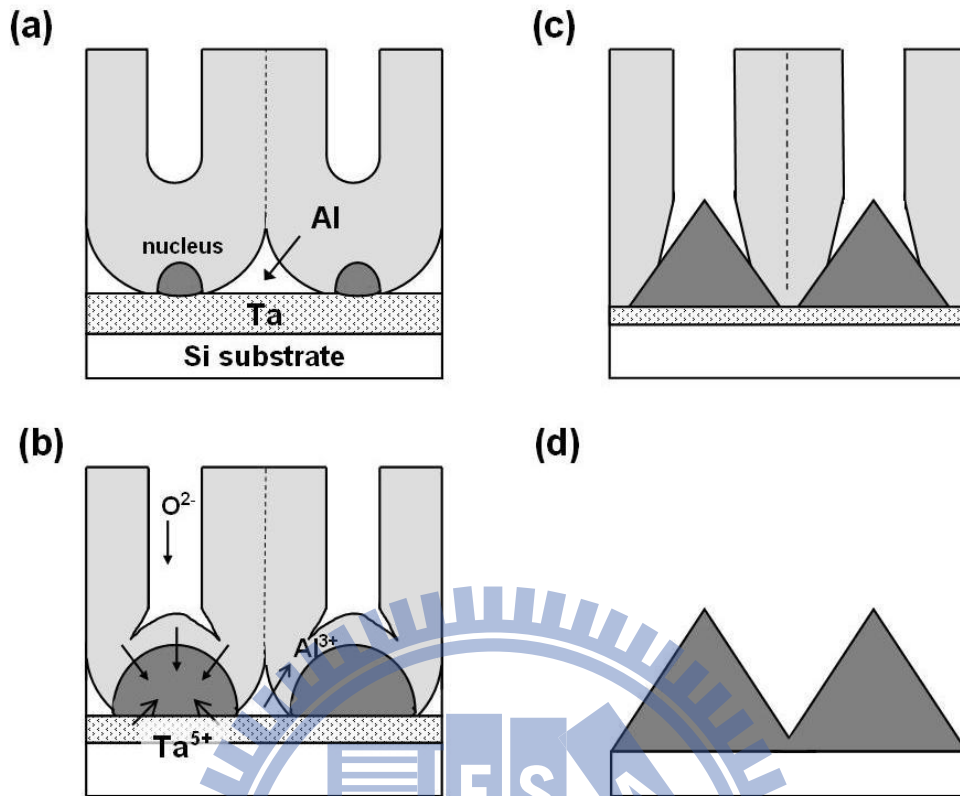


Figure 2.9 A schematic diagram to describe the formation mechanism of the tantalum oxide NCA at the Ta/Al interface.

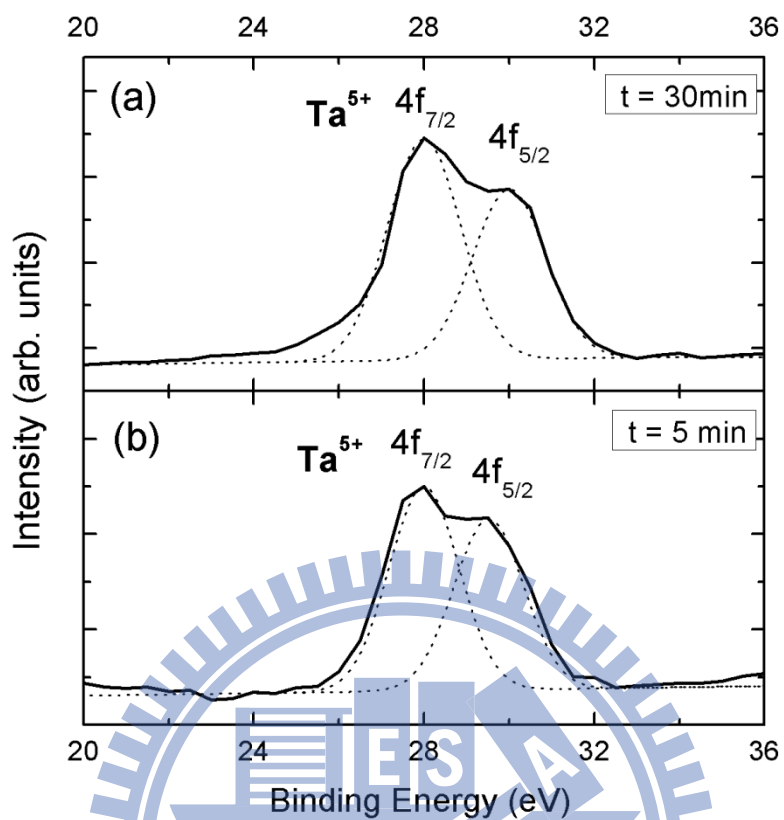


Figure 2.10 XPS depth-profile analysis of Ta 4f spectrum for tantalum oxide NCA on Si substrates at normal incidence. The Ar⁺ sputtering of 5 and 30 min was used to examine the inner composition.

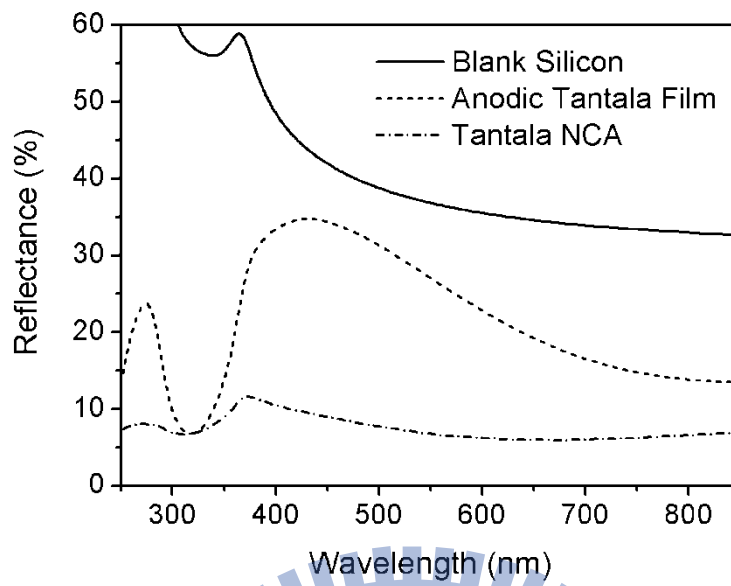


Figure 2.11 The spectroscopic measurements of broadband reflectance for the blank silicon wafer, the anodic tantalum oxide film and tantalum oxide NCA, respectively.



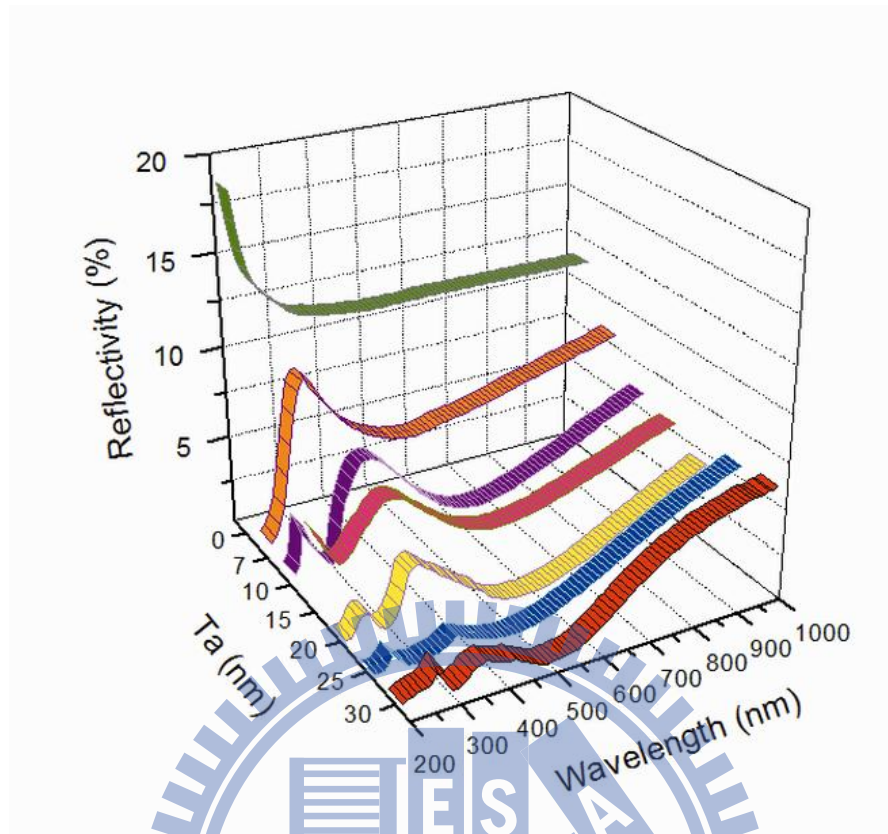


Figure 2.12 Experimental reflectivities of NCAs on AlN substrates, formed from Ta films having dimensions ranging from 7 to 30 nm.

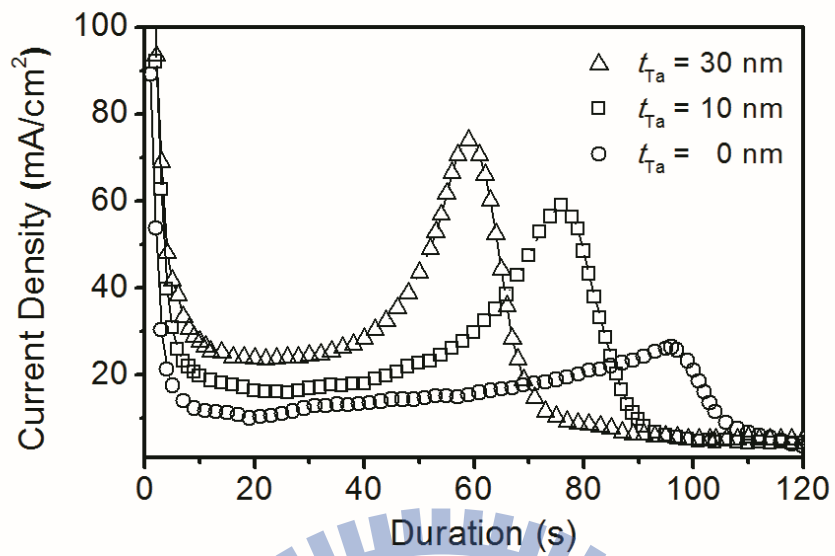
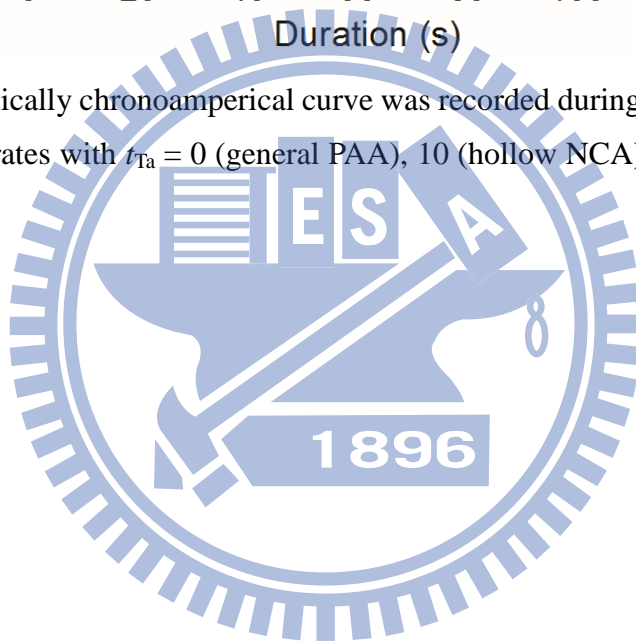


Figure 2.13 A typically chronoamperical curve was recorded during the anodization of Al on glass substrates with $t_{Ta} = 0$ (general PAA), 10 (hollow NCA), and 30 nm (solid NCA).



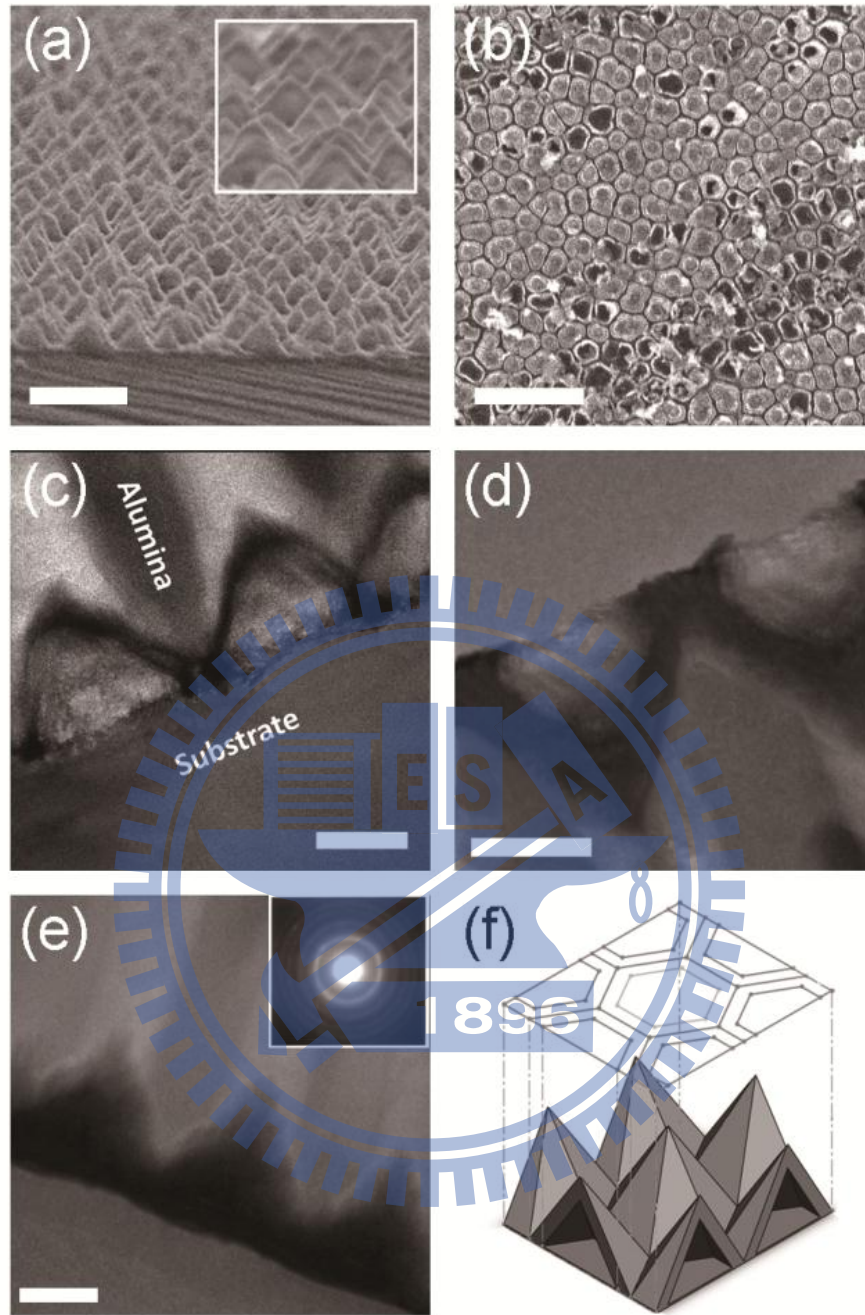


Figure 2.14 SEM and TEM images of cone-like nanostructure arrays. (a) Side-view SEM image (scale bar: 500 nm) of hollow NCA after alumina had been removed selectively. Inset: Magnified image. (b) Top-view SEM image (scale bar: 1 μm) of hollow NCA that had been ground using a diamond emery paper. TEM images of hollow (c), (d) and solid (e) nanostructures under porous alumina (scale bar: 100 nm). Inset (e): SAED pattern revealing the amorphous composition. (f) Schematic representation of a close-packed hexagonal NPC for theoretical calculation: period, 200 nm; base diameter, 200 nm; height, 200 nm.

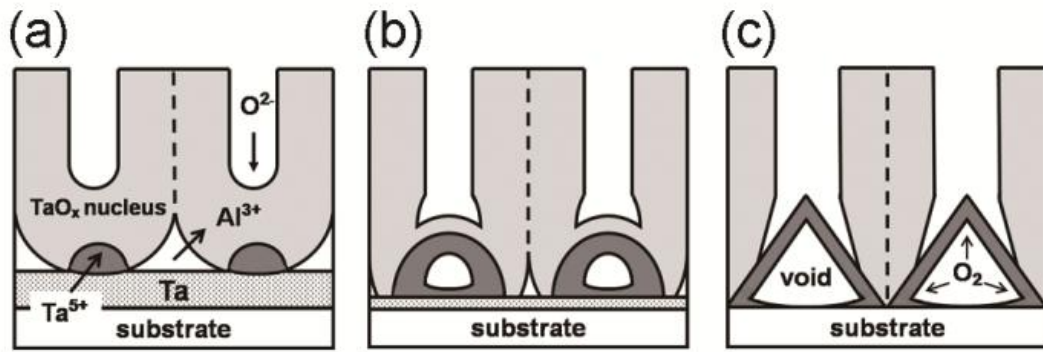
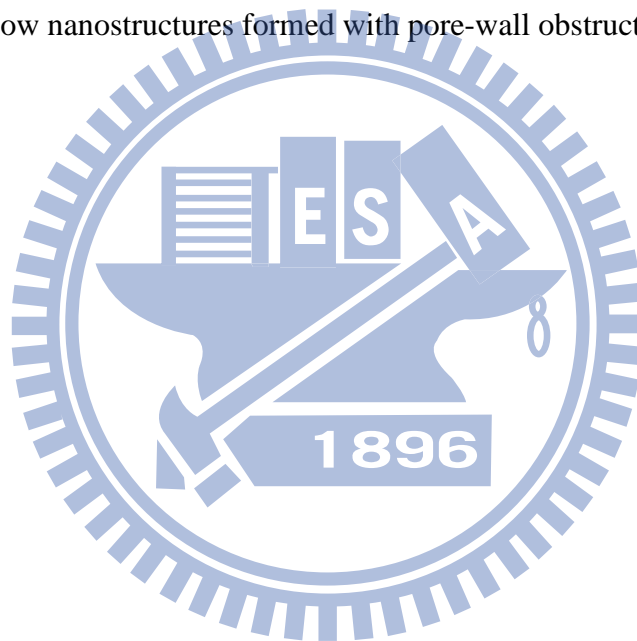


Figure 2.15 Schematic representation of the mechanism of the formation of the hollow nanocones. (a) Tantalum oxide nucleus formed as the anodization approached the Ta–Al interface. (b) Tantalum oxide hillocks grew, leaving voids caused by O₂ pressure. (c) Cone-like hollow nanostructures formed with pore-wall obstructing.



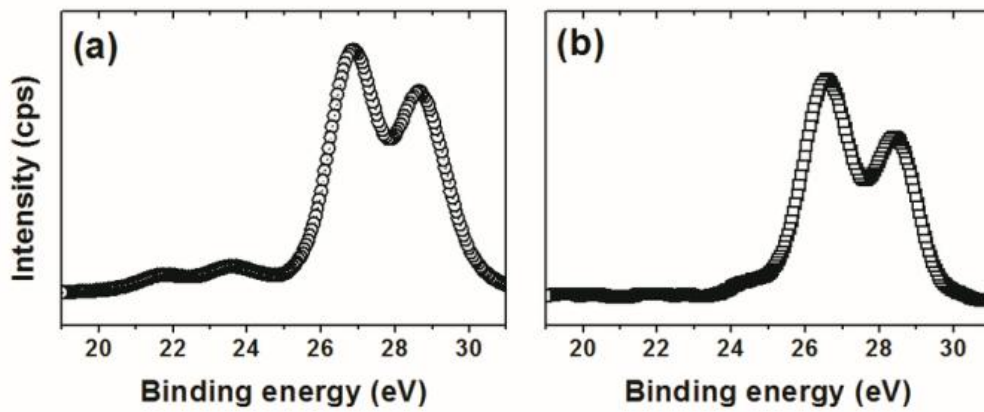
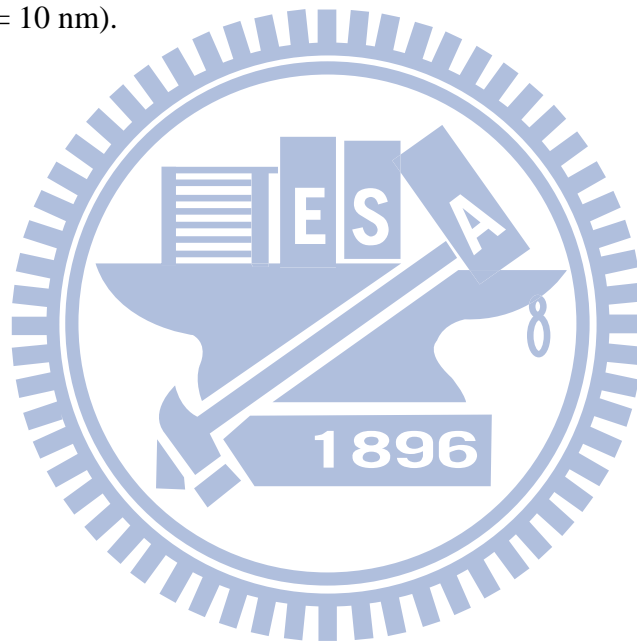


Figure 2.16 XPS depth-profile analysis of tantalum oxide NCAs on glass substrates at normal incidence. (a) Ta 4f spectrum of solid NCA ($t_{\text{Ta}} = 30$ nm); (b) Ta 4f spectrum of hollow NCA ($t_{\text{Ta}} = 10$ nm).



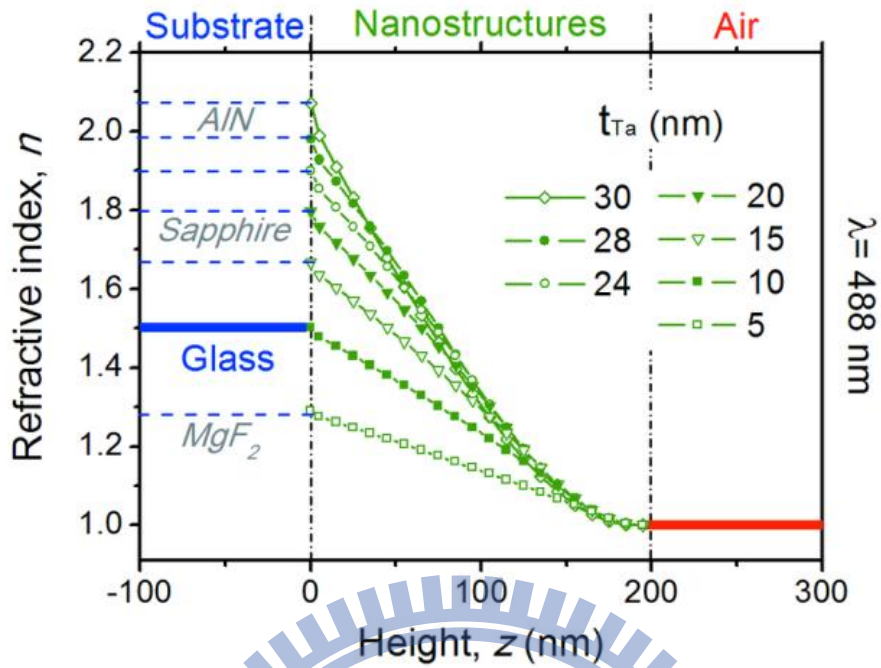


Figure 2.17 Refractive index profiles—for samples of various t_{Ta} —through air, the nanostructure and the substrate (wavelength: 488 nm). The x -axis represents the distance from the interface of the nanostructure and the substrate.

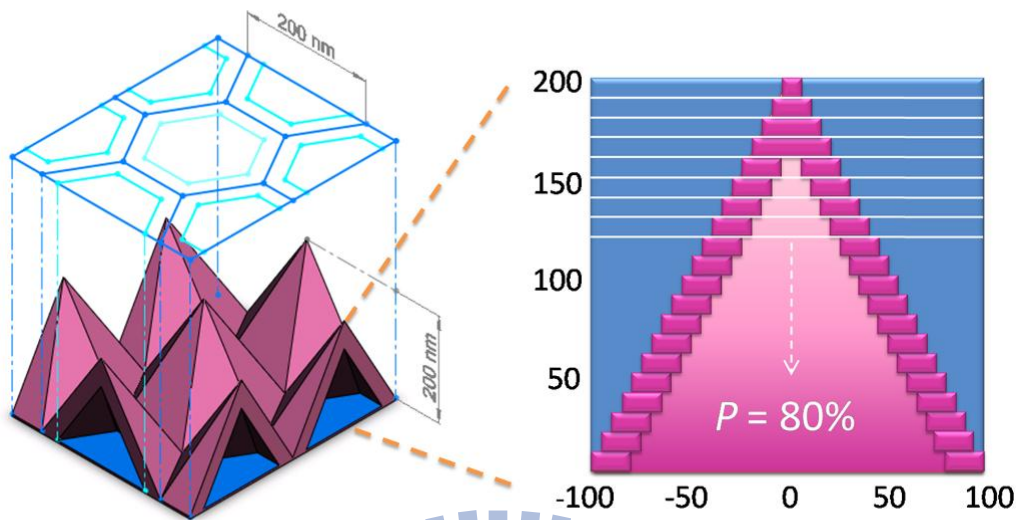
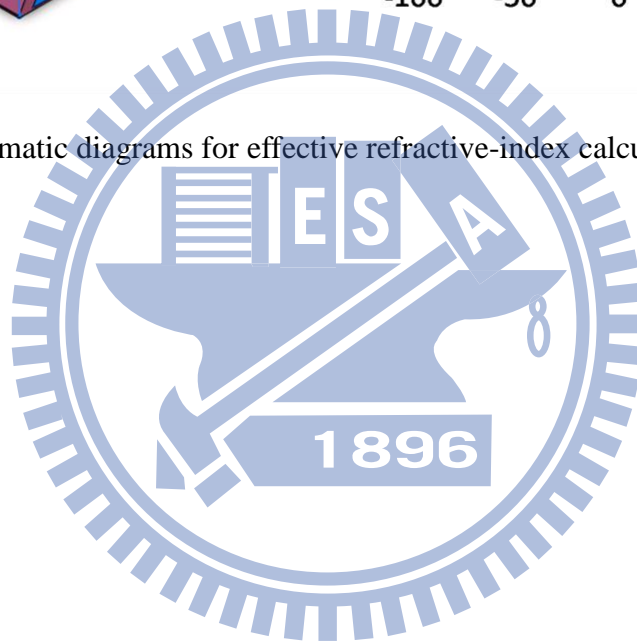


Figure 2.18 Schematic diagrams for effective refractive-index calculation.



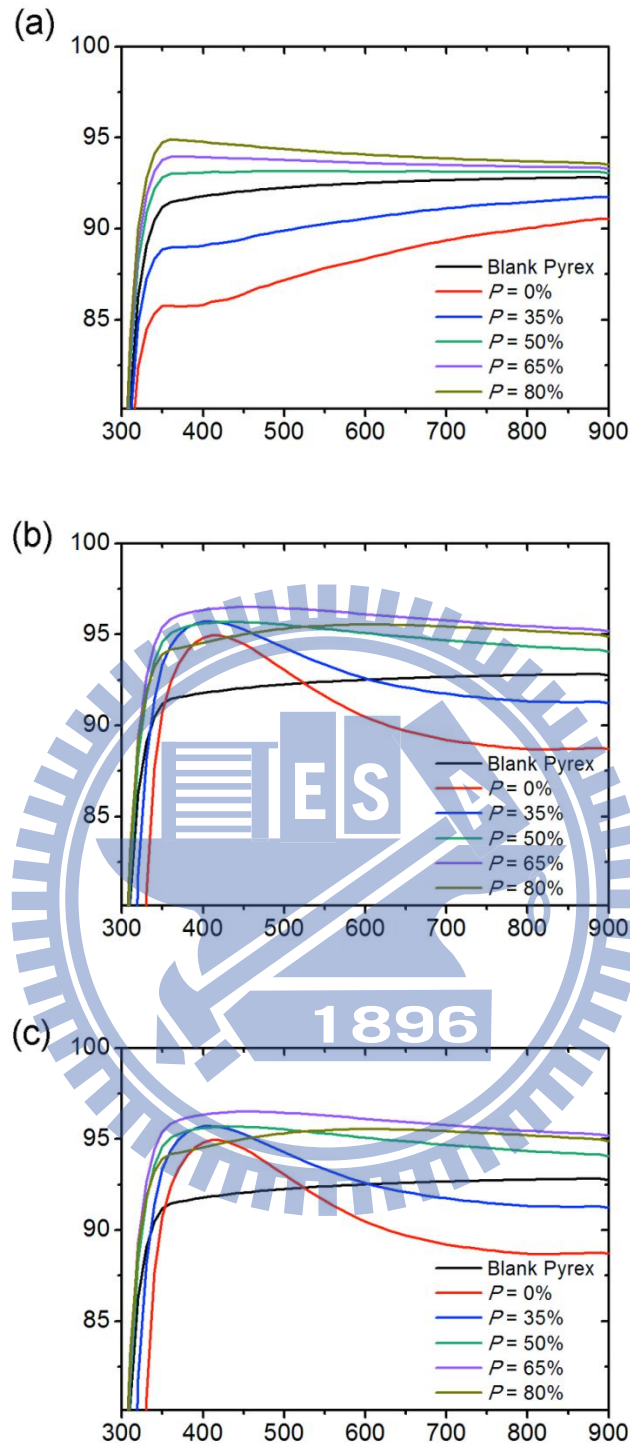


Figure 2.19 RCWA simulation of transmittance for single-sided coated Pyrex glass with various porosity and sizes NCAs. The nanocone structures was assumed to be a hexagonal close-packed period of (a) 100 nm, (b) 200 nm and (c) 300 nm with a height of (a)100 nm, (b) 200 nm and (c) 300 nm. A NCA owning a period and height of 200 nm and a porosity of 65% obtains the best transmittance.

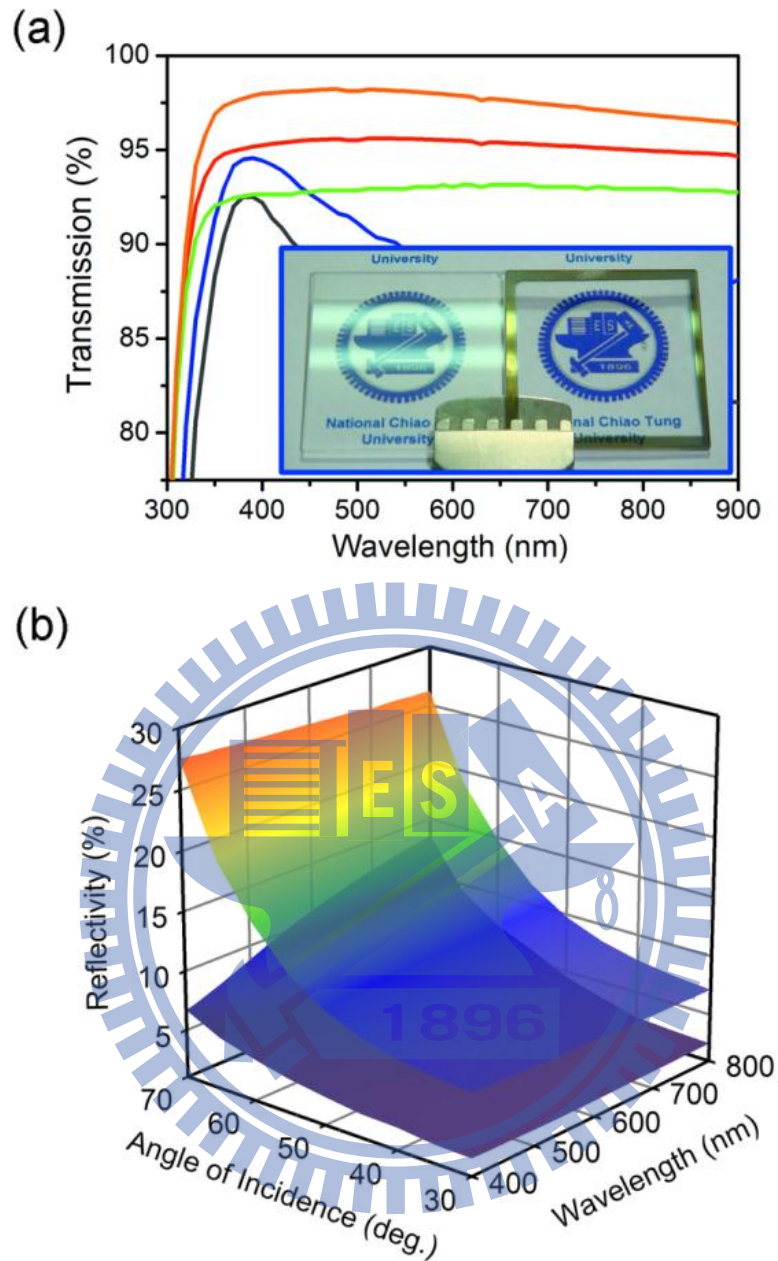


Figure 2.20 The optical performance of antireflective properties for NCA-coating glasses. (a) Measured transmissions of bare glass (green line) and NCA-coated (single side) glass substrates of initial Ta thicknesses of 10 nm (red line), 20 nm (blue line), 30 nm (black line) and 10 nm for double sides (orange line). Inset: Photographs of the structured (right) and unstructured (left) glass samples (30 mm × 30 mm) demonstrate the antireflective effect at a large tilted angle. (b) Measured wavelength and angle resolved absolute reflectance. The glass substrates were coated without (upper curve) and with double-sided NCA coating (lower curve).

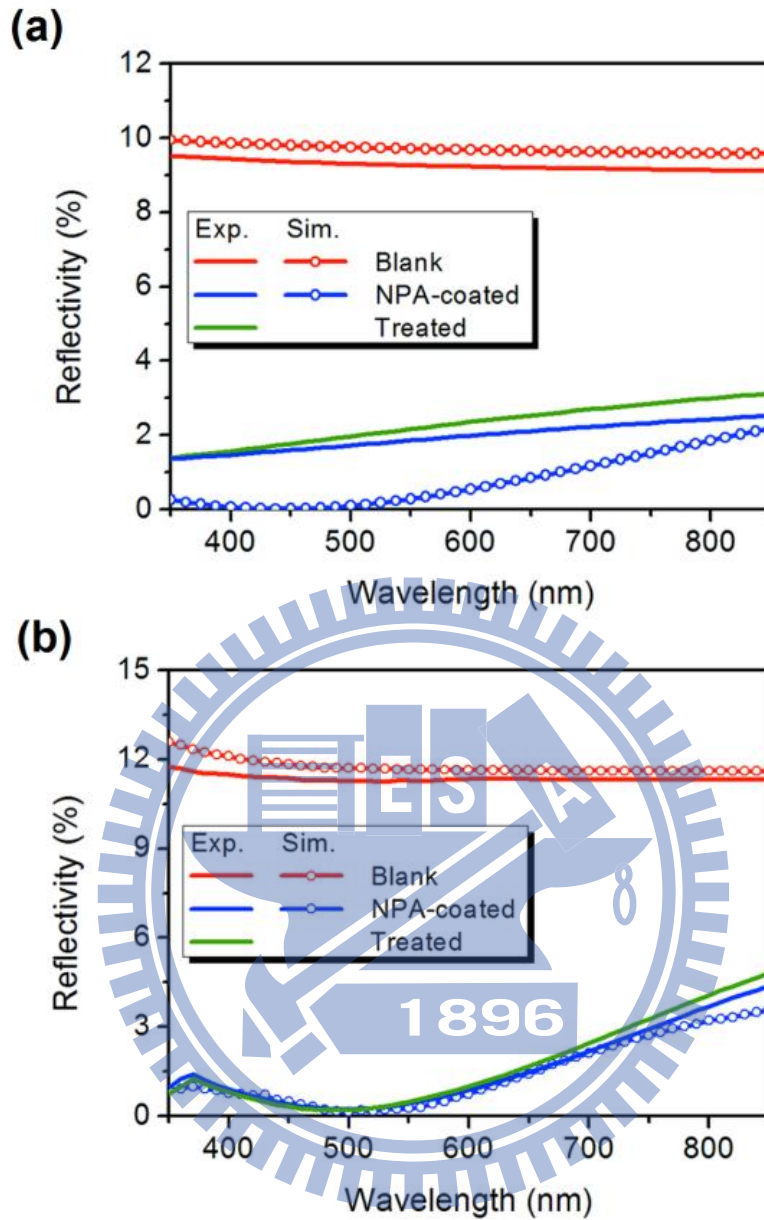


Figure 2.21 The improvement of reflectivity before and after the treatment for NCA coated on (a) sapphire and (b) AlN substrates. Experimental (solid) and RCWA-simulated (dotted) specular reflectivities at normal incidence were compared for a blank substrate (red lines), NCA coating (blue line) and NCA coating with treatment (green line).

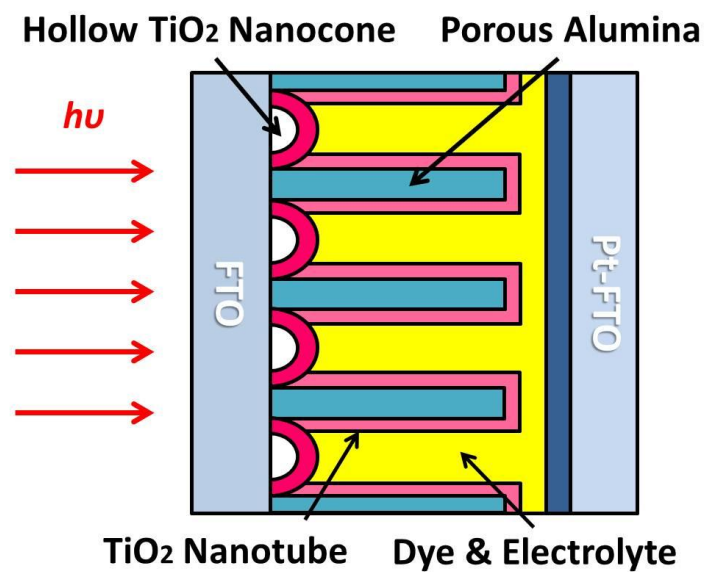
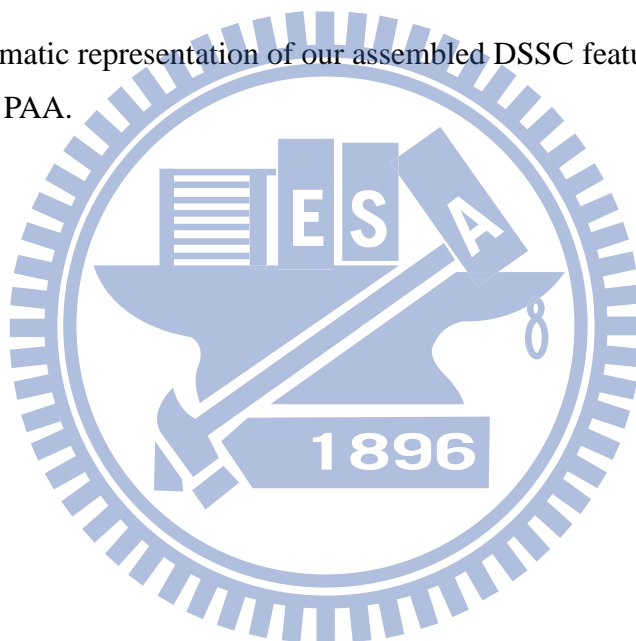


Figure 2.22 Schematic representation of our assembled DSSC featuring TiO₂ NTs and nanocones within PAA.



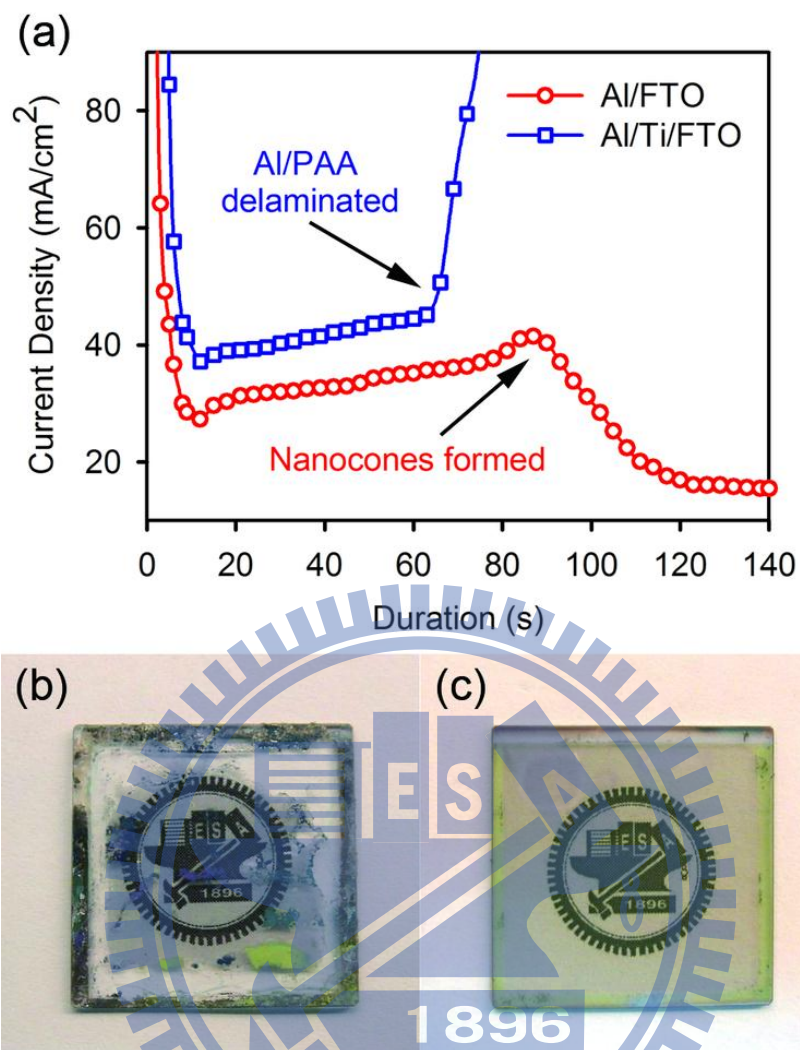


Figure 2.23 Typical anodization results of Al/FTO and Al/Ti/FTO samples. (a) Chronoamperical curve recorded during the anodization process. (b, c) Photographs of systems prepared in the (b) absence and (c) presence of Ti as the adhesion layer between the Al layer and the FTO substrate.

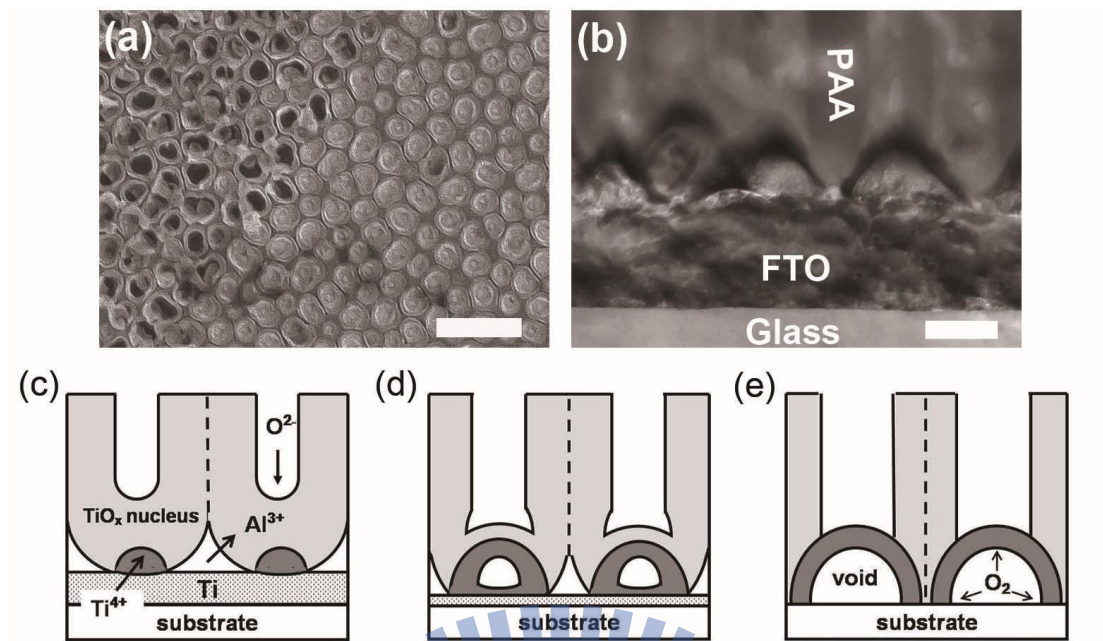


Figure 2.24 (a) Top-view SEM image (scale bar: 500 nm) of hollow TiO₂ nanocone arrays after alumina had been removed selectively. In the left part of the image, focused ion beam (FIB) milling had been used to reveal the hollow inner sections of the nanocones. (b) Cross-sectional TEM image of hollow TiO₂ nanocones (scale bar: 100 nm). (c–e) Schematic representation of the mechanism of formation of the hollow nanocones. (c) TiO₂ nucleus formed as the anodization approached the Ti–Al interface. (d) TiO₂ hillocks grew, leaving voids caused by O₂ pressure. (e) Cone-like hollow nanostructures formed with obstructing pore-walls.

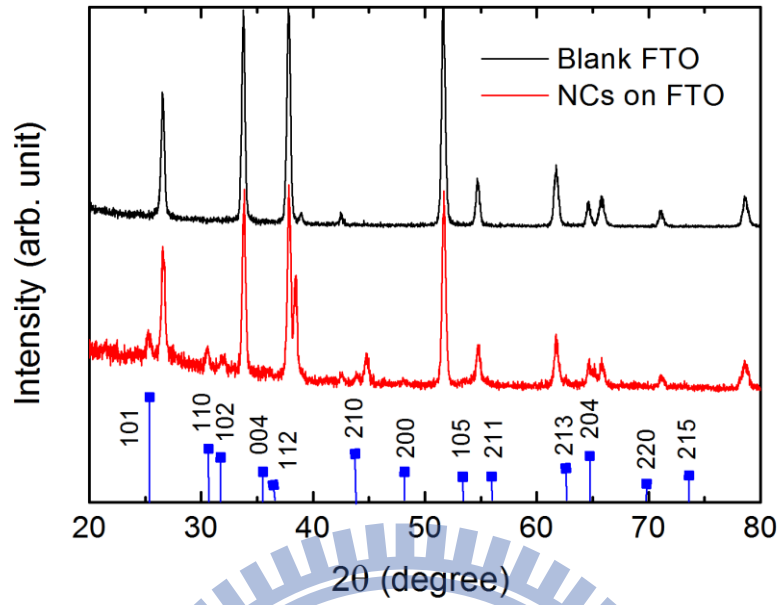
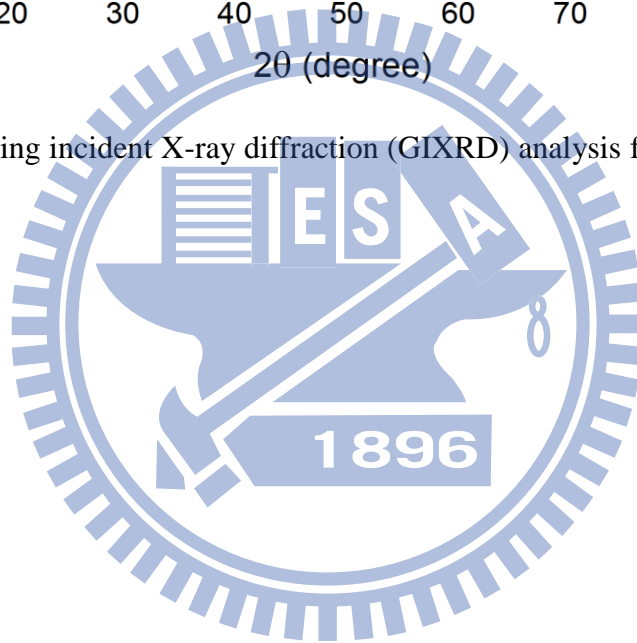


Figure 2.25 Grazing incident X-ray diffraction (GIXRD) analysis for TiO₂ nanocones on FTO.



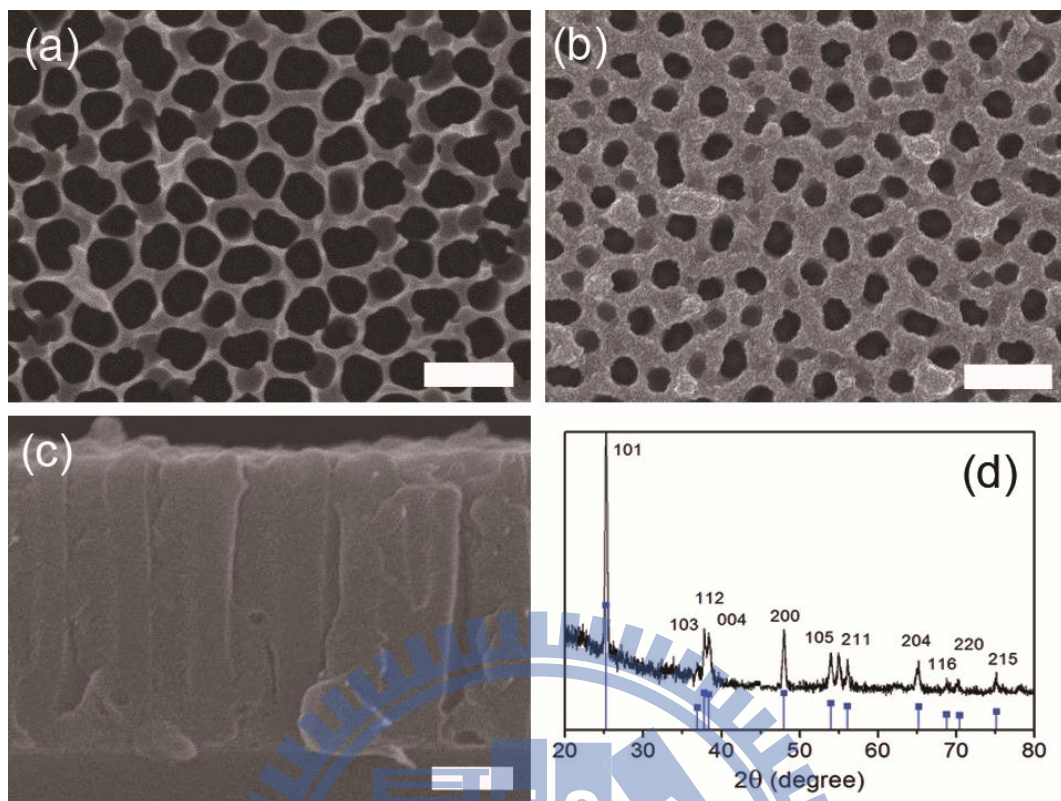


Figure 2.26 (a–c) Morphology of the TiO₂ NTs grown onto the pore walls of PAA. (a, b) Top-view SEM images (scale bar: 500 nm) of PAA (a) before and (b) after deposition of the TiO₂ NTs. (c) Cross-sectional SEM image (scale bar: 200 nm) of the sample in (b). (d) GIXRD analysis of a TiO₂ NT, revealing the desirable crystalline anatase phase.

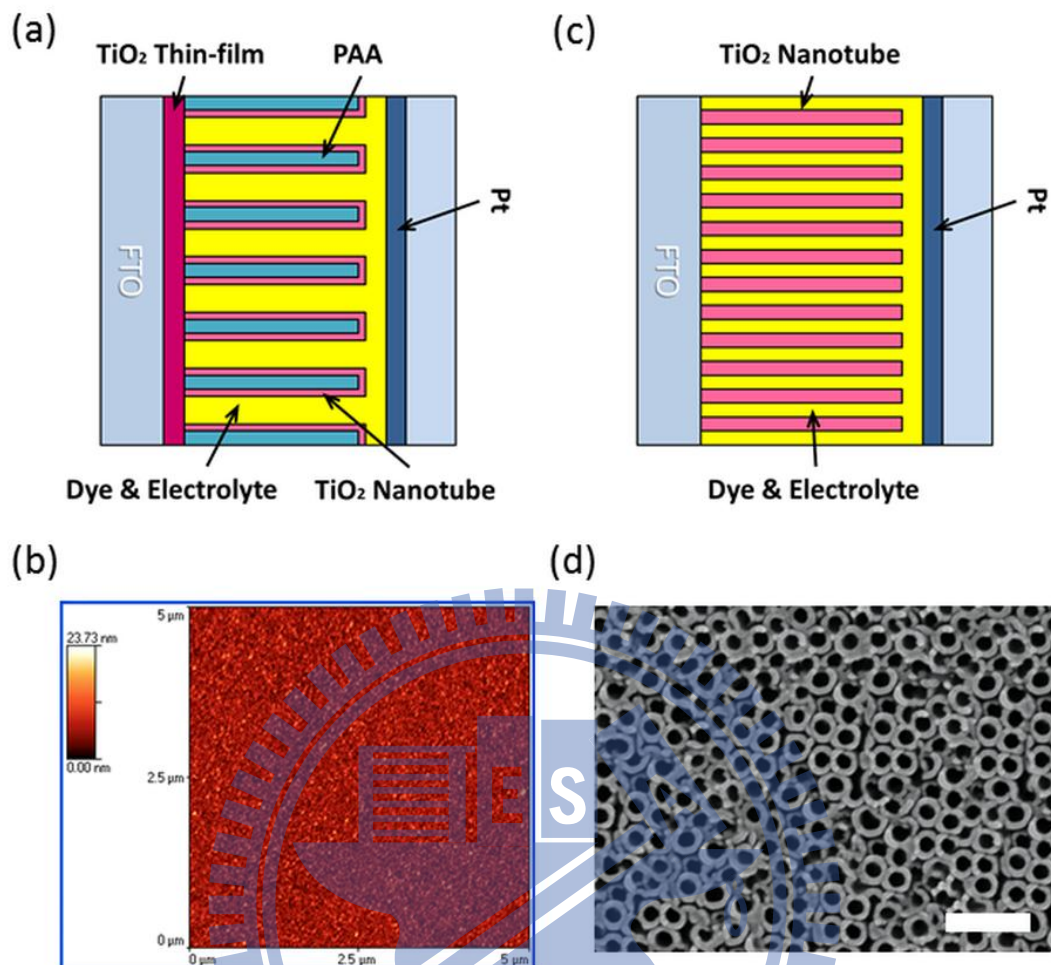


Figure 2.27 Schematic and microscopic images of samples NT-A-NC and NT-A. (a) Schematic representation of sample NT-A. (b) The AFM image of TiO₂ film onto FTO substrate. The arithmetic average roughness (R_a) and root mean square roughness (R_{RMS}) were 2.45 and 5.13 nm, respectively. The thickness of TiO₂ film is 100 nm from cross-sectional SEM observation. (c) Schematic representation of sample NT. (d) Top-view SEM image (scale bar: 500 nm) of anodic TiO₂ NTs of sample NT. The average inner diameter of the nanotube was 110 nm and outer diameter 160 nm. The depth of anodic TiO₂ NTs was estimated at about 700 nm from cross-sectional SEM observation. As we can see, cracks and interconnections appear in TiO₂ NTs.

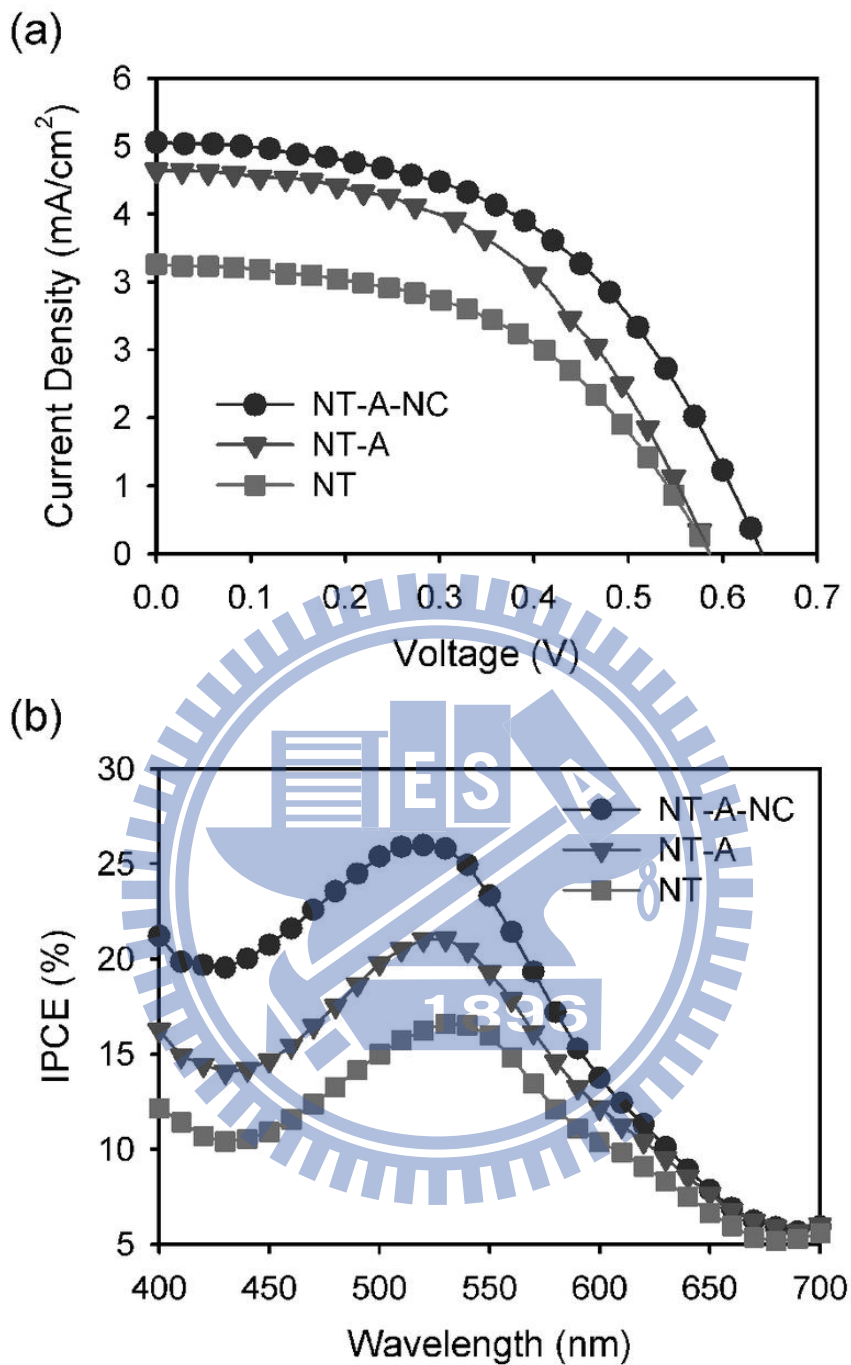


Figure 2.28 Photovoltage performances of cells constructed with various TiO₂ morphologies as electrodes: hollow TiO₂ nanocones under porous alumina and TiO₂ NTs (NT-A-NC); a TiO₂ film under porous alumina and TiO₂ NTs (NT-A); and anodic TiO₂ NTs without alumina (NT). (a) Current–voltage characteristics of the three DSSC devices. (b) The incident photon–to–current conversion efficiency (IPCE) spectra of the three DSSC devices.

Sample	J_{sc} (mA/cm ²)	V_{oc} (V)	FF (%)	η (%)
NT-A-NC	5.15	0.64	59	1.71
NT-A	4.78	0.59	46	1.45
NT	3.62	0.60	47	1.22

Table 2.1 DSSC performance metrics.



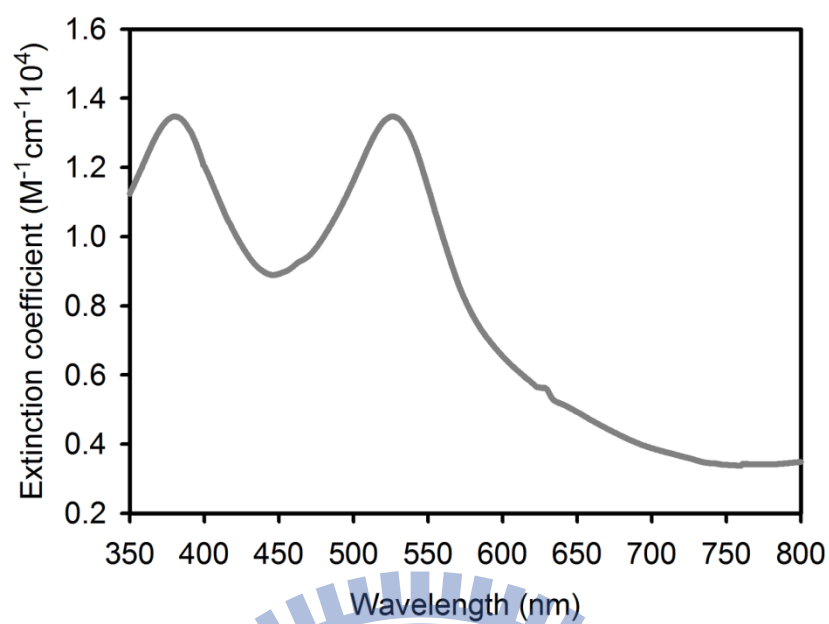


Figure 2.29 Absorption spectra of N719 sensitizer in absolute ethanol solution. The molar extinction coefficients of MLCT absorption band for N719 dye is $1.36 \times 10^4 M^{-1} cm^{-1}$, which is as well as that of ILCT absorption band ($1.36 \times 10^4 M^{-1} cm^{-1}$).

Chapter 3: An Anisotropic, Highly Stable and Water–Cleanable Gecko Adhesion via Innovative Design of Taper Nanohairs

3.1 Introduction

Nature has gone through evolution over the 3.8 G year since life is estimated to have appeared on the Earth.¹ Nature has evolved objects with high performance using commonly found materials. These function on the macroscale to the nanoscale. The understanding of the functions provided by objects and processes found in nature can guide us to imitate and produce nanomaterials, nanodevices and processes. On nanoscale, many of the atoms are still located on the surface, or one layer removed from the surface, as opposed to the interior. Thus, different properties are observed on this scale due to the interface that is not observed in the bulk or individual atoms. Since the properties depend on the size of the structure, instead of the nature of the material, reliable and continual change can be achieved using a single material.² As to nanoscale structure, nature is the best teacher giving from God. Biologically inspired design or adaptation or derivation from nature is referred to as ‘biomimetics’. It means mimicking biology or nature and is defined as ‘the study of the formation, structure or function of biologically produced substances and materials and biological mechanisms and processes especially for the purpose of synthesizing similar products by artificial mechanisms which mimic natural ones’. Nature uses commonly found materials, and properties of the materials and surfaces result from a complex interplay between the surface structure and the morphology and physical and chemical

properties. Many materials, surfaces and devices provide multifunctionality. Molecular-scale devices, superhydrophobicity, self-cleaning, drag reduction in fluid flow, energy conversion and conservation, high adhesion, reversible adhesion, aerodynamic lift, materials and fibers with high mechanical strength, biological self-assembly, antireflection, structural coloration, thermal insulation, self-healing and sensoryaid mechanisms are some of the examples found in nature that are of commercial interest.

A gecko is the largest animal that can produce high (dry) adhesion to support its weight with a high factor of safety. The secret of the gecko's adhesive properties lies in the microstructure and nanostructure of gecko feet.³⁻⁴ Microscopy shows that gecko feet are covered with millions of small hairs called setae, which further divide into hundreds of smaller spatulas.⁵ When such a structure is placed against any surface, hairs adapt and allow a very large area of contact with the surface. The van der Waals interaction between approximately millions setae and the substrate after contact is sufficient for the gecko to adhere and allow them to climb vertical surfaces at speeds of over 1 m, with the capability to attach or detach their toes in milliseconds. It has been suggested that this same hairy carpet on the gecko feet also plays an important role in self-cleaning.⁶

Gecko foot-hair, moth eyes and lotus surface mimicking structure were reported in "Nature" and "Science" in the past several times which we will have review next chapter. that shows a way to manufacture a prototype such as gecko-tape made by microfabrication of dense arrays of flexible plastic pillars with self-cleaning, re-attachable, the geometry of which is optimized to ensure their collective adhesion which proves that the re-attachable dry adhesives based on the gecko principle can find a variety of applications.

The emerging field of biomimetics is already gaining a foothold in the scientific

and technical arena. It is clear that nature has evolved and optimized a large number of materials and structured surfaces with rather unique characteristics. As we understand the underlying mechanisms, we can begin to exploit them for commercial applications.

3.1.1 Gecko-Inspired Artificial Structure for Adhesion

Van der Waals forces are unspecific and therefore omnipresent between practically any solid surfaces; the reason why we do not experience them in everyday life is their extremely short range: the surfaces have to be in intimate contact over large areas to exert strong forces. Nature utilizes these forces in animal locomotion. The prime example, which has aroused scientific interest especially over the last decade, is the adhesion and friction of the gecko pad for example during running, climbing, and traversing ceilings. It is now known that the gecko owes its extreme reversible adherence to a fine structure of hierarchically arranged fibrils, which enable it to exploit van der Waals and capillary forces with great efficiency.⁷⁻¹⁰

Dry adhesion mechanism in gecko lizards has attracted much attention since it provides strong, yet reversible attachment against surfaces of varying roughness and orientation. Such unusual adhesion capability is attributed to arrays of millions of fine microscopic foot hairs (setae), splitting into hundreds of smaller, nanoscale ends (spatulae), which form intimate contact to various surfaces by van der Waals forces with strong adhesion (10 N/cm^2).^{7,9} Recent advances of nanofabrication via top-down and bottom-up approaches have made it possible to develop synthetic, high-performance dry adhesives based on a range of different materials. Of these, polymeric nanohairs and carbon nanotubes (CNTs) have been largely used as attachment tip materials, since they allow for robust, high aspect ratio structures in a simple and reproducible manner.¹¹⁻¹⁶ In fact, researchers have already demonstrated that artificial dry adhesives can be applied to climbing robot and biomedical

patch.¹⁷⁻¹⁸

For fabricating gecko-inspired artificial dry adhesives, a number of methods have been proposed, which can be classified into two main streams: polymer-based dry adhesives and carbon nanotube (CNT)-based dry adhesives. These two kinds of adhesives have been developed independently by utilizing different fabrication principles. In general, the polymer-based adhesives have been fabricated by a top-down approach. For example, conventional topdown nanofabrication techniques such as electron-beam lithography, photolithography and etching techniques were utilized for fabricating nanohairs directly from a substrate.¹¹ In parallel, polymer molding techniques were adopted by using a master with straight nanoholes.^{12,14,19-20} As to CNT-based dry adhesives, a bottom-up approach in which the CNT arrays were grown from the catalyst layer deposited on a substrate by chemical vapor deposition. Due to different process characteristics and materials properties used in the fabrication, the polymer-based and the CNT-based dry adhesives demonstrate different adhesion capability and parameters.

One of the biggest advantages of the polymer-based methods is that they offer a simple and scalable approach to fabricating gecko-mimicking nanohairs with tailored geometry (angle, radius, height, shape of tip and hierarchy) and tunable material properties (modulus, surface energy, etc.) in a fast and cost-effective manner. Large area fabrication can be also achievable with the polymer-based approaches. The adhesion strength, however, is usually lower than that of the CNT-based adhesives because the resolution and aspect-ratio of polymer nanostructures are restricted by low mechanical strength of polymer materials. In contrast, the CNT-based dry adhesives usually have high level adhesion strength since the CNTs have superior structural features such as high AR, extremely small radius (10 nm) and high modulus (1000 GPa).¹⁵⁻¹⁶ Despite these advantages, the CNT-based methods are potentially

limited by complicated process for CNT growth and small patterning area (4 mm × 4 mm).^{15,21} Several exemplary works are in order to demonstrate how nanofabrication methods have been utilized to achieve synthetic dry adhesive with these two materials.

The gecko's high aspect-ratio nanohairy structures can maximize the contact area by a large number of pillars at the time of contact and a smaller effective modulus, which in turn increases the adhesion force against various surfaces. To achieve high aspect-ratio structures, Geim et al. presented a prototype of gecko tape having polyimide nanohairs (as small as 200 nm diameter) fabricated by e-beam lithography.¹¹ By fabricating high aspect-ratio polyimide hairs, relatively high normal adhesion (3 N/cm²) was obtained. The slow and expensive process of e-beam lithography, however, is a major shortcoming of this approach. In this work, they reported that the flexibility of the substrates was a crucial factor for obtaining high pull-off force. In these studies, researchers demonstrated that a small thickness of the substrate enhances the actual adhesion significantly as it allows flexibility and equal load sharing and prevents edge stress concentration.²² After the work by Geim et al., alternative approaches have been developed to overcome the limitations of e-beam lithography. The proposed approaches are mostly based on nanomolding methods, as they allow for a facile process with minimal time and cost. In these methods, various substrates (e.g., Si, SiO₂, poly-Si, PAA, polycarbonate film, etc.) having nanoholes are prepared by e-beam lithography, photolithography, etching or electrochemical reactions. Subsequently, nanohairs are replicated by molding polymers against the substrates. The fabricated substrates can be re-used as a template for nanomolding, allowing for significant reduction of time and cost. For example, Majidi et al. reported polypropylene nanohairs.¹³ The hairy structures were fabricated by casting polypropylene film into a commercially available polycarbonate filter at an elevated

temperature (at 200°C for 25 min) in a vacuum condition. In spite of high elastic modulus (1 GPa) of the polypropylene, the hair arrays exhibited the coefficient of friction greater than 5 N/cm² due to the enhanced compliance of the high aspect-ratio nanostructures. PAA also has been utilized as a mold for generating high aspect-ratio polymer nanohairs. The PAA template has highly ordered nanoholes whose diameters and depths can be easily controlled by varying the electrochemical parameters without the need of expensive e-beam or photolithography. Cho et al. presented a gecko mimicking adhesives by molding from PAA but with a low adhesion (0.05 N/cm²). High aspect-ratio polymer nanostructures could be easily obtained by simply molding the templates with thermoplastic or UV cured polymers.¹⁹⁻²⁰ However, the resulting nanohairs molded from the PAA usually suffer from self-matting problem due to wet chemical etching during template release or too high packing density and aspect-ratio of the nanostructures, which diminishes the resulting adhesion force significantly.¹⁹⁻²⁰ Jeong et al. suggested a nanodrawing method for fabricating high aspect-ratio polymer nanohairs (80 nm in diameter, 2 μm in height and aspect-ratio > 20) on a solid substrate by sequential application of molding and drawing of a thin polymer film with 3 N/cm².¹²

Fibrillar surfaces with a slanted angle show smaller effective elastic modulus than planar surfaces. As a result, they deform easily and form contact effectively, especially when adhering to rough substrates. The elastic-strain energy stored in slanted single fibrils during pull-off is dissipated and, as a consequence, the separation work is higher than for a planar contact of similar material.²³⁻²⁴ From the point of view of fracture mechanics, fibrillar structures with a slanted angle require frequent re-initiation of the interface crack and the failure of the interface therefore occurs at higher stresses.²⁴ Spatular tips at angles between 0 and 90° with respect to the substrate were obtained on tilted PU fibers by applying a controlled load to the tilted

fibrils during curing, causing bending of the fibrils.²⁵ This design, containing two independent tilted components (fiber and spatula), represents the most complex structure obtained to date with artificial systems. Slanted fibrillar structures were obtained by double replication of tilted SU-8 fibrillar arrays obtained by photolithography. This process involved tilted exposure of the resist layer to obtain fibrils forming angles between 0 and 500 with the substrate and exhibiting dimensions of 4 to 35 μm in diameter and ARs of up to 10. A mold of silicone rubber containing angled holes is then fabricated by soft-molding against the SU-8 template and subsequently used to obtain PU microfibers from liquid precursors.²⁶ Alternatively, arrays of PP microfibers were fabricated by first filling PC membranes with PP to obtain vertical fibrils and then tilting them by processing the patterned film through two heated rollers.²⁷ Tilted fibrils with 0.6 mm diameter, 18 to 20 mm length, and a 45° tilting angle were obtained. Coarser structures with 1mm length, 380 μm diameters and a tilt angle of 20° with a top face inclined at 450 with respect to the vertical were obtained by casting a PU precursor onto a mold fabricated by micromachining. Tilted structures were also prepared by a post-molding electron-beam irradiation step. The irradiated fibril surfaces shrink more than the opposite surface, resulting in bending of soft-molded fibrils.¹⁴ In this method, PUA nanopillars (100 nm in diameter and with an aspect-ratio of 10) were fabricated with tilting angles between 30° and 80°.

Ge et al. suggested dry adhesives with micropatterned CNT arrays.¹⁵ Interestingly, they reported that micropatterned CNT arrays with optimized geometry have four to seven times higher shear adhesion ($\sim 36 \text{ N/cm}^2$) strength than nonpatterned CNT arrays. Moreover, the adhesion strength was maintained over thousands of cycles. Qu et al. also reported similar adhesion strength (15 N/cm^2 for shear adhesion and 30 N/cm^2 for normal adhesions) by growing single walled CNTs

(SWCNTs).²⁸ Following this work, they further enhanced the performance of the dry adhesive using MWCNTs.¹⁶ With use of vertically aligned MWCNT having curly entangled end segment, they could obtain extremely high shear adhesion (~ 100 N/cm²), which was ten times higher than gecko's adhesion strength. The strong shear adhesion comes from shear-induced alignment of the nonaligned top layer of the nanotubes enhancing the contact line length.¹⁶ As a result, increasing the CNT length greatly enhanced the shear adhesion. In contrast, the normal adhesion force was almost insensitive to the nanotube length as a result of point contact. Interestingly, there have been seemingly opposite reports on repeatability and robustness of CNT-based dry adhesives. Ge et al. and Qu et al. reported that CNT arrays maintained the strength for long attachment/detachment cycles whereas Zhao et al. reported that the adhesion strength was decreased with repeated use due to an interface failure between CNT arrays and the substrate.¹⁵⁻¹⁶ Recently, Wirth et al. investigated the structural changes of vertically aligned CNT arrays (10 nm in diameter and 100 μ m in length) after attachment.²⁹ They observed that the applied force for preloading leads to the collapse of the CNT arrays limiting the repeatable use of the dry adhesives. It seems that the interfacial strength between CNTs and the substrate is important for ensuring robustness and repeatability of the CNT-based adhesives. In general, CNT-based dry adhesives have higher adhesion strength than polymer-based adhesives due to outstanding structural properties such as extremely high aspect-ratio ($> 10^4$, diameters around 10nm and heights over 100 μ m). With extraordinary high AR, the effective modulus of CNT is reduced below Dahlquist criterion ($E \sim 100$ kPa) in spite of its high mechanical modulus ($\sim 10^3$ GPa). However, the patterned area of CNT arrays is usually small (~ 1.6 mm²) due to the complicated process (photolithography, catalyst deposition and chemical vapor deposition at high temperature, e.g., $\sim 750^\circ\text{C}$). It is worthwhile noting in this regard that the adhesion

force per area can be enhanced greatly by reducing the contact area.³⁰ Also, the adhesion force of single nanohair measured by AFM might be misleading as it would not scale linearly into the bulk adhesion strength. In addition to the complicated and expensive process as well as small patterning area, another major concern of the CNT-based adhesives is that it requires a high preload (50~500 N/cm²) compared to that of polymer-based adhesives (< 0.5 N/cm²), potentially limiting the widespread use of the CNT-based adhesives.

Learning from nature creatures, we can find that nanostructures are essential in fabricating super hydrophobic surfaces with high CA, and multiscale structure can effectively reduce the angle of hysteresis of water droplets. In general, surfaces with a static CA (contact angle) higher than 150° are defined as super hydrophobic surfaces. As for the details of CA hysteresis,³¹⁻³³ five states are possible for super hydrophobic surfaces: Wenzel's state, Cassie's state, the so-called "Lotus" state, the transitional state between Wenzel's and Cassie's states, and the "Gecko" state.

The phenomenon of self-cleaning in gecko setae is out of general thinking because setae are adhesive and can self-clean when dry. Adhesion in gecko setae is a consequence of many divided contact points (spatulae) that deform to achieve intimate, high-density contact with the surface, whereas lotus-like surfaces remain slippery because their rough, and in some cases waxy, cuticle prevents intimate contact. Lotus-like surfaces require water as a cleaning agent,³⁴⁻³⁵ whereas self-cleaning in gecko setae may occur because it is energetically favorable for particles to be deposited on the surface rather than remain adhered to the spatula. We can model spatulae as curved surfaces with approximately spherical geometry at the interface, and also work at flexible strips. In each case, we compare the magnitude of attraction between a spherical dirt particle and a planar wall to the combined attraction of the same particle to a number of spatulae. This model suggests that >

26 spatulae would need to be attached simultaneously to a single 2.5 μm-radius dirt particle in order for self-cleaning not to occur, assuming similar Hamaker constants (A) and gap distances. Hamaker constants are unlikely to vary by more than a factor of 2; if we take the worst case where $A_{ps} \sim 2A_{pw}$, (where p and w refer to particle and wall, respectively) energetic equivalence occurs with 13 spatulae attached. Gap distance remains an unknown parameter in the model. Until measurements are available, we will assume that D_{pw} and D_{ps} have similar probability distributions, and thus can be assumed to be approximately equal.

Adhesion is the result of attractive forces between two solids with surfaces in close proximity. The opponent of adhesion is the elastic strain energy of the solids as they deform to optimize their contact. A well-known model that treats this energy balance for two contacting spheres is the Johnson–Kendall–Roberts theory.³⁶ It predicts the force necessary for producing a contact area with radius a between two spherical solids of radius R as

$$F = \frac{4 E^* a^3}{3 R} - \sqrt{4\pi E^* \gamma a^3} \dots\dots\dots (1)$$

where E^* is the Young modulus of the contact pair, and γ is the work of adhesion. The first term in Eq. 1 corresponds to the Hertz solution in the absence of attractive surface forces. The assumption of such forces leads to the prediction of a theoretical pull-off (or adhesion) force between a sphere and a plane given by

$$F_c = \frac{3}{2} \pi R \gamma \dots\dots\dots (2)$$

Application of the JKR model to living systems has led to the “contact splitting” principle:³⁷ If one spherical large contact is subdivided into n smaller contacts, with

identical apparent contact area, the adhesion force rises by a factor $n^{1/2}$. This principle is reflected in the design of the attachment pads of different natural species. Heavier animals with different lineage (including flies, beetles, spiders, and lizards) display progressively finer contact elements. Assuming that the adhesion force is proportional to body mass, a theoretical dependence of number of contacts versus animal mass has been derived which matches the observed correlation.³⁷ An additional feature in gecko locomotion is the rapid switching between attached and detached states. Understanding this mechanism is essential for producing responsive adhesives. Recent studies have revealed that geckos move by utilizing both adhesion in the normal direction and friction in the lateral direction.³⁸⁻³⁹ These two components are strongly coupled: the friction enhances the adhesion when geckos grip onto substrate surfaces, called “frictional adhesion”, while both forces fall to almost zero during detachment with little expenditure of energy by the gecko (“directional adhesion”). This mechanism arises if the fibrils are not vertical, but tilted with respect to the surface. It is because an angled structure significantly lowers the effective modulus of the surface.⁴⁰ According to a previous study, the effective modulus should be less than 100 kPa for ensuring a tacky surface (so called “Dahlquist criterion”), which is given by

$$E_{eff} = \frac{3EID \sin \theta}{L^2 \cos^2 \theta [1 \pm \mu \tan \theta]} \dots\dots\dots (3)$$

where E is the elastic modulus, I is the moment of inertia ($\pi R^4/4$, R is the radius of hair), D is the hair density, L is the hair length, μ is the friction coefficient, and θ is the slanted angle. For vertical nanostructures, it is extremely difficult to meet the Dahlquist criterion unless the aspect-ratio of the structure is extremely high. For example, the

AR should be larger than 2×10^2 for the vertical nanohairs with 100nm diameter assuming the slanted angle of 89° ($E = 1 \text{ GPa}$, $D = 1.1 \times 10^{-7} \text{ m}$, $\mu = 0.25$).³⁷

This value is not easily achievable using polymeric materials with current fabrication techniques. Even if possible, the self-matting problem or structural buckling will occur due to too high aspect-ratio and limited modulus of polymers.⁴⁰⁻⁴¹ On contrast, if the structures are slanted, the effective modulus can be greatly reduced without the need of structures with extremely high AR. For 100 nm nanohairs with aspect-ratio of 20 ($E = 1 \text{ GPa}$, $D = 1.1 \times 10^{-7} \text{ m}$, $\mu = 0.25$), the effective modulus decreases less than 100 kPa when the structures are slanted with less than 60° angle with respect to the horizontal plane. Most solid surfaces are not perfectly smooth and have some degree of roughness. Therefore, the height of nanohair should be long enough to ensure adaptation of rough surface with varying amplitude and topography. The maximum height of polymer nanohair (h_{\max}), however, is restricted by a critical value that is involved in lateral collapse of hairy structures due to relatively low elastic modulus of polymers. The value of h_{\max} for given elastic modulus, size and surface energy of nanohairs is given by⁴⁰

$$h_{\max}(L) = \left(\frac{\pi^4 ER}{2^{11} \gamma_s (1-\nu^2)} \right)^{\frac{1}{12}} \times \left(\frac{12ER^3 (W/2)^2}{\gamma_s} \right)^{\frac{1}{4}} \dots\dots\dots (4)$$

where R is the radius of hair, γ_s is the surface energy, W is the distance of two neighboring hairs, E is the elastic modulus of hair, and ν is the Poisson's ratio. According to Eq. 4, the maximum aspect-ratio of polymeric nanohairs without self-matting is about 10~20, limiting the absolute height of nanostructures significantly. In this regard, micro/nanoscale combined hierarchical structures could be useful, as they increase adhesion strength against a rough surface either by enhancing structural height or by reducing structural stiffness without structural

instability observed in high aspect-ratio nanostructures.⁴² As to the adhesion, the adhesion energy, which consists of the energy dissipated along the interface and the elastic energy stored in the fibril volume, should be concerned without doubt.

$$\gamma_{eff} = \varphi \left(\gamma + \frac{P_{cr}^2}{2E(WH)^2} L \right) \dots\dots\dots (5)$$

where L is the length of the fibrils, P_{cr} is the critical force required to peel an elastic thin film off a rigid surface, W is the width of the film, H is the thickness of the film and φ is the area fraction of the fibril array. According to Eq. 5,⁴²⁻⁴³ the larger the length of the fibrils are, the higher will be the adhesion energy. Taking L = 120 μm as the length of a seta, we can find γ_e >> γ. For φ~1, when the peeling angle of the spatula pad is θ = π/2, we have γ_e = 10 J and γ = 0.1 J; when the peeling angle of the spatula pad is slightly smaller than θ = π/6, we find γ_e = 924 J and γ = 9.24 J. Therefore, extending the spatula pads to the length of the seta gives rise to a structural unit with much higher adhesion energy than the van der Waals interaction energy. The increase in adhesion energy is tremendous. At the same time, the effect of orientation dependent adhesion energy for peeling at different angles is magnified through the term P_{cr}² in Eq. 5. Thus, at the scale of the seta, the adhesion energy for attachment is almost two orders of magnitude higher than that for detachment.

3.1.2 Geometry-Controllable Templates from PAA

PAA formed by anodization has been widely studied in more than 100 years.⁴⁴⁻⁵⁰ Porous alumina membranes are used for the fabrication of composites in nanometer scale because of their relatively regular structure with narrow size distribution of pore diameters and interpore spacings.⁴⁴ The pore structure is a self-ordered hexagonal array of cells with cylindrical pores of variable sizes with diameter of 25 nm to 420 nm with depths exceeding 100 nm depending on the anodizing conditions used.⁵¹

Essentially, the structure is a result of several coupled phenomena. One mechanism is a nonuniform electric field and, hence, current that arises in the porous aluminum structure as a result of topological variations. The second mechanism is either field-enhanced dissolution or increased local temperature that enhances dissolution of the bottom oxide barrier layer.⁴⁴ These coupled phenomena preferentially remove the oxide at the bottom of the pores while leaving the pore walls intact. In another hand, “Nature” describes a model of PAA growth based on simple concepts of volume and charge conservation, coupled with experimentally validated descriptions of interfacial reactions and transport processes recently.⁵² The resulting structure is an ordered hexagonal array of cells with cylindrical pores with cell walls composed of alumina. Nanoporous anodic aluminium oxide with self-organized hexagonal arrays of uniform parallel nanopores has been used for various applications in the fields of sensing, storage, separation, and the synthesis of one-dimensional nanostructures.⁵³⁻⁵⁵ Self-ordered PAAs have been obtained by mild anodization (MA) and hard anodization (HA). Both of their advantages are utilized in our experiments.

In ordinary two-step mild anodization (MA) process, the self-ordered columns of alumina nanopores can be obtained within three well-known growth regimes:

(1) Sulphuric acid (H_2SO_4) at 25 V for D_{int} (interpore distance) = 63 nm^{51,56}

(2) Oxalic acid ($\text{H}_2\text{C}_2\text{O}_4$) at 40 V for $D_{\text{int}} = 100$ nm⁵⁷⁻⁵⁹

(3) Phosphoric acid (H_3PO_4) at 195 V for $D_{\text{int}} = 500$ nm⁵⁹⁻⁶⁰

Applied voltages higher than the optimum value required to maintain stable anodization in a given electrolyte always result in ‘breakdown’ or ‘burning’ of the oxide film caused by catastrophic flow of electric current.⁶¹ Therefore, a long anodizing time (16 h) was required to obtain highly ordered PAA films.⁵⁶ Masuda et al. reported self-organized pore growth, leading to a densely packed hexagonal pore structure for certain sets of parameters.⁵⁷ The self-organized arrangement of

neighboring pores in hexagonal arrays can be explained by any repulsive interaction between the pores.

In general, the fabrication of self-ordered AlO pore arrays, under conventional so-called 'mild anodization' (MA) conditions, requires several days of processing time and the self-ordering phenomenon occurs only in narrow process windows, known as 'self-ordering regimes'.^{51,56-60} Owing to the slow oxide growth rates (for example: 2–6 $\mu\text{m h}^{-1}$), MA processes based on Masuda's approach have not been used in industrial processes so far. Hence hard anodization (HA) of aluminum, a faster process that was invented in the early 1960s is an attractive alternative.⁶²⁻⁶³ HA is carried out at relatively low temperatures and high current densities, and has routinely been used in the aluminum industry to produce anodic films of high technical quality at an efficient rate of production (typically 50–100 $\mu\text{m h}^{-1}$).

Above all, from a practical point of view, the HA process has many advantages over conventional MA. The major findings on the HA process are as follows. (1) The current density (that is, the electric field strength E at the pore bottom) is an important parameter governing the self-organization of oxide nanopores in a given anodization potential. (2) A new self-ordering regime is established over a broad range of $D_{\text{int}} = 200\text{--}300$ nm in $\text{C}_2\text{H}_2\text{O}_4$ and $D_{\text{int}} = 320$ nm in $\text{H}_3\text{PO}_4\text{-H}_2\text{O-C}_2\text{H}_5\text{OH}$.⁶⁴ (3) The ratio ζ of the D_{int} to the anodization potential is lower ($\zeta_{\text{HA}} = 2.0$ nm V^{-1} for HA, and $\zeta_{\text{MA}} = 2.5$ nm V^{-1} for MA). (4) The porosity P is lower ($P_{\text{HA}} \sim 3\%$, $P_{\text{MA}} \sim 10\%$). (5) The growth rate of the porous oxide film is 30 times larger (>50 $\mu\text{m h}^{-1}$) than for MA. (6) Ideally ordered alumina membranes with a high aspect ratio ($>1,000$) of uniform nanopores can be fabricated by HA of pre-patterned aluminum. (7) Pulse anodizations of aluminum were conducted under potentiostatic conditions by using sulfuric acid or oxalic acid. Pulses consisting of a low-potential pulse followed by a high-potential pulse were applied to achieve alternating MA and HA conditions. A combination of

HA and MA allows modulation of the pore diameter over extremely high aspect ratios.⁶¹⁻⁶⁵

These results imply that pore initiation and the steady growth of alumina cells are strongly influenced by the high current density. In order to explain the mechanism behind pore formation phenomenon of self-organization in HA mechanism, the situation during steady state pore growth has to be considered. Pores grow perpendicular to the surface with the equilibrium of field-enhanced oxide dissolution at the oxide/electrolyte interface and oxide growth at the metal/oxide interface.⁶⁶

While the latter is due to the migration of oxygen containing ions (O^{2-}/OH^-) from the electrolyte through the oxide layer at the pore bottom, Al^{3+} ions which simultaneously drift through the oxide layer are ejected into the solution at the oxide/electrolyte interface. The fact that Al^{3+} ions are lost to the electrolyte has been shown to be a prerequisite for porous oxide growth, whereas Al^{3+} ions which reach the oxide/electrolyte interface contribute to oxide formation in the case of barrier oxide growth. A possible origin of forces between neighboring pores is therefore the mechanical stress which is associated with the expansion during oxide formation at the metal/oxide interface. During the initial stages of film growth, the penetration paths that develop (which are the precursors of the regular pores) are more densely distributed due to the high anodizing current densities. Since the oxidation takes place at the entire pore bottom simultaneously, the material can only expand in the vertical direction, so that the existing pore walls are pushed upwards. Thereafter, steady film growth is attained with the development of the major pores and the repulsive interaction between the alumina cells. The repulsive interaction force, associated with expansion during film formation at the aluminium/oxide interface, increases with electric field. The strong repulsive or expansion force (high field) under high current density limited the transverse growth of alumina cells and forced them to form

close-packed hexagonal arrays. Thus producing highly ordered PAA films is over a large area.⁶⁷

The anodic porous alumina, which is formed by Al anodization in acidic solution, is a typical self-ordered material. Under appropriate anodization conditions, long-range-ordered anodic porous alumina with an ideally pore size can be obtained. The shape of the holes in the anodic porous alumina can be controlled by a process composed of a series of anodization and subsequent etching treatments (H_3PO_4). By using the anodic porous alumina with shape-controlled holes as a mold for the replication, the preparation of high aspect-ratio structures of polymer could be achieved.⁶⁸

3.2 Materials and Methods

Chemicals and Materials. Phosphoric acid (H_3PO_4 , 86%), anhydrous ethanol (99.5%), and dihydrate oxalic acid ($\text{C}_2\text{H}_2\text{O}_4 \cdot 2\text{H}_2\text{O}$, 99.8%) were purchased from J. T. Baker (Phillipsburg, NJ, USA). Polyurethaneacrylate (soft PUA, 99%) was purchased from Sigma-Aldrich (St. Louis, MI, USA). Chromium trioxide (CrO_3 , 99%) and perchloric acid (HClO_4 , 70%) were purchased from Showa (Tokyo, Japan). Aluminium foil (99.999%) and 1H, 1H, 2H, 2H-perfluorooctyltrichlorosilane ($\text{C}_8\text{H}_4\text{Cl}_3\text{F}_{13}\text{Si}$, 97%) were purchased from Alfa Aesar. Ultrapure water used in all experiments was purified with a Milli-Q apparatus (Millipore, Billerica, MA, USA) to a resistivity of 18.2 $\text{M}\Omega \text{ cm}$. All chemicals were used without further purification.

Anodization Process. Aluminum foils were degreased in acetone, washed in de-ionized water, and put into a tailor-made holder with an opening of 3 cm^2 . Before anodizing, the aluminum was treated with annealing at 450°C for 12 hr and electropolished at a constant voltage in a 1:4 volume mixture of perchloric acid and ethanol under room temperature. The $\text{C}_2\text{H}_2\text{O}_4$ – $\text{C}_2\text{H}_5\text{OH}$ – H_2O electrolytes, and

$\text{H}_3\text{PO}_4\text{-C}_2\text{H}_5\text{OH-H}_2\text{O}$ electrolytes are designated. For the pre-step HA, the concentrations of phosphoric acid in the electrolytes were in the range of 0.25 M. The temperatures of the electrolytes were kept at -10°C by a powerful low-constant-temperature bath, and samples were anodized at target voltages 195 V for 10 min. After the selective removal of alumina in a mixture solution of CrO_3 and H_3PO_4 , the first HA was carried out under the same anodization conditions. During the first anodization step, the shape of the holes was precisely controlled by changing the times of anodization and etching in phosphoric acid at 53°C . For the second step HA, the concentrations of oxalic acid in the electrolytes were in the range of 0.1M, the temperatures of the electrolytes were kept at -10°C , samples were anodized at target voltages 195 V for 10 s, the PAA template with pore diameter of 380 nm and length of 1.3 μm was obtained. A Cu foil was used as the support for the working electrode. The substrate was positioned on top of the support while Cu tapes were used to connect the Cu support to the Al film upon the sample. The design advances the uniform current distribution from Cu support to underlying Al, leading to a homogeneous anodization. Two acrylic caps were used to fasten the sample and the Cu support inside within O-ring.

Fabrication of Hairy Nanostructures. The taper shaped gecko-like structure via self-ordered porous alumina hard templates serving as shape-defining molds is well-established. After preparing the tapered PAA master with a specific feature size, we fabricated tapered nanohairs by replicating the master with soft UV-curable polyurethane acrylate (PUA). The master was treated with a fluorinated SAM solution. The treated master mold was annealed at 120°C for 20 min. Drops of soft PUA prepolymers were dispensed onto the master mold and UV-transparent able silica was slightly pressed against the liquid drop as a supporting backplane. After preparing a polymer replica by UV exposure for 1hr through the transparent back side (dose = 15

mJ/cm²) and mold removal, the PUA replica was additionally exposed to UV for 10 h for complete curing.

3.3 Results and Discussions

3.3.1 Fabrication of Desirable Taper PAA Templates

HA (hard anodization), which is highly dependent on current density and temperature, is utilized to fabricate taper PAA in our work. Figure 3.1 presented the SEM images of taper PAA with 1.3 μm in length and 380 nm in diameter. HA and MA (mild anodization) are rather distinct in current density, film growth rate and interpore distance (D_{int}). From Figure 3.2, unlike the typical anodization curve of MA, the current density in HA shows a nearly exponential decrease as a function of time which have been reported in detail.⁶⁸ We compared a conventional MA anodization with our HA anodization and showed in Table 3.1. Larger current density caused by larger voltage (Figure 3.2) will lead to a high growth rate due to the extremely rapid movement of ionic species (O^2 , OH^- , Al^{3+}). Film growth rate is highly dependent on current densities, once a given value of current density can stand for a corresponded growth rate through our database. Moreover, low porosity in HA provided us a better specification for a sharper tip than that of MA. Figure 3.3 showed PAAs of different lengths via the same film growth rate, which is related to the current densities of HA, in different processing time. Furthermore, high anodizing current density will induce a denser penetration path distribution during the initial stages of film growth compared with MA. The repulsive interaction force between the alumina cells (from high current density) limited the transverse growth of alumina cells and force them to form close-packed hexagonal arrays, thus producing highly ordered PAA quicker than that in MA as shown in Figure 3.1c, d.

During the taper PAA fabricating process, we have found few special phenomena

such as concentration effect, diameter saturation and decoupling anodization of HA. We discussed the results of these three aspects respectively as follows. First, instead of affecting diameter or others, we noted that the concentration only affect the current density which is referred to the ordering and film growth rate. Current density was produced by the movement of ionic species which acquire more in higher concentration electrolyte. However, large current density may also cause the joule heat which will destroy the ordering and bring unstable situation. Once the cooling system cannot eliminate the tremendous heat instantly, the orientation will be disturbed. We discovered that the optimal concentration is 2.5% for producing and releasing heat from the sample. According to Figure 3.4a, 1% H_3PO_4 solution cannot afford enough ionic species, but 10% H_3PO_4 solution provided excessive ionic species and joule heat to obtain high ordering.

Further, the ordinary empirical relationship between voltages and diameters of PAA are $D_{int} = 2.5 Ea$ for MA and $D_{int} = 2 Ea$ for HA. The linearly relationship will vanish above a saturation value of voltage, and left the better ordering arrangement with an increasing current density induced from a large voltage (Figure 3.5). The strong repulsive force between the alumina cells induced by higher current density may be the main reason of the saturate diameter. That is, we can acquire a highly ordered PAA with increasing voltage as long as the joule heat induced can be released by the powerful cooling system.

We also perceived a decoupling system by using different electrolyte in HA. It can support us to modulate nanopore diameter with different porosity, hence resulted in the fine structure which facilitated the adhesion force of PUA as shown in Figure 3.1b and Figure 3.6. Conventional two-step anodization process should be done with the same electrolyte and voltage in both steps which will also cause the same porosity. With our two-step decoupling anodization, the pore size and interpore spacing of

ordered PAA can be independently controlled without using expensive and cumbersome imprinting. For instance, we could fabricate the second step in oxalic acid with same voltage as the first step (in phosphoric acid) and resulted in a smaller pore diameter about 30 nm, where the ratio of D_{int} to Ea is 2 for both phosphoric acid and oxalic in HA. Figure 3.6c and d presented the fabrication of PAA beyond the processing windows (with different voltage in each step), leading into a breakdown of ordering.

To sum up, using phosphoric acid as an electrolyte required a higher working voltage and current density to obtain ideal interpore distance, hence it will be perplexed to fabricate PAA compared with other acid. Without expensive imprinting process, we firstly manufacture highly ordered taper and decoupling structured PAA in phosphoric acid through HA process. Moreover, HA process provided a short anodizing time which avoided disorder structure due to the amassment of joule heat.

3.3.2 Design of Ideal Nanohairs for Gecko Adhesion

In this section, we presented nano-scaled, taper hairy adhesives which can perform high adhesion, high stability and also self-cleaning properties. Getting the vindication from nature animals, we suggest that it is integral for generating high adhesives, which can sustain grant weight such as human being, via nano-scaled structure instead of micro-structure due to an important consequence of contact splitting theory. Our design principle for the nano-scaled taper hairy adhesives is based on this finding. We'll discuss the results, length effect, and the reason of utilizing taper shape, slanted angle for easily releasing and self-cleaning feature as following. Table 3.2 presents the comparison of the gecko mimicking adhesives including our work.

Young's modulus is a fairly important parameter for us to forecast the adhesive ability and whether the hairy structures bunch themselves or not. Conventional

adhesives, such as those used in adhesive tapes, must be soft enough. It means that low Young's modulus materials ($E < 100$ kPa) were used for satisfying Dahlquist's criterion to inherit intimate and continuous surface contact.⁷⁰ Definitely, the Young's modulus will vary by the deformation and geometry to fit the criterion. Facile fabrication of high-AR and taper nanostructures by replica molding requires the optimization of mechanical properties of a structured material. If the material is too soft (such as polydimethylsiloxane so called PDMS, with a Young's modulus of 1.8 MPa), the resulting high-AR nanostructure is prone to clump and collapse after molding which will reduce the real area of contact between the adhesive and surface. In contrast, if the material is too stiff (such as carbon nanotube), the high-AR nanostructure can readily be fabricated, despite a high preloading force and a significant reduction in the adaptability for a rough surface are still the major concern. Hence, the material we using is sufficiently rigid for high-AR replica molding with its modulus 19.8 MPa but low preloading force. In short summary, in theory, smaller features will generate higher levels of adhesion, and such materials with a higher modulus of elasticity will resist clumping and fouling.

The taper shape is beneficial for its "longer length", "higher stability", "higher adhesion" and better "self-cleaning" ability compared with other shapes, showing the profile and SEM image of taper pillars in Figure 3.7. Pillars cannot survive at the same conditions of density and length compared with taper shape pillar, that is, the life time or cycles can be improved without additional deposition such as Pt compared with other shapes of nanohairs as shown in Figure 3.8. Eq. 6⁷¹ and Eq. 7⁷²⁻⁷³ explain the maximum height of polymer nanohair (H) and the adhesion energy of the fibrils, respectively.

$$h_{\max}(L) = \left(\frac{\pi^4 ER}{2^{11} \gamma_s (1 - \nu^2)} \right)^{\frac{1}{12}} \times \left(\frac{12ER^3 (W/2)^2}{\gamma_s} \right)^{\frac{1}{4}} \dots \dots \dots (6)$$

where R is the radius of hair, r_s is the surface energy, W is the distance of neighboring hairs, E is the elastic modulus of hair, and ν is the Poisson's ratio.

$$\gamma_{\text{eff}} = \varphi \left(\gamma + \frac{P_{\text{cr}}^2}{2E(WH)^2} L \right) \dots \dots \dots (7)$$

where L is the length of the fibrils, P_{cr} is the critical force required to peel an elastic thin film off a rigid surface, W is the width of the film, H is the thickness of the film and φ is the area fraction of the fibril array.

According to Eq. 7, the larger the density (area fraction) or length of the fibrils, which means the high aspect-ratio fibrils accompany the high adhesion energy. Taper shape has the advantages compared with pillar shape in both of density and length. The advantage is showing here via this equation, the taper shaped pillar can keep high density of fibrils which referred to adhesion ability while length increasing. Because if the pillar shape reach the same optimal length level as taper shaped pillar, the space between only pillar shapes should be widen in case of bunching, that is, density and area fraction must be decreased dramatically which reduce the adhesion force. Consequently, taper pillar has a better performance than others. Gradient diameter of taper shaped pillar can firmly support whole weight from bottom, and avoids bunching due to wider interval from top. Evidently, taper shaped pillar can did increase the pillar height compared to pillar shape in the same material as shown in Figure 3.7d. It is also noted that the maximum height of taper shaped and pillar shaped nanohairs in Eq. 6 are in the range of 1.3~1.8 μm and 0.7~1.2 μm respectively ($\gamma_s \sim 40 \text{ mJ/m}^2$ and $\nu = 0.5$), corresponding to the height of taper shaped hairs

presented here (~1.4 μm and 800 nm). As shown in Figure 3.9-10, different lengths and profiles are fabricated by replicating, and the optimal lengths are 1.4 μm and 800 nm, respectively, which are both fit to the theoretic value. Obviously, the pillars adhered with themselves in Figure 3.10a-c while no taper nanohairs attach themselves regardless of long or short structures.

Gecko’s adhesive system is massively reusable and stable because of its multilevel hierarchy that distributes the load and generates such high levels of adhesion because of the smaller features (Figure 3.11a).⁷⁰ We can easily understand that taper shape could achieve stable and reusable than others due to the gradient diameter from bottom to top of the pillar. The larger diameter at bottom can support longer length and offer a better fundamental base of the pillar in case of breaking by external force, and smaller diameter at top is responsible for higher contact area related to the adhesion and also avoids clumping which we discussed previously (Figure 3.7d). We can split the taper shape into several layers stacked up one by one as shown in Figure 3.11b. Moreover, each layer can regard as a sum of hundreds of thousands pillars to support the layer above themselves that is just like the gecko’s multilevel hierarchy. In another way, due to the “optimal” Young’s modulus in gecko’s feet, the multilevel hierarchy can easily acquire by gecko. Eq. 8⁷² shows the lowest Young’s modulus needed for different conditions (as shown in Figure 3.11c).

$$E \geq \frac{8\gamma L^4}{3d^2 t^3} \dots\dots\dots (8)$$

Obviously, we can acquire the Young’s modulus for taper pillar that is much lower than sheer pillar used in the most of synthetic gecko adhesives. The result revealed the taper shape can break the limitation of material characteristics (such as Young’s modulus limitation) through successfully designed structure and shows an optimal

model which enhanced the stability and lifetime within the high adhesion, for any kind of material.

In addition to high aspect-ratio and small radius of structures, a directional angle of nanostructure is another crucial factor for anisotropic, reversible dry adhesive. It is because an angled structure significantly lowers the effective modulus of the surface from Eq. 9.⁷¹

$$E_{eff} = \frac{3EID \sin \theta}{L^2 \cos^2 \theta [1 \pm \mu \tan \theta]} \dots\dots\dots (9)$$

where E is the elastic modulus, I is the moment of inertia ($I = \pi R^4/4$, R is the radius of hair), D is the hair density, L is the hair length, μ is the friction coefficient, and θ is the slanted angle. According to Dahlquist criterion we have mentioned previously, the effective modulus should be less than 100 kPa for ensuring a tacky surface. If the structures are slanted, the effective modulus can be greatly reduced without the need of structures with extremely high AR, including the risk of self-matting and structural buckling within the limited modulus of polymers. As shown in Figure 3.12, for 80 nm nanohairs with aspect-ratio of 15 ($E = 19.8$ MPa, $D = 6.3 \times 10^8$ cm⁻², $\mu = 0.25$), the effective modulus decreases less than 100 kPa when the structures are slanted with less than 73° angle with respect to the horizontal plane.

Another fascinating property of the slanted structures is a controllable adhesion by varying the applied shear force. Efficient climbing relies on this behavior. By contrast, materials such as pressure-sensitive adhesive tapes require a substantial preload to achieve adhesion and a similarly large force to achieve detachment. The attached and detached mechanism of our slanted taper is shown in Figure 3.13.

3.3.3 Adhesive Properties for Taper Nanohairs

We hypothesize that the observed anisotropic behavior arises primarily due to

the stresses caused by the moment created when the taper is sheared. This can be understood by analysis of the rotation of the tip during shear loading in each direction (Figure 3.13). The original angle, ϕ , introduces a moment that is relative to the magnitude of the angle change from its undeformed state. The peeling moment is increased if the tapered pillar is sheared in the releasing direction because it increases the already present tip rotation to a larger angle (ϕ_r), increasing $\Delta\phi$ as seen in Figure 3.4.13c. This increased moment peels the leading edge, eventually detaching and overturning the fiber tip. However, when sheared in the gripping direction, the fiber tip begins to return to its original angle, reducing the moment to zero (Figure 3.13a). When the magnitude of the moment is near zero, the normal stress distribution at the interface is more evenly distributed, reducing the chances of detachment. After this point, if the shearing in the gripping direction is continued, $\Delta\phi$ changes and begins to increase in magnitude, eventually causing the leading edge (left) in detachment. The initial decrease in moment for shearing in the gripping direction increases the allowable displacement before detachment occurs, which means adhesion increased when shear force is applied in a preferred direction, in contrast to the releasing direction where the moment increases immediately. The increased displacement in the gripping direction allows the fibers to stretch and maintain contact, leading to high interfacial shear strength and anisotropy. All the shear and normal forces were recorded at the adhesive's failure point within our experiment. Taper shaped pillars we fabricated with slanted angle by pressure technique are shown in Figure 3.14.

The shear force was greatly reduced to 2.1 N/cm^2 when the sample was pulled in releasing direction, suggesting that the dry adhesive presented here can be used as a smart, directional adhesive patch with strong attachment ($\sim 21.5 \text{ N/cm}^2$) and easy detachment ($\sim 2.1 \text{ N/cm}^2$), with the hysteresis close to 13 as shown in Figure 3.15. A simple peeling model can also explain the strong directional adhesion capability.

According to the Kendall peeling model, the critical peel-off force (F_c) of a nanohair can be estimated with an assumption that the tip of slanted taper nanohairs forms intimate contact with the substrate as in an elastic tape, yielding⁷³⁻⁷⁴

$$P_{cr} = \frac{2\gamma b}{\sqrt{(1 - \cos \theta)^2 + \frac{2\gamma}{Et}} + 1 - \cos \theta} \dots \dots \dots (10)$$

where $\gamma = 100 \text{ mJ/m}^2$ is the adhesive energy, θ is the peel-off angle, and $b = 50 \text{ nm}$, $t = 100 \text{ nm}$ and $E = 19.8 \text{ MPa}$ are the width, thickness, and elastic modulus of the tape, respectively. Thus, the peel-off force can be expressed as a function of peeling angle for given parameters and the total peel-off force per unit area can be expressed by

$$P_{cr}(\text{total}) = \frac{2\gamma b}{\sqrt{(1 - \cos \theta)^2 + \frac{2\gamma}{Et}} + 1 - \cos \theta} \cdot D \dots \dots \dots (11)$$

where $D = 6.46 \cdot 10^8 \text{ cm}^{-2}$ represented the hair density. Figure 3.15 presented the peel-off force per unit area with varying peeling angles. As shown in Figure 3.15, the peel-off force increased gradually with a stronger shear adhesion force. When the adhesive was pulled in the reverse direction, however, the leaning angle of nanohairs is increased from its initial value of 60° to 180° , and thus the peel-off force is greatly reduced. According to Eq. 11, the peel-off forces are 21.5, 3.4, and 2.1 N/cm^2 for 0° , 90° , and 180° , respectively. The value of simulation is not quite fit with experimental data at a glance; however, the maximum value of simulation takes place at the angle around 0° which is scarcely possible on average day. Hence if the slanted angle was extended to 54° , the adhesion force will be around 8 N/cm^2 which agrees fairly well with our experimental results (maximum shear adhesion of $\sim 8 \text{ N/cm}^2$ in the forward

direction and $\sim 1.4 \text{ N/cm}^2$ in the reverse direction as shown in Figure 3.16. The diagram in Figure 3.17 gave us a comparison between taper shape and pillar shape, then we can find out the higher adhesion of taper shape than pillars'. There is still remaining a large space that we can improve from 8 N/cm^2 to 21.5 N/cm^2 from Figure 3.15. The possible reason which restricts the extension of slanted angle may be the way to measure is not efficient enough.

Gecko with special self-cleaning via walking steps is well known for scientists. Self-cleaning ability will occur rapidly as a consequence of energetic disequilibrium; particles tend to remain attached to the wall rather than to the spatula. For dirt or particle in daily life, equal energy is required to separate the particle from the wall and from the spatula. Unless particles are very small, many spatulas must be attached simultaneously to a single particle to balance the interaction energy between a spherical dirt particle and a planar wall (W_{pw}). Applying the same assumption from gecko to our taper shape structure, we may conclude the dirt will transfer to wall due to the difference between W_{pw} and W_{pt} (the interaction energy between a spherical dirt particle and taper pillar). Approaching this feature, an optimal density is required. It avoids particles for dropping down to the space between pillars but still keep the balance between W_{pw} and W_{pt} , and stability which can suffer several times of steps. Both optimal density and reliable stability could be reached by our taper structure. To get this goal, the super-hydrophobicity as the gecko's setal arrays composed of an array of β -keratin pillars is considerable with a water contact angle of 160° and with a contact angle of 93° on flat β -keratin surface but setal arrays from gecko. The water contact angle is usually used to measure self-cleaning ability. Getting the same results from our taper shaped structure, we observe the contact angle is increasing from 65° (hydrophilic) to 125° (hydrophobic). This is deserved to mention that this level of hydrophobicity is enough for daily using. From Table 3.3, taper shape clearly showed

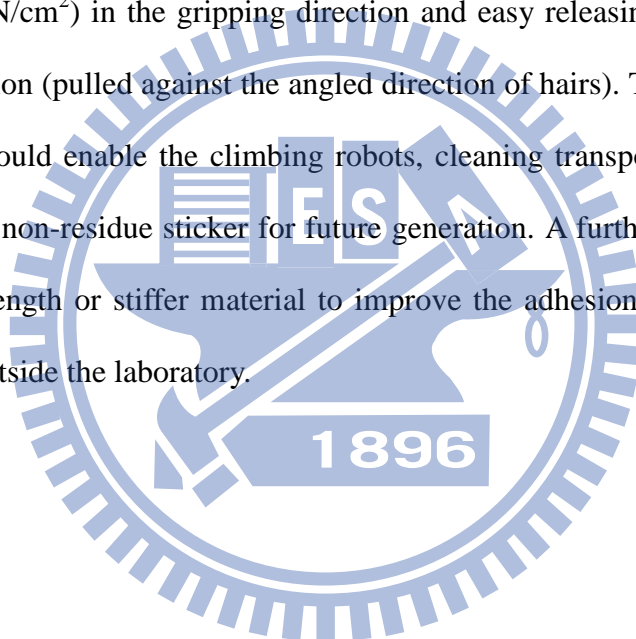
the advantage of self-cleaning ability over pillar shape. Explanations and reasons are as follows. Generally, high contact angle is induced by nanostructure and low sliding angle caused by nano- and micro-structures such as lotus leaf. Lotus is on behalf of super hydrophobic surfaces in Cassie's state, and exhibit a high CA and very low CA hysteresis. In another way, owing to its high adhesive (high CA hysteresis) properties, gecko is the representative of the high CA which is referred to contact area. The nano-slanted taper shape offered enough contact area for adhesion, while the contact area of microstructure or vertical structure is insufficient for high adhesion. Air trapping via nano- or micro-structure is critical for high CA; accordingly, efficiently trapped air is much more important than other factors. Both taper and pillar types are initially in Cassie's state and contribute very large fraction of air on the surface. Yet the air pockets of pillar type is in a flow tending condition, which is risky of transferring to Wenzel's state because of continuous interface with outside air from top to bottom. For taper type, sealed pockets will lead to flow unfriendly at bottom.

As a demonstration of the adhesion of the taper nanohair arrays, a small area of 1 cm^2 was evaluated through a frictional adhesion test as shown in Figure 3.18b. Figure 3.18a presented the mold and the tape of PUA after replicating. As to the measurement, a flexible adhesives with slanted nano-taper pillars attached to a glass slide that supported a counter weight in gripping direction under a preload of 0.5 N cm^{-2} . During the shear-adhesion test, no external normal load was applied. To verify the contamination, Figure 3.18c presented the adhesive after detaching from glass and the water droplet with high CA, which implied the water cleaning ability, on the adhesive, respectively.

3.4 Summary

We successfully presented an approach to fabricate angled taper nanohair arrays

as an excellent directional, reusable and water cleanable gecko-mimicking dry adhesive in large area. From Dahlquist's criterion, an ideal taper nanohair of PUA that consist a length of 1.3 μm and a diameter of 380 nm was designed. By using taper PAA mold via decoupling two-step HA process reported firstly by us, taper nanohairs with slanted angle were fabricated. The angled taper nanohair did facilitate the stability and self-cleaning properties compared with pillar nanohairs while still maintain a great directional adhesion. Moreover, remarkably directional force exhibited by angled taper nanohair arrays is showing here with strong shear attachment ($\sim 8 \text{ N/cm}^2$) in the gripping direction and easy releasing($\sim 1.4 \text{ N/cm}^2$) in the reverse direction (pulled against the angled direction of hairs). The smart adhesive presented here would enable the climbing robots, cleaning transport system such as LCD factory and non-residue sticker for future generation. A further study should be done on longer length or stiffer material to improve the adhesion capability against rough surfaces outside the laboratory.



	MA	HA
Applied voltage (V)	160	190
Current density (mA/cm²)	3	20
Growth rate (μm h⁻¹)	10	60
Interpore distance (D_{int}; nm)	405	380
Porosity (P; %)	10	3

Table 3.1 MA versus HA in 2.5% H₃PO₄.



	Material (Young's modulus)	Shear adhesion	Durability	Directional adhesion	Self- cleaning
Natural Gecko ⁷	β -keratin (2 GPa)	10	> 30000	Yes	Excellent
Our work	PUA (19.8 MPa)	8	> 100	Yes	Good
Angled pillar ¹⁴	PUA (19.8 MPa)	11	N/A	Yes	No
Slanted Pad ²⁷	PP (1 GPa)	4.5	N/A	Yes	No
Pillar ¹⁹	<i>h</i> -PDMS (11 MPa)	0.05	N/A	No	Good
Hierarchical Tip ²³	PDMS (1.8 MPa)	2	N/A	No	No
Angled spatulata ²⁵	PU (3 MPa)	10	> 100	Yes	No

Table 3.2 The comparison between different types of polymer-based gecko adhesives (N/A represents “no information”).






Plane PUA	Pillar PUA	Taper PUA
		
CA = 65°	CA = 94°	CA = 125°

Table 3.3 Measurement of contact angle for various cases with a dry adhesive pad.



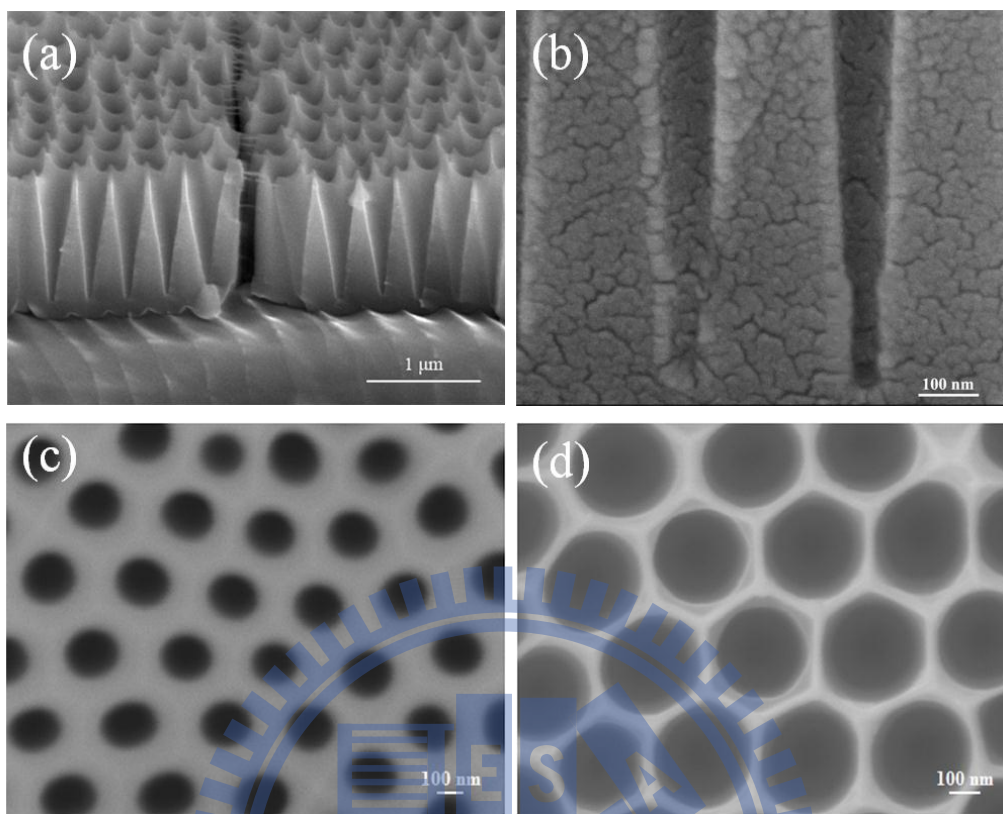


Figure 3.1 SEM image of our taper shape PAA. (a) The cross-sectional image showed a length of 1.4 μm . (b) The magnified image of channel tips. Top-view images of the pore-widening time in (c) 3 min and (d) 15 min.

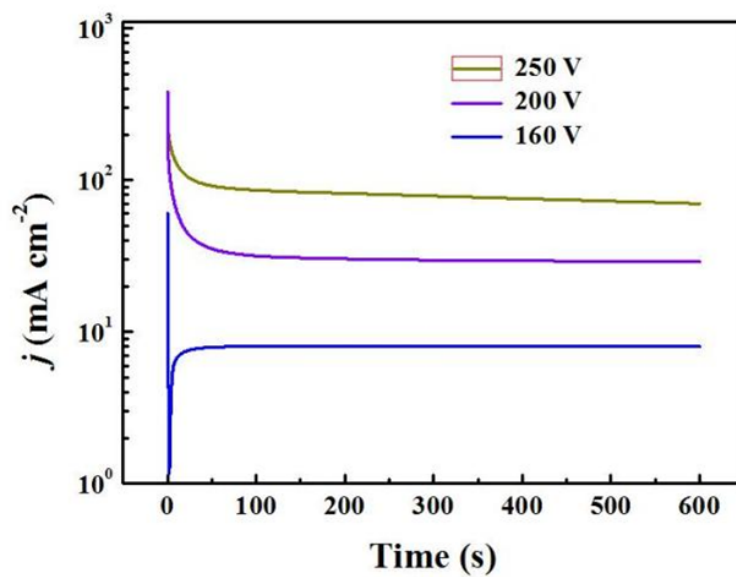
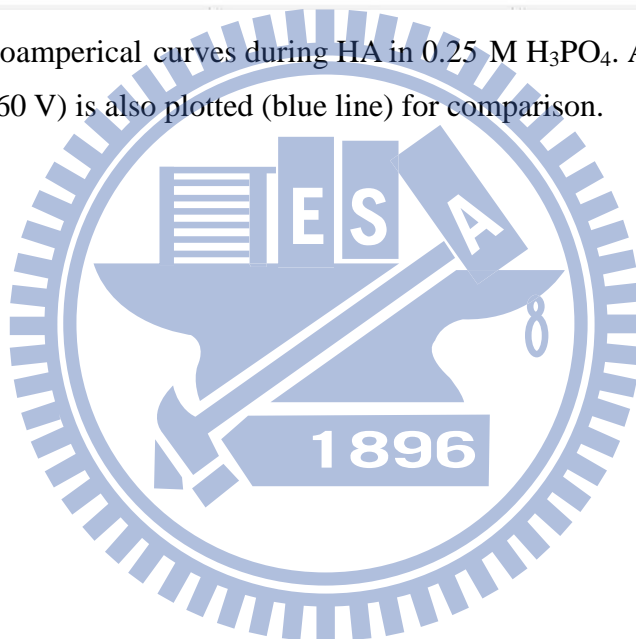


Figure 3.2 Chronoamperical curves during HA in 0.25 M H₃PO₄. A conventional MA (0.25 M H₃PO₄, 160 V) is also plotted (blue line) for comparison.



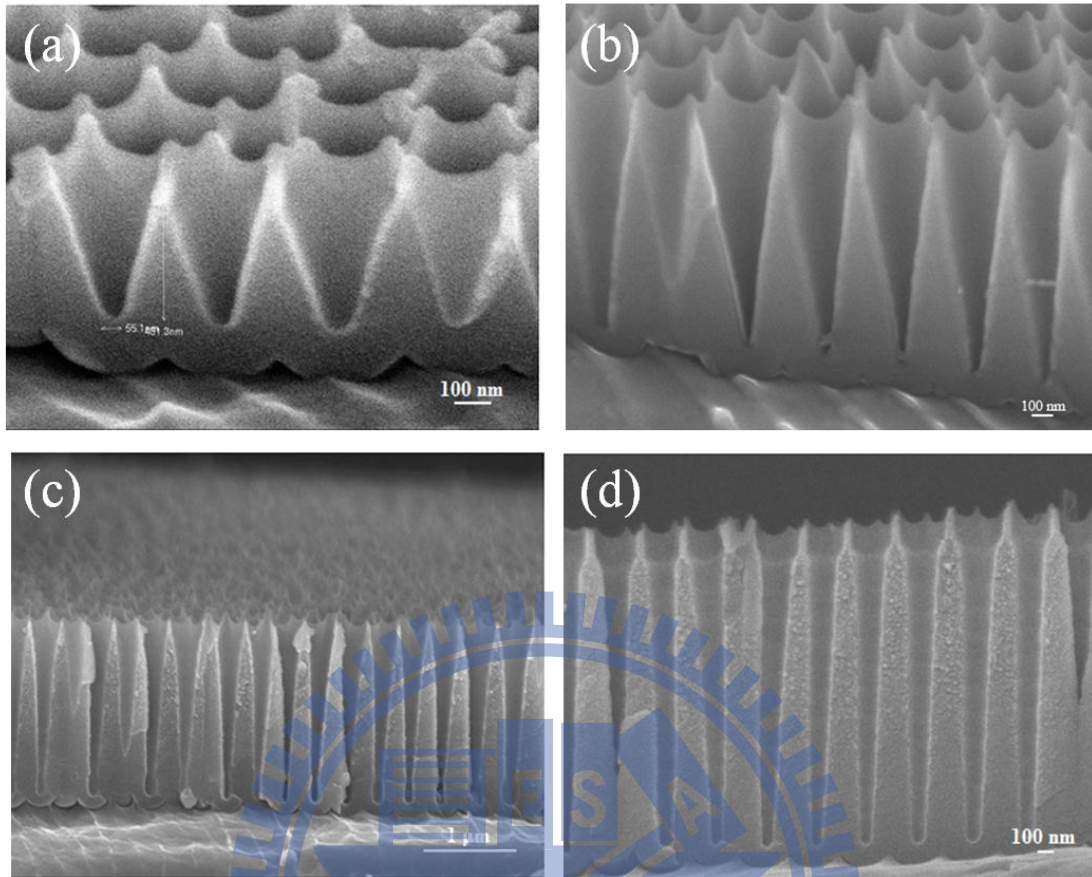


Figure 3.3 SEM images of taper PAA with different lengths: (a) 600 nm, (b) 1.1 μm , (c) 1.8 μm , and (d) 2.3 μm .

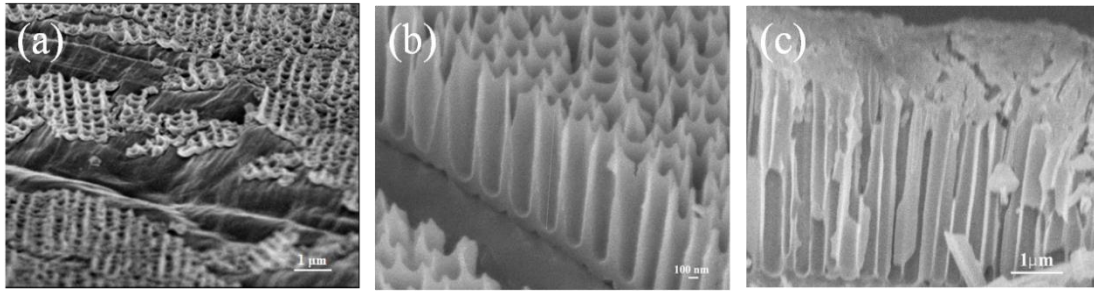


Figure 3.4 Processing anodization in H_3PO_4 with different concentration. (a) 1% which cannot offer enough ionic species. (b) 5% and (c) 10% with excess joule heat from current densities.



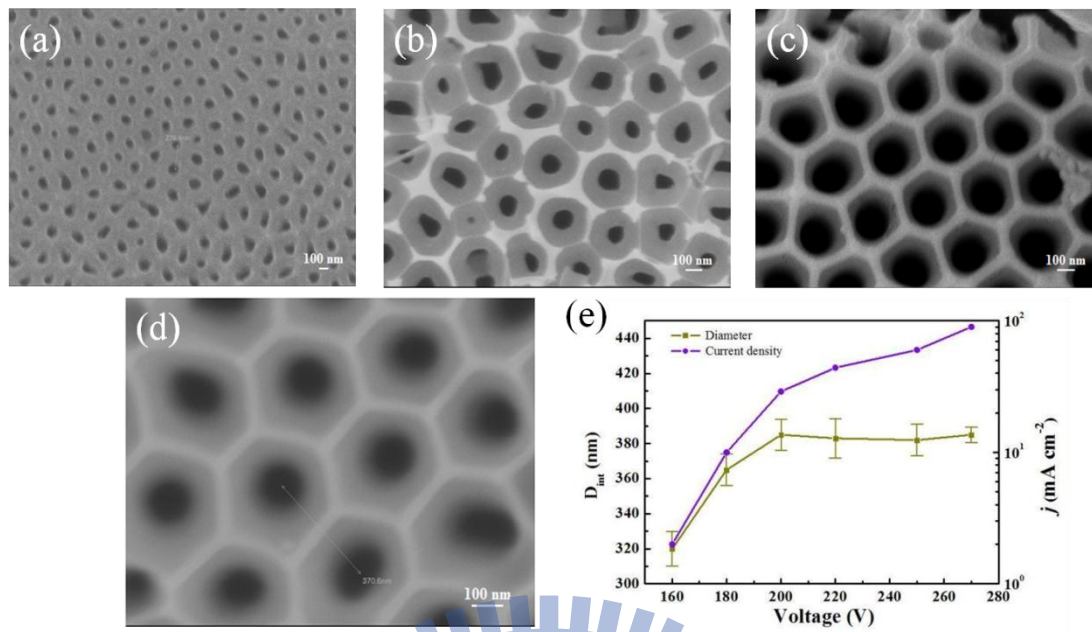
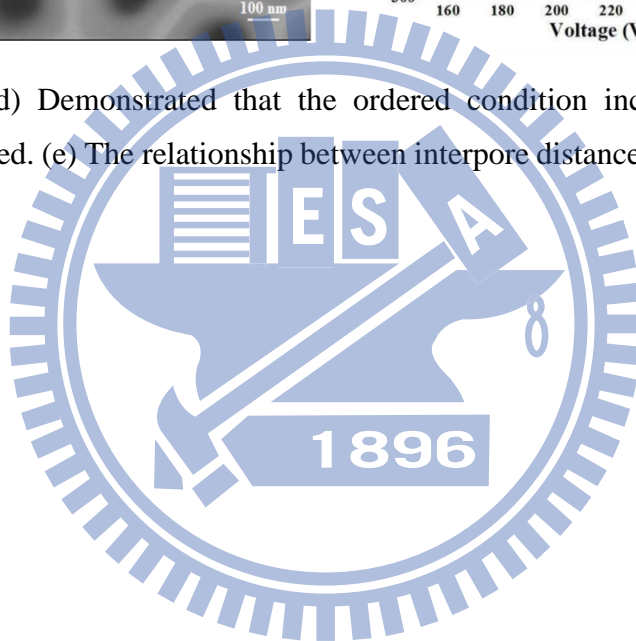


Figure 3.5 (a)-(d) Demonstrated that the ordered condition increased as voltage parameter increased. (e) The relationship between inter-pore distances, current densities and voltage.



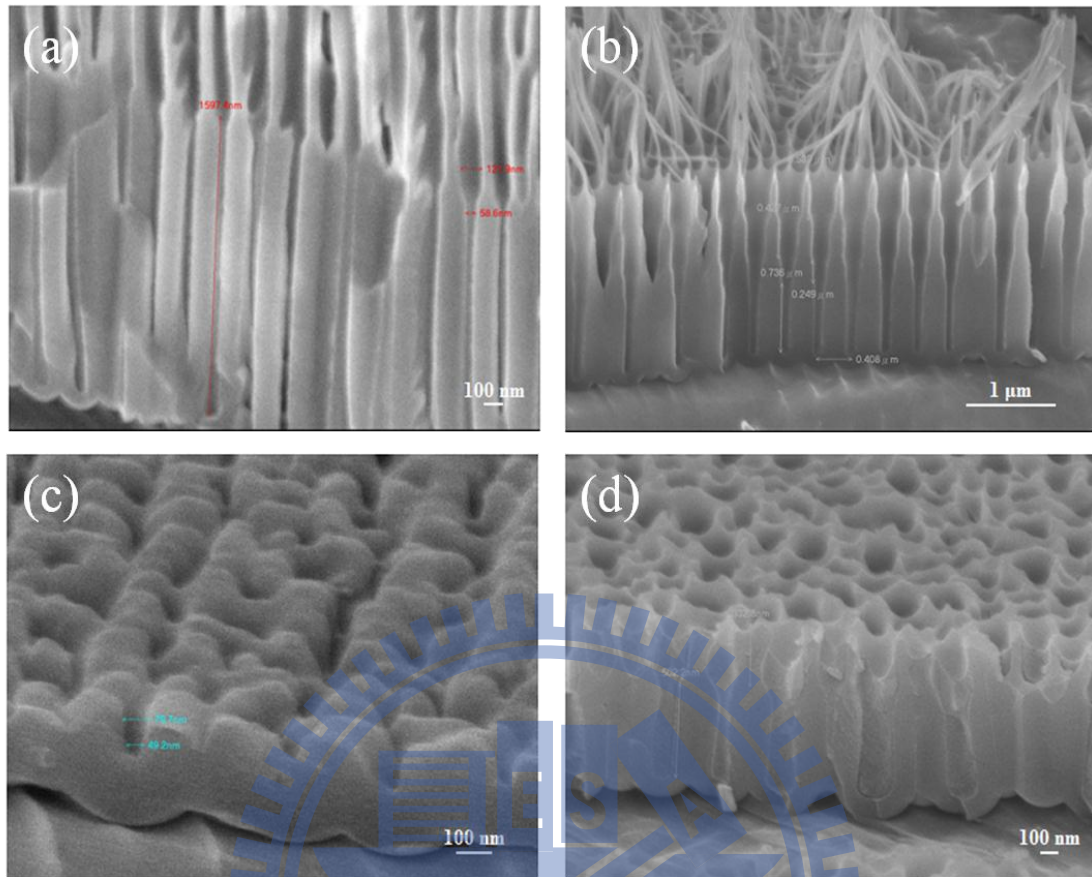


Figure 3.6 SEM images of decoupling system. (a)-(b) Optimal processing widows in both first and second step. Unmatched voltage cause a bad result because the applied voltage at second step is (c) insufficient and (d) excess to fit the optimal condition.

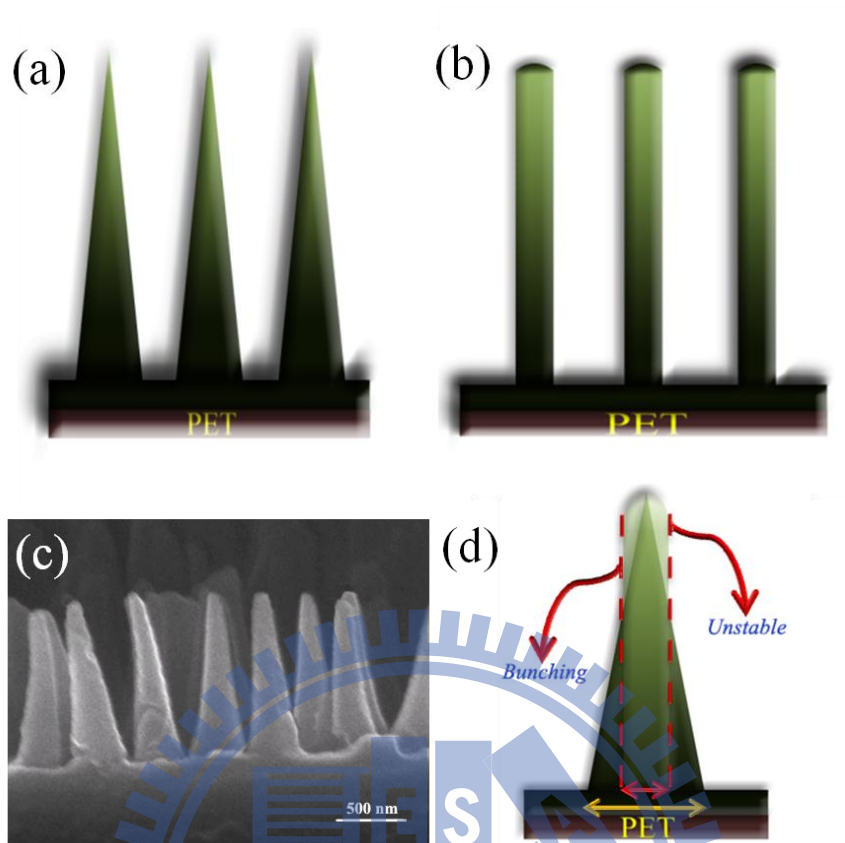


Figure 3.7 (a) Taper shaped pillars profile sketch map. (b) Pillar shape profile sketch map. (c) SEM image of taper shaped pillars and (d) Illustration of taper's advantage.

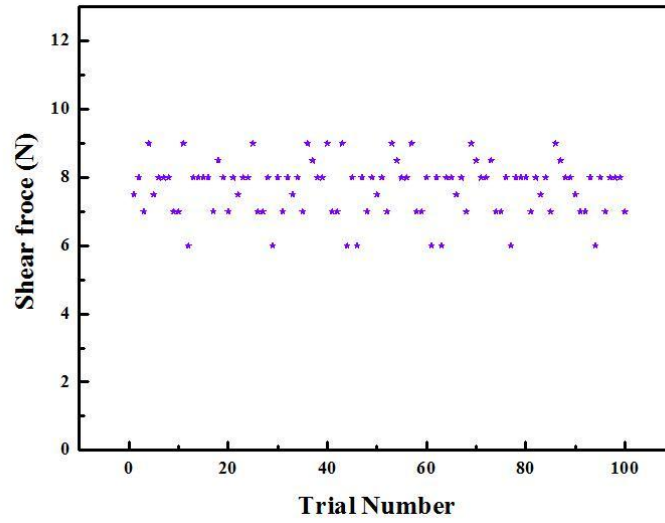
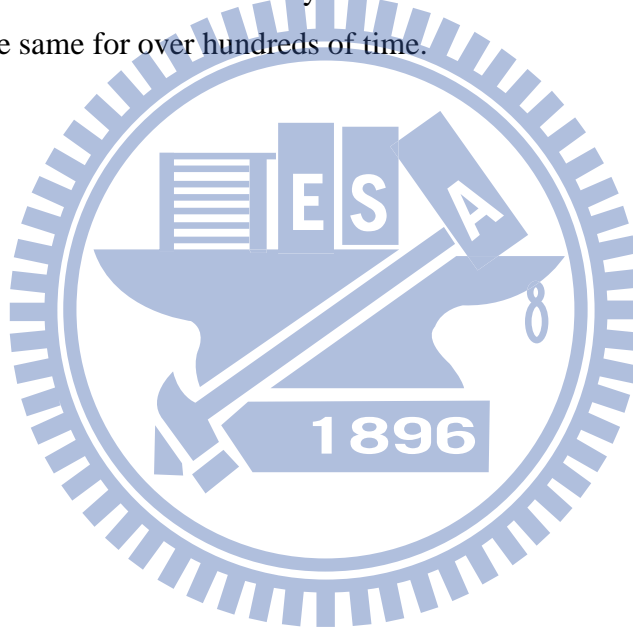


Figure 3.8 Force measurements versus cycles of attachment and detachment, and the force remained the same for over hundreds of time.



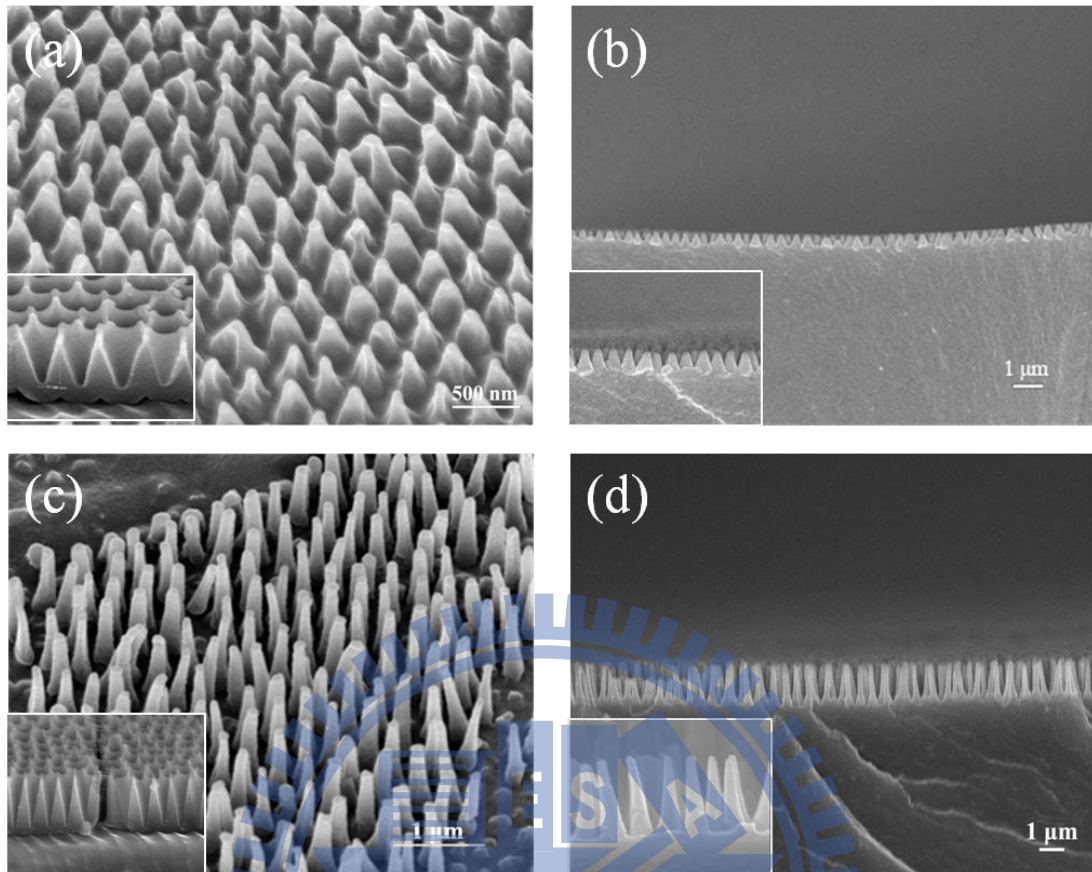


Figure 3.9 Taper pillars with different lengths. (a) 600 nm from tilted SEM image (b) 600 nm from cross SEM image. (c) 1.4 μm from cross SEM image. (d) 1.4 μm from cross SEM image. The insets showed the molds of replicating or SEM images of high magnification, respectively.

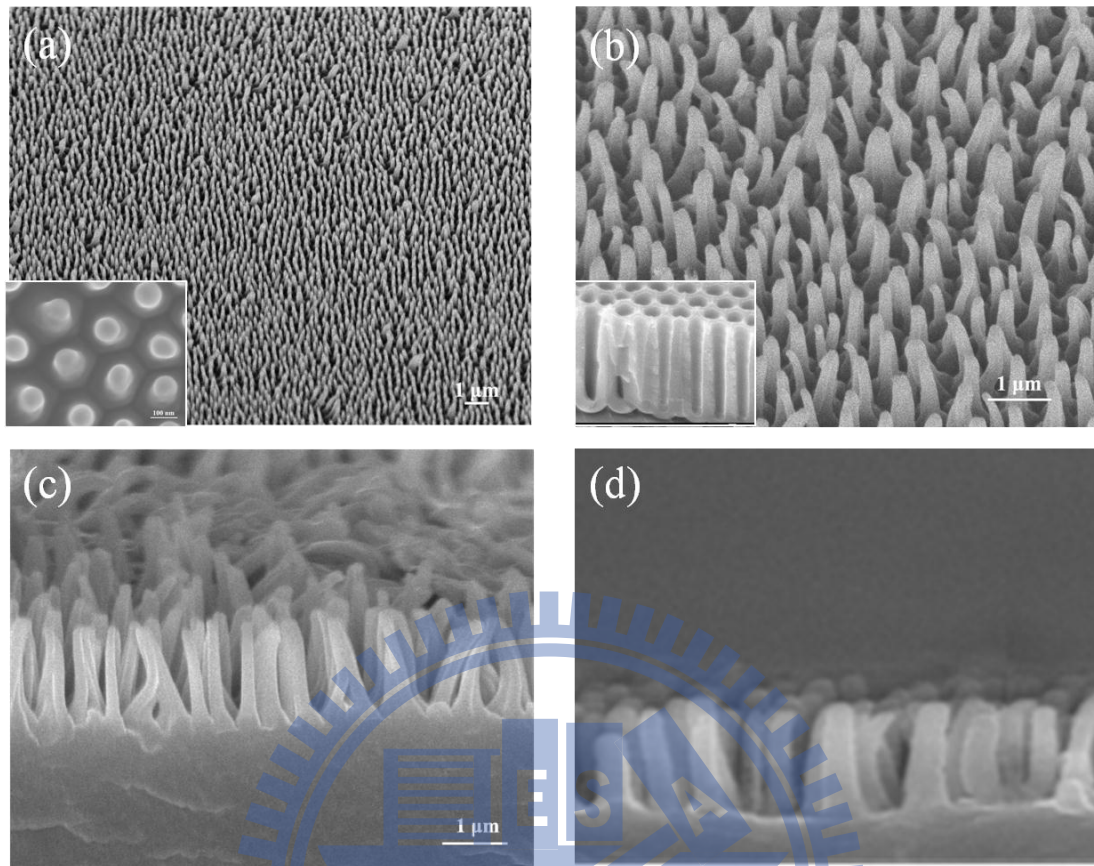


Figure 3.10 SEM images of taper and pillar nanostructures. (a) Low magnification of our structure and the inset is the top view image that displays the taper edge and hexagonal arrays. (b) Tilted SEM image of the pillar shape showing this type cannot support the same height as the taper shape and (c) SEM image from cross-section. (d) Stable pillar with decreasing the length.

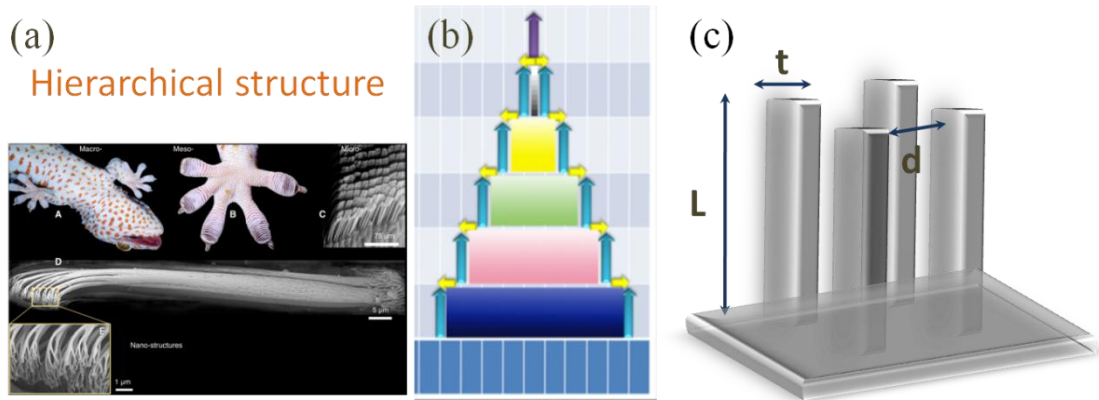


Figure 3.11 Illustrated hierarchy (a) of gecko and (b) of taper shape as a hierarchy-like by “cake” model. (c) Illustration of Eq. 8.



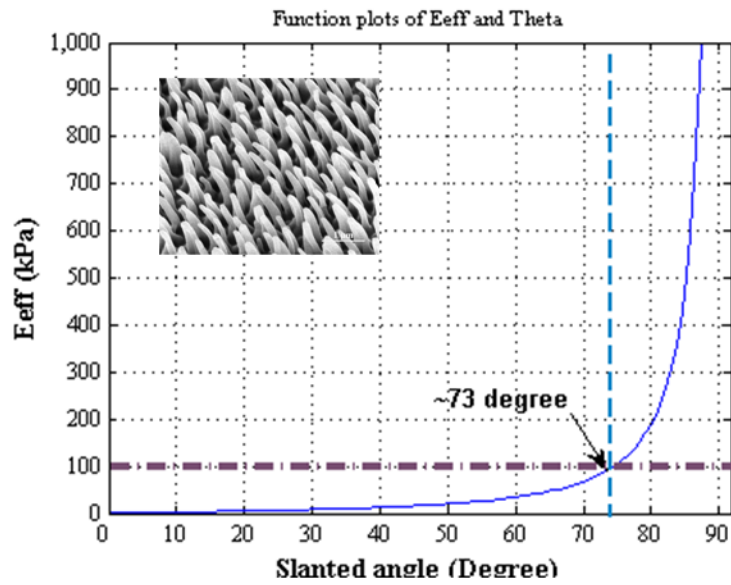
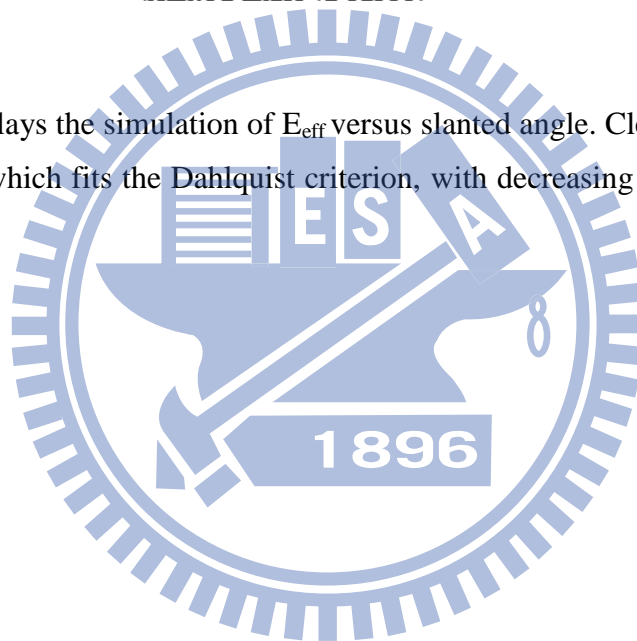


Figure 3.12 Displays the simulation of E_{eff} versus slanted angle. Clearly, the E_{eff} drops below 100 kPa, which fits the Dahlquist criterion, with decreasing slanted angle after 73° .



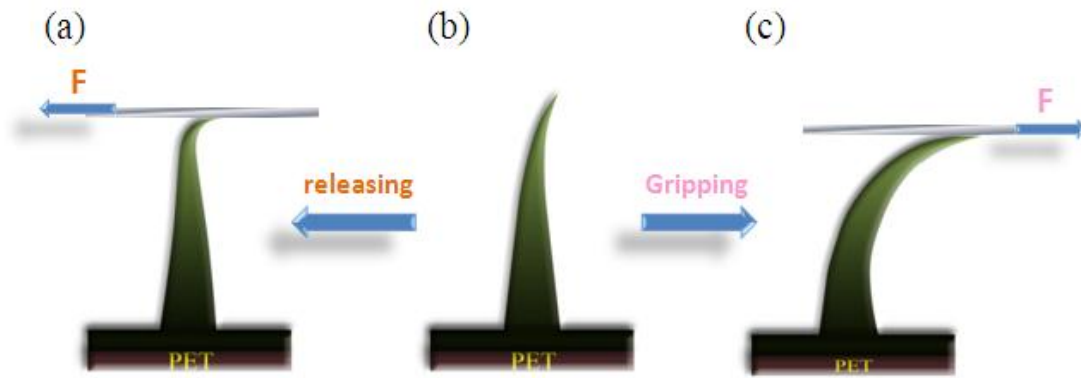
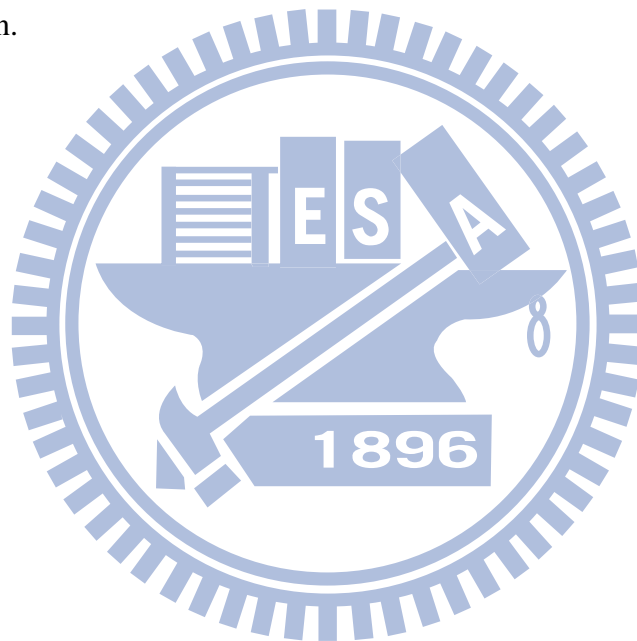


Figure 3.13 Theoretical analysis of directional adhesion mechanism of the slanted taper shaped pillars. An illustration showed the change of leaning angle of the slanted taper nanohairs when the adhesive is pulled in (a) the gripping, (b) initial state and (c) releasing direction.



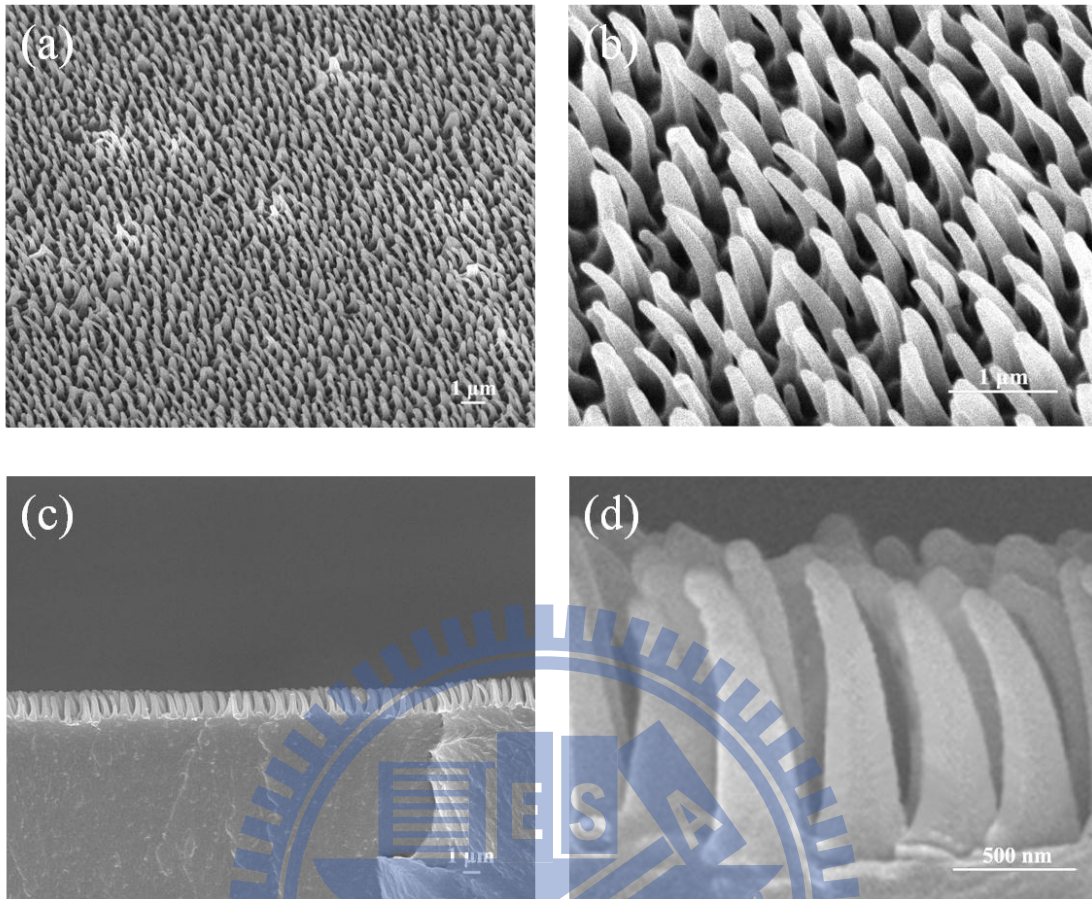


Figure 3.14 Taper shaped pillars with slanted angle we fabricated by pressure technique. (a) Low magnification. (b) High magnification of tilted SEM image of the structure. (c) Low magnification and (d) high magnification from cross-sectional view.

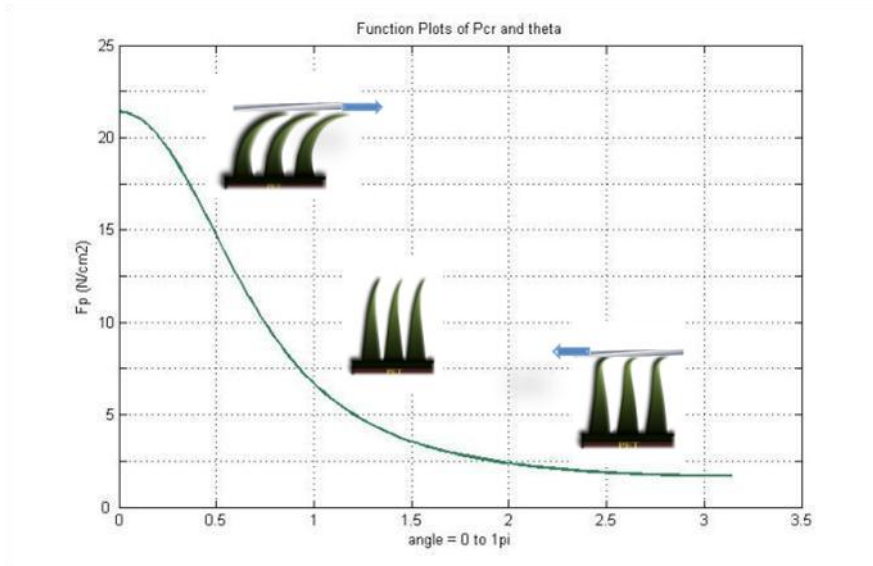
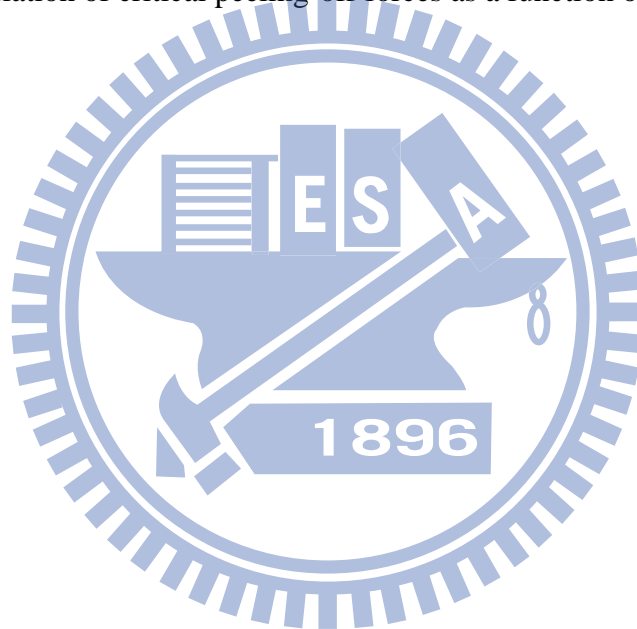


Figure 3.15 Simulation of critical peeling-off forces as a function of peeling angle.



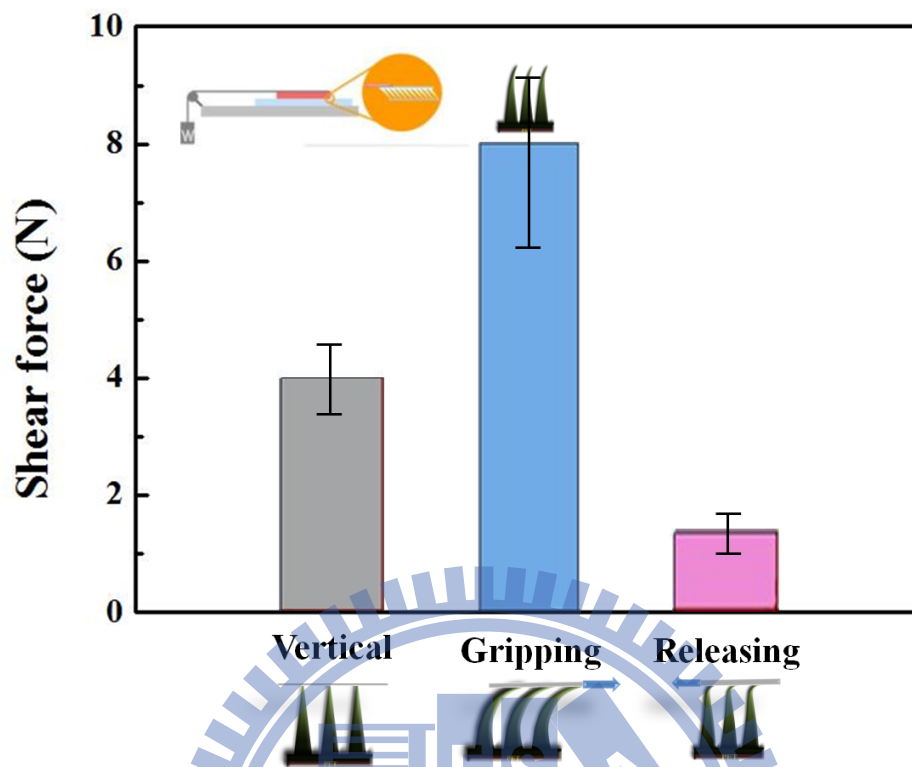


Figure 3.16 Measurement of shear force for various cases with an adhesive patch of 1.0 cm². The taper nanohairs were composed of soft PUA.

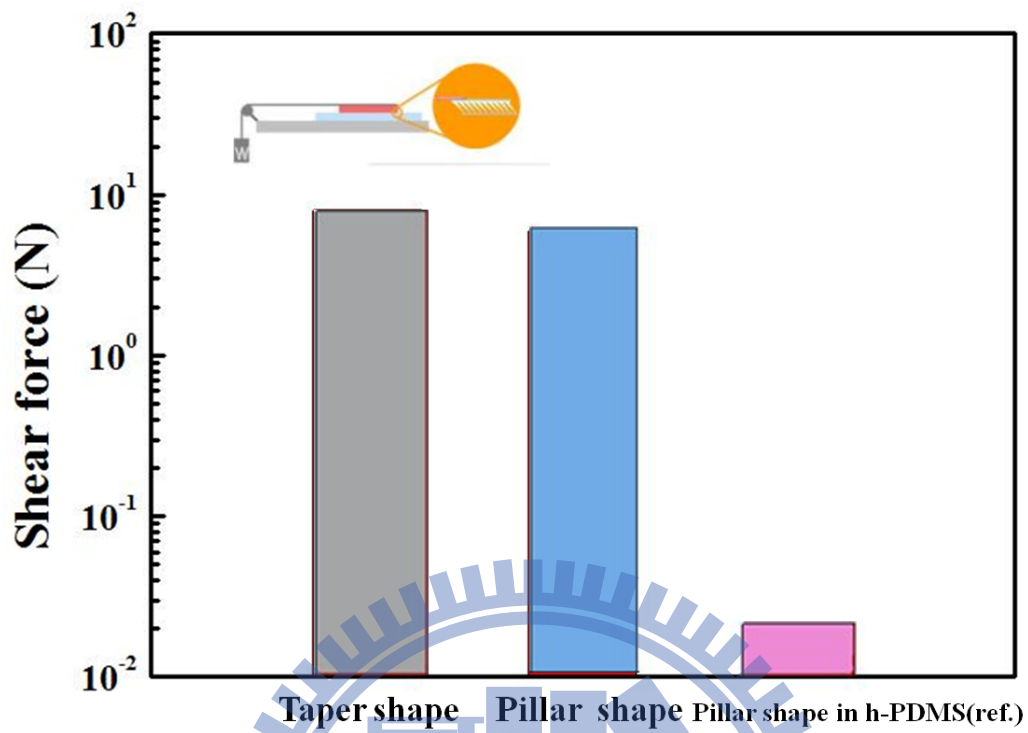


Figure 3.17 Giving a comparison between taper shape and pillar shape, we can find out the higher adhesion of taper shape than pillars' can account for the higher density, longer length or adhere efficiently we have discussed previously.

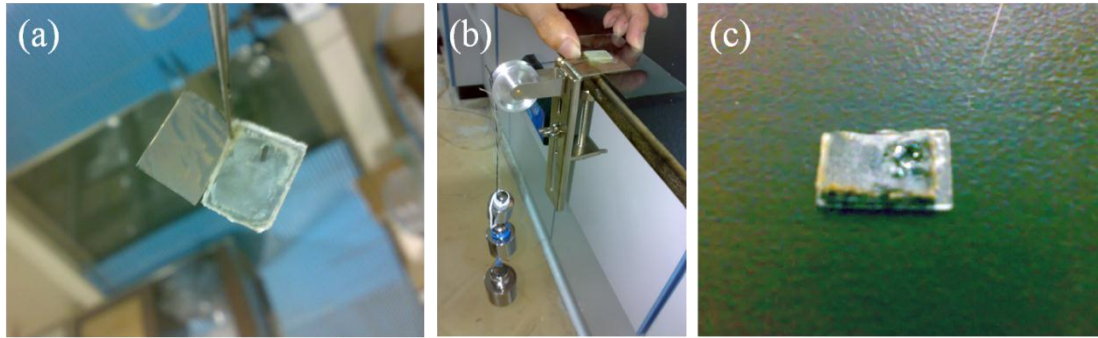


Figure 3.18 Photographs of (a) tape of PUA after replicating and the mold. (b) Counter weight measured system. (c) The high CA of tape after detaching from the glass.



Chapter 4: Kiss from a Rose: Bioinspired Superhydrophobic and High-Water Adhesive Surfaces for Innovative Imprint Technique

4.1 Introduction

Approximately 460 million years ago, the first plants moved from their aqueous environment to the drier atmosphere on land, and they needed a protective outer coverage. The development of the cuticle as hydrophobic outer coverage was one of the key innovations that enabled plants to leave their primarily aquatic habitat and to overcome the physical and physiological problems connected to an ambient environment, such as desiccation. Some naturally occurring plant leaves such as those of the lotus have well-demonstrated superhydrophobic surfaces such that water drops can easily roll off and carry away dust particles and debris, a mechanism often referred to as self-cleaning.¹⁻³ The self-cleaning of lotus leaves in particular is a popular topic of study because of the observed wetting properties of the material surfaces.⁴⁻⁶

4.1.1 Lotus Effect: A Superhydrophobic and Self-Cleaning Surface

Lotus leaves are one of the most famous examples among naturally occurring superhydrophobic surfaces.³ The water contact angle (CA) of a lotus leaf is $161 \pm 2.7^\circ$ with CA hysteresis of 2° .⁷⁻⁸ The structure of a lotus leaf consists of a combination of a two scale roughness: one around $10 \mu\text{m}$ (rough structure) and one around 100nm (fine structure). These surfaces are also referred as hierarchical micro- and nano-structures.⁹⁻¹⁰ The hydrophobicity of a lotus leaf arises from the epicuticular wax

secreted by the leaf itself.¹¹ The wax has a contact angle of 110°, not highly hydrophobic; however, the lotus leaf still exhibits a superhydrophobic property. It is presumed that this combination of roughness and wax contribute to the superhydrophobicity of the lotus leaf.^{9,12} The rolling off of water droplets and collecting the contaminants from the lotus leaf is dubbed as the “lotus effect”. The lotus leaf therefore always exhibits a very low degree of contamination: self-cleaning. The hierarchical structured surface of the lotus leaf provides a model for the development of biomimetic self-cleaning surfaces. On these water-repellent surfaces, water droplets move easily at a low inclination of the leaf and collect dirt particles adhering to the leaf surface.¹³

Wettability of a solid surface is an important property because controlling the surface wettability is crucial in many practical applications in MEMS and biomaterials etc.¹⁴⁻¹⁶ If a droplet of liquid is placed on a solid surface, the solid–air and liquid–air interfaces come together under the static or most stable CA (contact angle), θ_y (Figure 4.1a). The value of θ_y can be determined from the condition of the total free energy of the system being minimized and is given by the so-called Young–Dupre equation¹⁷⁻¹⁸ for the CA showed as:

$$\cos \theta_y = \frac{\gamma_{SA} - \gamma_{SL}}{\gamma_{LA}} \dots\dots\dots(1)$$

where γ_{IJ} designates the surface tension (or energy) between phase I and J (S: solid, A: air and L: liquid). For a rough solid surface that consists of asperities and valleys with a typical size of roughness details smaller than the size of the droplet (Figure 4.1b), the CA θ_w was calculated by Wenzel¹⁹ as:

$$\cos \theta_w = r \cos \theta_y \dots\dots\dots(2)$$

where $r = A_{SL}/A_F$ is a roughness factor defined as a ratio of the solid–liquid area A_{SL} to its projection on a flat plane, A_F . Wenzel’s relation embodies two types of behavior:

1. If $\theta_y < 90^\circ$ (hydrophilic solid), we will have $\theta_w < \theta_y$ since $r > 1$.
2. Likewise, if $\theta_y > 90^\circ$, we will have $\theta_w > \theta_y$.

Thus roughness magnifies hydrophobic and hydrophilic properties of a surface and by roughening a material with low surface energy, superhydrophobicity can be achieved.

For a rough surface, a composite solid–liquid–air interface may form air pockets at the valleys between asperities with the flat fractional geometrical area of the solid–liquid and solid–air interfaces under the droplet f and $1 - f$, respectively (Figure 4.1c). Transition to the composite interface increases CA and dramatically decreases solid–liquid contact area, and therefore decreases adhesion of liquid to solid, allowing the droplet to roll easily along the solid surface. Cassie and Baxter²⁰ found that for fractional solid–liquid and solid–air interfaces, the CA is given by:

$$\cos\theta_c = r f \cos\theta_y - 1 + f \dots\dots\dots(3)$$

Equation (2) may now be considered a special case of Equation (3) with $f=1$ (no air under the droplet). For a heterogeneous interface consisting of two fractions with the CAs θ_1 and θ_2 , and the fractional areas f_1 and f_2 (so that $f_1 + f_2 = 1$), the Cassie and Baxter equation has the form:

$$\cos\theta_c = f_1 \cos\theta_1 + f_2 \cos\theta_2 \dots\dots\dots(4)$$

Equation (4) is reduced to Equation (3) in the limiting case of $\cos\theta_1 = -1$ (corresponding to the contact with air pockets, with $\theta_1 = 180^\circ$), $\theta_2 = \theta_y$, $f_2 = f$, and $r = 1$ (e.g. flat-top surface). The opposite limiting case of $\cos\theta_1 = 1$ corresponding to $\theta_1 = 0^\circ$ (water-on-water contact) yields $\cos\theta_c = 1 + f(\cos\theta_y - 1)$. This form of the Cassie-Baxter equation is used sometimes for the homogeneous interface instead of Equation (3), if the rough surface is covered by holes filled with water.

4.1.2 Rose-Petal Effect: A Superhydrophobic and High Adhesive Surface

Hierarchical micropapillae and nanofolds are known to exist on the petals’

surfaces of red roses. These micro- and nano-structures provide a sufficient roughness for superhydrophobicity and yet at the same time a high adhesive force with water. A water droplet on the surface of the petal appears spherical in shape, which cannot roll off even when the petal is turned upside down. Jiang et al. firstly defined this phenomenon as the “petal effect” as compared with the popular “lotus effect”.²¹ From the point of practical applications, this surface will be more useful in the synthesis of chemical engineering materials and microfluidic devices.²²

Superhydrophobic surfaces with different dynamic wettabilities, such as water repellent or water adhesive, have attracted increasing interest recently.²³⁻³⁰ The lotus leaf, with ultrahigh water contact angle (CA) and low sliding angle (SA), is widely known as a model superhydrophobic surface because of its self-cleaning property. Although superhydrophobic surfaces with high SA cannot be self-cleaning, they have many other potential applications, such as in the field of microfluidic control systems.³¹⁻³⁷ Superhydrophobic surfaces that can “pin” liquid droplets have been demonstrated for no-loss microdroplet transfer or trace-liquid reactors.³⁸⁻⁴⁴ The ability of adhesive force to liquid is caused by van der Waals’ force and capillary force. It is known that superhydrophobicity is effective for obtaining a small liquid interfacial contact area, at least for water-based liquids, which significantly reduces the mass loss in microdroplet transfer.⁴⁵⁻⁴⁶

In fact, before “petal effect” was observed by Jiang et al., some nanostructures have demonstrated with superhydrophobic and water adhesive properties. Gao et al.⁴⁷ designed a nanotube array based on basic principles of roughness-enhanced hydrophobicity and capillary-induced adhesion. The nanostructures were prepared with the simple electrochemical anodizing of pure Ti sheets and then treated with a methanolic solution of tetraethoxysilane. The surface adhesive force may be effectively tuned by solid–liquid contact ways and the fractions of air pockets in open

and sealed systems, which depend on the nanostructure configurations. In addition, authors found that the water adhesive force of the superhydrophobic NTA nanostructure surface could be tuned with changing the diameter of nanotubes and also the length of nanotubes, which was ascribed to the negative pressure changes caused by the volume changes of the air, sealed in the nanotubes.⁴⁸ Dressick et al. have introduced a bottom-up process based on oblique angle deposition as a simple, robust method for controlling the morphology of poly-(p-xylylene) (PPX) films. They fabricated superhydrophobic films through the chemisorptions of fluoroalkylsiloxane coatings to hydroxyl sites created on the PPX film surface and controlled both water wettability and adhesion through appropriate choices of PPX surface chemistry and roughness. The structure is able to pin a water droplet on the fabricated surface. These results suggested that van der Waals and/or capillary forces sufficient to induce wetting behavior associated with the intermediate state are present for the structured PPX films.⁴⁹ Pogreb et al. fabricated the surfaces which had high apparent contact angles accompanied by high adhesion of water droplets similar to the rose petal. The surface was prepared by spreading lycopodium particles on the extruded polyethylene film and hot pressed with a crimped template. This observation resembles the petal effect reported by Jiang et al. It is reasonable to relate the high adhesion of the droplets to the Wenzel wetting regime occurring on the lycopodium.

However, those structures as above mentioned show either too strong water adhesive abilities or poor surface retention. If we consider such superhydrophobic and water adhesive structure as liquid transportation application, moderate water adhesive ability, surface stability and large-scale fabrication are indispensable. So far only Jiang et al. successfully fabricated the artificial structure of rose petal surface by using flash rose petals as a mold to duplicate the micro- and nano-structure. The fabricated polystyrene (PS) surfaces which have morphology like rose petals' surface exhibited

superhydrophobicity and high water adhesion.⁵⁰ The high adhesive force of the replica can be explained according to the Wenzel model. The water droplet can be pinned on the surface, because of the strong capillary force of the cone-shaped microstructures, which can force the water into the grooves of the surface. Therefore, the resulting replica shows superhydrophobicity with high adhesive force.

4.2 Materials and Methods

Chemicals and Materials. Phosphoric acid (H_3PO_4 , 95%), sulfuric acid (H_2SO_4 ; 98%), anhydrous ethanol (99.5%), and hydrogen peroxide (H_2O_2 , 30%) were purchased from J. T. Baker. Glutaraldehyde ($\text{CH}_2(\text{CH}_2\text{CHO})_2$, 25%), and paraformaldehyde ($\text{OH}(\text{CH}_2\text{O})_n\text{H}$ with $n = 8\sim 100$, powder, 95%) were purchased from Sigma-Aldrich. Nitric acid (HNO_3 , 60%), poly-(vinyl-alcohol) (PVA, 87% hydrolyzed, high molecular weight of 88,000-97,000), polystyrene latex microsphere (PS, 30 μm in diameter), osmium tetroxide (OsO_4 , 99.8%) and sodium phosphate dodecahydrate ($\text{Na}_3\text{PO}_4 \cdot 12\text{H}_2\text{O}$, 97%) were purchased from Alfa Aesar.

Wrinkle Formation on Plane PDMS. PDMS was prepared by mixing silicone base (reagent A) and curing agent (reagent B) in a weight ratio of 10:1. After degassing, the mixture was heated at 80°C for one hour. The PDMS layer, which had the size of 1 cm^2 in area and 0.1 cm in thickness, was fixed on a glass slide. Then the bilying sample was immersed in a sulfuric acid solution, made of sulfuric acid/nitric acid in different volume ratio), for several seconds. After acid treatment, it was immediately submerged into a cold bath of 1°C for thirty seconds. Finally, the sample was dried by N_2 purging and an overnight post-baking in oven.

Petal-like PDMS Surface Manufacture. The experimental protocol to mimic the petal-like PDMS surface was schematized in Figure 4.2. First of all, the 2.5 wt% PS beads, which had 35 μm in diameter, were spread on a clean Si wafer chip treated

with O₂ plasma. It was dried in barometric pressure until the total water was vaporization. Then the two-dimensional close-packed PS beads were formed owing to the water vaporization. Thereupon, PVA solution of 15 wt% was spread on a Si chip. A PVA-PS film was peeled from the wafer when the solution was dried at atmosphere pressure. The film we received was slightly polished by using sandpaper. Afterwards, it immersed in an acetone solution accompanied with ultrasonic bath to remove the PS beads. Then the treated PVA film, replicated from the cross-packed PS beads, was used as a negative mold. When the PDMS sample was dried, we peeled it off and fixed it onto a clean wafer. Finally, the PDMS sample undergone an acid corrosion process as same as we mentioned in the last paragraph.

Fresh Petal Dehydration. Firstly, the fresh rose's petal was sliced up into little chips had a size of 0.5 cm². The chip was immersed in a phosphate buffer solution (0.1 M) composed of 2 wt% glutaraldehyde and a 4 wt% paraformaldehyde for 2 hours. The prepared petal was then immersed in a phosphate buffer solution (0.1 M) composed of 2 wt% osmium tetroxide for 2 hours. Subsequently, the pre-treated petal was washed by the phosphate buffer solution thoroughly. Afterward, the cleaned petal was processed through a dehydration process by using a series of alcohol solutions whose concentrations are 20%, 30%, 50%, 70%, 80%, 90% and 100%, respectively. The treated sample was submerged by each alcohol solution for 20 minutes and then immersed in an acetone solution for 20 minutes. It shall be repeated three times before migrating to next high concentration alcohol solution. Eventually, the dried sample had to undergo a critical point dry by a carbon dioxide liquid ensured total water was removed from the petal.

Characterization. The periodic wrinkles on PDMS surfaces were observed by an inverted light microscopy (Olympus CKX41). The morphology of the micro- or nanostructure of the prepared PDMS sample, close-packed PS beads on wafer and

duplicated PVA film was observed by a field-emission scanning electron microscopy (JEOL, JSE-6700F). A measurement of a static contact angle is a general method to understand the wetting phenomena of a surface. A surface with a static contact angle larger than 150 degree is regarded as a superhydrophobic surface. The resulted contact angle averaged measurements of five different positions on the same surface. Fourier transform infrared spectrometer (FTIR) as a useful technique for characterization of polymeric materials has been firmly established. We prepared the specimen by scrapping the treated surface then mixture the bits and small pieces with potassium bromide powder. After that, we grinded the mixtures to a small size and pressed the mixtures to a chip. Finally, the chip was then characterization by FTIR (Nicolet Avatar 320).

4.3 Results and Discussions

4.3.1 Superhydrophobic Periodic Wrinkles on Plane PDMS

Plane PDMS was treated by a strong acid composed of sulfuric acid and nitric acid with several reaction conditions as listing in Table 4.1. The resulting surfaces were examined by an inverted microscope; the photographs were showed in Figure 4.3 and Figure 4.4. The random orientation of wrinkles was observed, but a regular periodicity of these wrinkles was revealed. Figure 4.3a to d showed the periodicities ranging from 4.3 μm to 26.3 μm according to different immersion times of 5 s, 15 s, 30 s, and 60 s, respectively. Another experimental condition was illustrated in Figure 4.4a-d. The treated surfaces with periodicities ranged from 26.3 μm to 109.8 μm under appropriate immersion time of 5 s, 15 s, 30 s, 60 s, respectively. We analyzed the results of Figure 4.3-4 which were plotted in Figure 4.5. It is concluded that the periodicity increases with immersion time and the proportion of sulfuric acid in the mixture acid. Another variable—the temperature of acid solutions—was investigated

for the sake of the command of periodic wrinkles. Figure 4.6 revealed the relationship between reaction temperature and the resulting periodicity—a proportional increase of the periodicity to the reaction temperature. The temperature increased from 20°C to 50°C led to a slight increase of periodicity from 8.6 μm to 14.2 μm . Herein, we acquired an approach to modulate the periodicity of the wrinkle by altering the proportion of sulfuric acid in the mixture acid, the reaction time and the reaction temperature. After examining the microstructure, we used SEM to obtain the nanostructure as shown in Figure 4.7. It is interestingly noted in Figure 4.7c that the bulges with an average diameter of 50 nm appeared under large-scale observation. As shown in Figure 4.7d, the structures on the wrinkle would lead to a superhydrophobicity with a contact angle of 151.5°, while a blank PDMS plane showed a contact angle of approximate 90°.

The spontaneous formation mechanism of periodic wrinkles of double layers systems have been studied by many scientists, for instance, metal/soft-polymer film;⁵¹ moreover, PDMS surface treated by O₂ plasma could cause the similar phenomenon. In our experiment, plane PDMS was fixed onto a silicon wafer; the top of PDMS was treated by acid solution. It resulted in two layers: one was the upper PDMS layer, reacted with acid solution; the other was underlying PDMS. The upper layer was called modified layer or stiff layer; the under layer was the bulk of PDMS which still maintained flexibility. We supposed that the differences of thermal-expansion coefficients and the Young's modulus between modified layer and under layer soft PDMS led to a compressive stress. Once the sample underwent a cooling process, the periodic wrinkles were formed owing to the releasing compressive stress. Figure 4.8 revealed the formation mechanism of the periodic wrinkles. As the aforementioned discussion, to modulate the proportion of sulfuric acid in the mixture acid and reaction time, the thickness of the modified layer would be changed and led

into the formation of periodic wrinkles. Therefore, the periodicity was proportional to the proportion of sulfuric acid and immersion time because of the increase of modified layer. Moreover, the acid corrosion resulted in the periodic wrinkle as well as the nanoscale convex with the width less than 100 nm which has not been reported so far. In the acid corrosion experiment, it was hard to find the periodic wrinkle when the sulfuric acid/nitric acid ratio less than 1/1 because of insufficient sulfuric acid to produce effectively modified layer. The wrinkles would be merged when we substantially increased the immersion time more than 2 minutes.

To understand the interaction of PDMS and the acid solution well, we are looking forward to the analysis of chemical group of PDMS before and after the acid treatment. PDMS (Sylgard 184, Dow Corning) we prepared was composed of two intergradients; one was pre-polymer that composed of about 60 repeating units of $-\text{OSi}(\text{CH}_3)_2-$ terminating with a vinyl $-\text{CH}=\text{CH}_2$ group, the other was curing agent that was composed of about 10 repeating units of $-\text{OSi}(\text{CH}_3)_2-$ and silicon hydride $-\text{OSiHCH}_3-$ as shown in Figure 4.9. We investigated the chemical structure of PDMS by FTIR spectra. Table 4.2 listed expected FTIR absorption band of chemical structures of pure PDMS and common groups. The FTIR spectra were shown in Figure 4.7 which indicated the FTIR spectra of pristine and acid-treatment PDMS respectively. The peak of 1260 cm^{-1} resulted from the Si-C chemical bond of $-\text{Si-CH}_3$ functional group; the peak of $1130\text{-}1000\text{ cm}^{-1}$ indicated the Si-O chemical bond of $-\text{Si-O-Si-}$ functional group; the peak of $2280\text{-}2080\text{ cm}^{-1}$ came from Si-H single bond; the peak of $2962\text{-}2960\text{ cm}^{-1}$ resulted from the C-H chemical bond of CH_3 functional group; the broad peak of $3700\text{-}3200\text{ cm}^{-1}$ resulted from the O-H chemical bond of $-\text{OH}$ functional group. In these points, we could conclude that in our system, there had no chemical structure changed when it under the stable stage after acid corrosion. On the other hand, the $-\text{OH}$ resulted from the acid remained or the small

amount of penetration steam. Hence, the wetting phenomenon of superhydrophobicity was resulted from the sculptured topography by acid corrosion instead of chemical modifications of PDMS.

According to our previous study, the anti-wetting property of modified PDMS was caused by the microstructure periodic wrinkles and raised nanostructure. There are two possible wetting states for superhydrophobic PDMS: (1) Wenzel's state: water attaches to the sculptured surface, and (2) Cassie's state: water cannot penetrate to the sculptured surface and trap air inside. As our best knowledge, the high contact angle hysteresis may occur in Wenzel's state; on the contrary, Cassie's state could induce a low contact angle hysteresis such as lotus leaf. Herein, we supposed that the superhydrophobicity of the modified PDMS surface resulted from Cassie's state because the surface had a very small sliding angle (lower than 5°).

Unlike carbon hydride polymer, PDMS consists of silicone base bone which caused a high resistant to environmental damage such as corrosive acid or base solution. This advantage leads into to the potential for application in industrial field. For this reason, we prepared several corrosive solution, ranging from pH = 1 to 14, to examine our modified PDMS. The results showed that the superhydrophobic property (a contact angel of 150°) toward pure water as well as corrosive solution. Moreover, we prepared more corrosive solutions to obtain the results as shown in Figure 4.12. All the corrosive solution located on treated PDMS showed a contact angle higher than 150° .

From the FTIR spectra, no change in chemical structure was revealed. The fabricated PDMS sample just altered the topography on the surface, leading into the two level structures (micro- and nano-structure) as shown above. Hence, we offered another evidence to prove that the superhydrophobic property resulted from the change of topography. Figure 4.13 showed the retention of superhydrophobic

properties over time. If superhydrophobicity caused by the chemical modification, it would decrease as time goes by. For instance, the superhydrophobicity of PDMS treated by SF₆ plasma decayed over time. Our results indicated that the sustained superhydrophobic property owing to the micro- and nano-structures of modified PDMS surface.

4.3.2 High-Water Adhesive Properties of Petal-Like Surfaces

After a raining day, a rose petal is shining because many small water droplets were spread on it even if a wind over blow the petal. Until the last, the unusual phenomena have been studied by scientists. The ability of water adhesion in a rose petal is very different from a lotus leaf in which a water droplet can easily roll off. Because of the two level scales of micro- and nanostructures, the rose petal exhibits a high adhesive force for a water droplet. The topographies of petals are shown in Figure 4.14. The convex structure is about 30 μm in width and the sub-fold is in hundreds of nanometer. From the coevolution opinion, the micro-convex with nano-fold allow bees to grip flowers and increase foraging efficiency.⁵² Herein, we attempted to fabricate a rose petal-like structure by a bottom up method, the results were showed later.

The morphology of rose petal inspired us to fabricate a superhydrophobic surface with high water adhesion. In the beginning, a monolayer of polystyrene (PS) sphere was assembled on a silicon wafer owing to the attractive capillary forces and water flow caused by evaporation.⁵³ Figure 4.15 schemed the formation of the close-packed PS spheres. Subsequently, we manufactured micro-convex by using the close-packed PS spheres as a duplicated mold. In our work, the PDMS replica had the same topography of close-packed PS spheres and then dipped in the prepared solution, the acid solution composed of sulfuric acid and nitric acid. We examined the treated PDMS sample by SEM as shown in Figure 4.16. There were three level structures on

our fabricated surface. The primary structure from the replica of close-packed PS spheres had a convex about 30 μm in width. The secondary structure was the wrinkle of several hundred nanometers in width. It is worthwhile to note that the wrinkle's width on the convex is somewhat smaller than that on plane PDMS. Compared with a plane, a spherical surface tends to release the external stress, which causes the smaller periodicity. The tertiary structure was the small bulges with the width less than 100 nm.

Figure 4.18 were the images of a water droplet on PDMS surface, encompassed three structures. To investigate the wetting phenomena, we prepared plane and convex PDMS to compare with the petal-like PDMS. Surface roughness magnifies the underlying properties; both hydrophobic and water adhesive characteristics are reinforced by surface textures based on the wetting property of Wenzel's state.¹⁸ Because of the insufficient roughness, the formation of air pockets is impossible on plane and convex PDMS. Thus, when a water droplet deposits on the flat PDMS or that on the convex one, the wetting state will obey Wenzel's model. Petal-like PDMS was unlike plane or convex PDMS; it had sufficient roughness for formation of air pockets underneath the water droplet. There, consequently, were two possible wetting states for our petal-like PDMS. One was Cassie's state that we have mentioned earlier, the other was Cassie impregnating state, in which, grooves of the solid are wetted with liquid and solid plateaus are dry.⁵⁴ The petal-like PDMS exhibited the high adhesion for water so the wetting state tended to the Cassie impregnating state instead of the Cassie's state. In the Cassie impregnating model, the water film can impregnate along with the topography; nevertheless, the water film even can wet the upper part of the surface, the bottom still dried. For water, the close-packed microscale convex was easy to penetrate, but the nanoscale structures could repel the water. Herein, a droplet of water placed on our fabricated PDMS spread on the surface and penetrated the

depth of the support. The scheme was shown in Figure 4.19.

In this section, we displayed the adhesive properties toward flat, convex, and petal-like PDMS. Moreover, we also showed the relationship between dipping times and adhesive forces. Figure 4.20 indicated that the adhesive forces and water contact angles received with different structures. With roughness increasing, the contact angles changed from 93.4° to 128.7° and 150.1° . A water droplet located on plane and convex PDMS was revealed the Wenzel's wetting state because the two topographies had insufficient roughness to trapped air under the water. The different of contact angle between plane and convex PDMS owing to the surface roughness. On the other hand, air pockets could be obtained when a water droplet deposited on the petal-like PDMS. It's because of the formation of wrinkles and nanostructures after the acid treatment; the more air trapped, the more increase of water contact angle. The adhesive forces increased from 11.4 N/m^2 , 14.5 N/m^2 to 35.8 N/m^2 , while the adhesive forces of plane and convex PDMS were due to the van der Waals interactions between the liquid and solid supports. A theatrical adhesive force obtained from petal-like PDMS was caused by van der Waals interaction and capillary force. As earlier study, the wetting state of petal-like PDMS is Cassie impregnating state; the water, hence, can penetrate to the grooves and the upper wrinkles. The extended contact area between the liquid and the solid support caused the larger van der Waals interaction than plane and convex PDMS. Besides, the trapped air induced a large capillary force when the water droplet was going to pull out from the surface. According to the reasons above, the petal-like PDMS revealed a high adhesion for water. To investigate the induced adhesive forces from wrinkles and nanostructures, we measured the adhesive forces and contact angles of petal-like PDMS treated by several circumstances of dipping times. As showed in Figure 4.21, the dipping times from 3 to 4 and 5 caused the increases both adhesive forces and water contact angles.

The water contact angles increased from 137.9°, 148.8° to 150.1° with dipping times increased from 3, 4 to 5, respectively. The three times dipping might induce slight wrinkles and nanostructures which could not increase sufficient roughness for trapping much air under the liquid; it, hence, showed the smallest contact angle and adhesive force. Under the dipping conditions of 4 and 5, the change of water contact angles and adhesive forces were small, less than 1% and 3%, respectively. The reasonable explanations of the increases were as follows. The longer acid treatment with time caused deeper wrinkles and more nanostructures which induced more contact area and much air trapping under the liquid, the van der Waals interaction and capillary force were both increasing. These increases caused high water adhesion. However, too much acid treatment time, we could not obtain petal-like PDMS because the formed wrinkles would be destroyed with the excess acid corrosion.

4.3.3 Innovative Applications of Petal-Like Surfaces

Petal-like PDMS also could be applied as a transferring tool of a water droplet with some weight, which was suggested to be useful in liquid transportation without any loss or contamination for microsample analysis. We deposited a 5 mg water droplet on the superhydrophobic surface. When petal-like PDMS contacts the water droplet, it immediately adhered to the petal-like PDMS. The water droplet was then transferred from the petal-like surface to a hydrophilic silicon wafer as shown in Figure 4.22. It's simple and easy to release the water droplet from petal-like PDMS to a hydrophilic silicon wafer. As mentioned previously, hairy type and tube type surfaces also have a high adhesion to water. However, excessive adhesion resulted from strong van der Waals force is disadvantageous to water-releasing, and thereby such structures are unsuitable for liquid transportation. As the results we obtained, the petal-like PDMS had the potential of water transportation; moreover, it might be used in micro-fluid field.

To fabricate the nonresidual PDMS stamp, we designed the two superhydrophobic regions on the PDMS. One is the superhydrophobic area with self-cleaning and the other is the superhydrophobic area with high water adhesion. The convex PDMS sample was manufactured by duplicating the close-packed PS beads. Afterward, the convex PDMS sample was etched by a carbon dioxide laser. The remained region still had convex upon PDMS; on the other hand, the topography of the etching area became flat. The prepared PDMS sample, then, treated by acid corrosion process we have mentioned above (Figure 4.23a). Here, the resulting PDMS had two wetting states, Cassie impregnating wetting state and Cassie's wetting state. The petal-like area was engaged in an adhesive palm to adsorb the dye then released it readily to a paper. By contrast, the flat region in Cassie's wetting state exhibited non-sticky property, which avoided the absorption of the dye. After we used PDMS to imprint for several thousand times, the surface of the stamp remained in clean as well (Figure 4.23c). This nonresidual property means we need fewer dye and cleanless process in imprinting, which brings advancements of low cost and environmental friend.

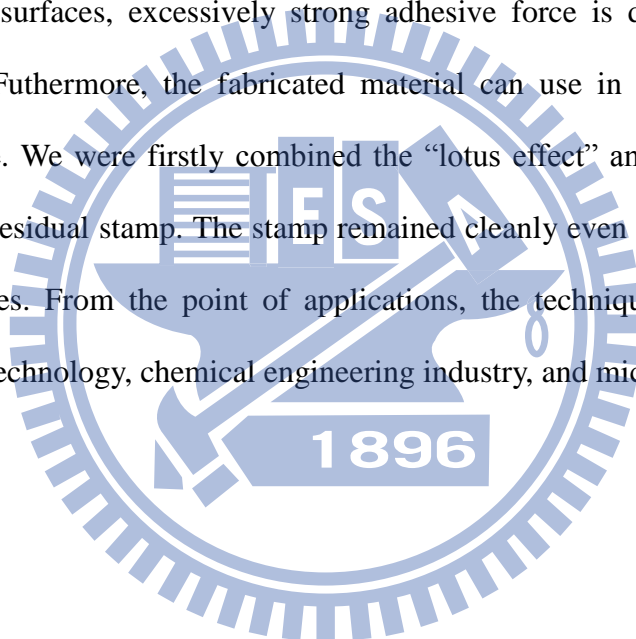
4.4 Summary

Plane PDMS treated by the simple acid texture exhibited regular periodic wrinkles whose periodicities were in a micro-scale. Two superhydrophobic surfaces with self-cleaning and high water adhesion were obtained. The resulting superhydrophobicity caused only by the topography changing instead of chemical modification. Owing to the silicon back bone in PDMS, the fabricated surface displayed mechanical stable superhydrophobicity under acidic and basic corrosive environments and a long duration.

The complicated rose petal topography manufactured by duplicating the

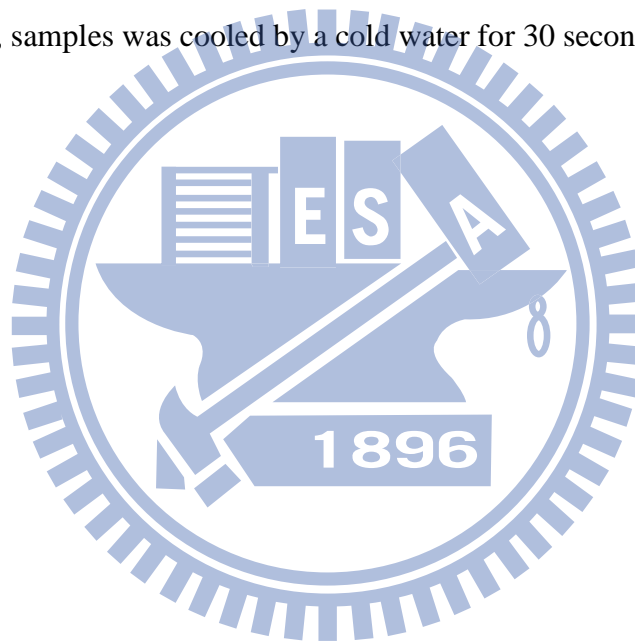
close-packed polystyrene beads and acid corrosion process. The petal-like surface of superhydrophobicity and high adhesive force for water we fabricated had three structural levels including micro-convexes, nano-wrinkles and nanostructures. The resulting micro-convex, provided high-water adhesive ability due to van der Waals interaction, while nano-wrinkles and nanostructures provided superhydrophobicity caused by the lotus effect.

The unique property including superhydrophobicity and high-water adhesion was suitable for applying in liquid transportation. Unlike hairy type and tube type superhydrophobic surfaces, excessively strong adhesive force is disadvantageous to water-releasing. Furthermore, the fabricated material can use in future nonresidual imprint technique. We were firstly combined the “lotus effect” and “petal effect” to fabricate the nonresidual stamp. The stamp remained cleanly even though it was used for thousand times. From the point of applications, the technique we proposed is applicable in biotechnology, chemical engineering industry, and microfluidic devices.



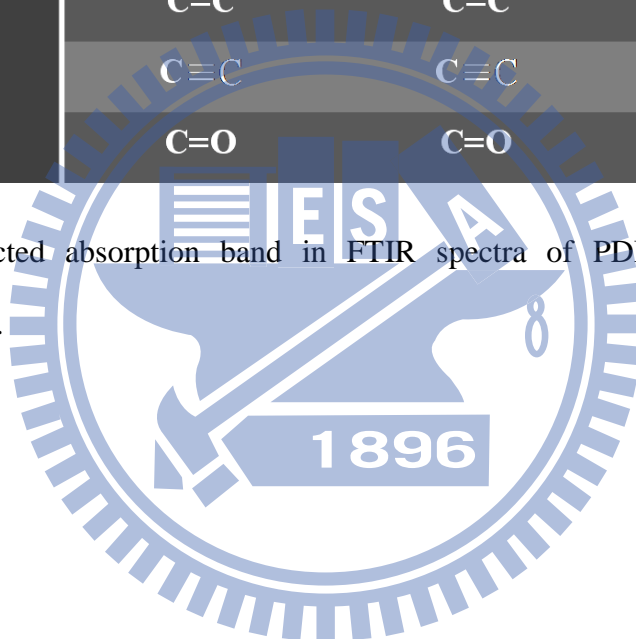
time \ ratio	S/N = 1/1	S/N = 2/1
5 s	#1	#5
15 s	#2	#6
30 s	#3	#7
60 s	#4	#8

Table 4.1 The treatment conditions were listed above, in which, S/N presented the volume ratio of sulfuric acid over nitric acid, #1~#8 represented serious samples' numbers, first column indicated the reaction time, all the samples reaction at 55°C; after acid etching, samples was cooled by a cold water for 30 seconds at 1°C.



	Functional group	Chemical bond	Expected peak (cm ⁻¹)
PDMS	-Si-CH ₃	Si-C	1260
	-Si-O-Si	Si-O	1130-1000
	-Si-H	Si-H	2280-2080
	-CH ₃	C-H	2962-2960
Other	-OH	O-H	3650-3000
	-N-H	N-H	3650-3000
	C=C	C=C	1680-1600
	C≡C	C≡C	2400-1900
	C=O	C=O	1800-1650

Table 4.2 Expected absorption band in FTIR spectra of PDMS and common functional groups.






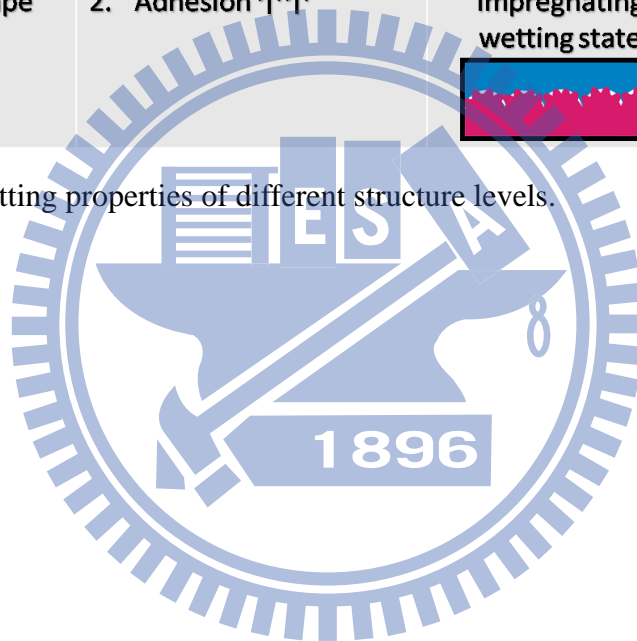
	Structure	Property	Wetting state	Reason
PDMS	Flat	Hydrophobicity	Wenzel state	Van der Waals interaction
	Periodic wrinkles	1. Superhydrophobicity 2. Self-clean	Cassie state 	Lotus effect
	Convex shape	1. Hydrophobicity ↑ 2. Adhesion ↑	Wenzel state 	Van der Waals interaction
	Petal-like shape	1. Superhydrophobicity 2. Adhesion ↑↑	Cassie impregnating wetting state 	Petal effect

Table 4.3 The wetting properties of different structure levels.



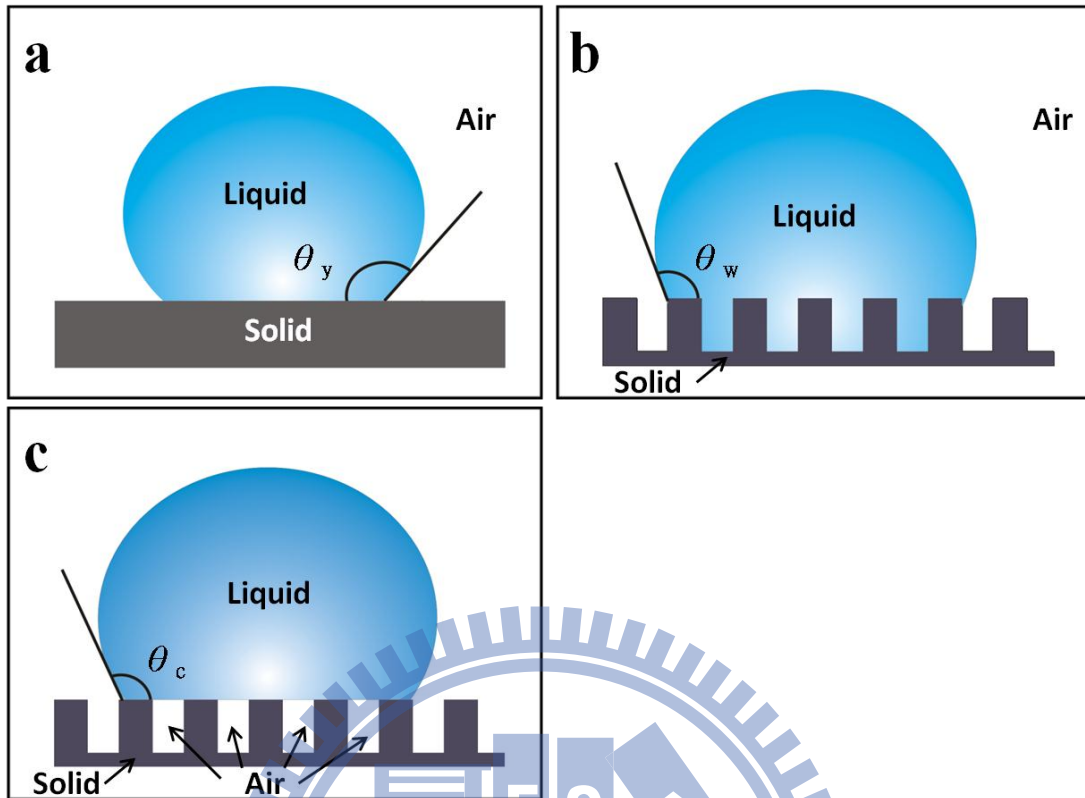


Figure 4.1 A liquid droplet in contact with (a) a smooth solid surface (b), (c) a rough solid surface. (b) Illustrate Wenzel's wetting state. (c) Illustrate Cassie's wetting state.

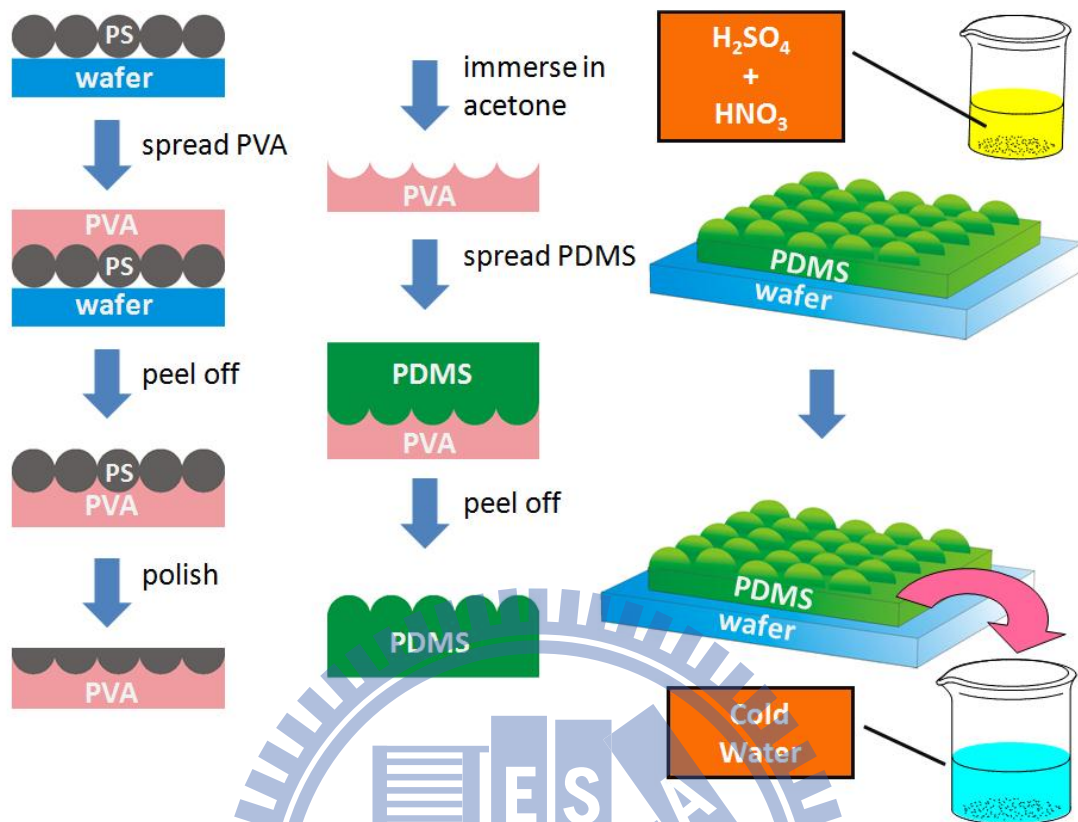


Figure 4.2 The scheme showed the protocol of manufacturing a petal-like PDMS.

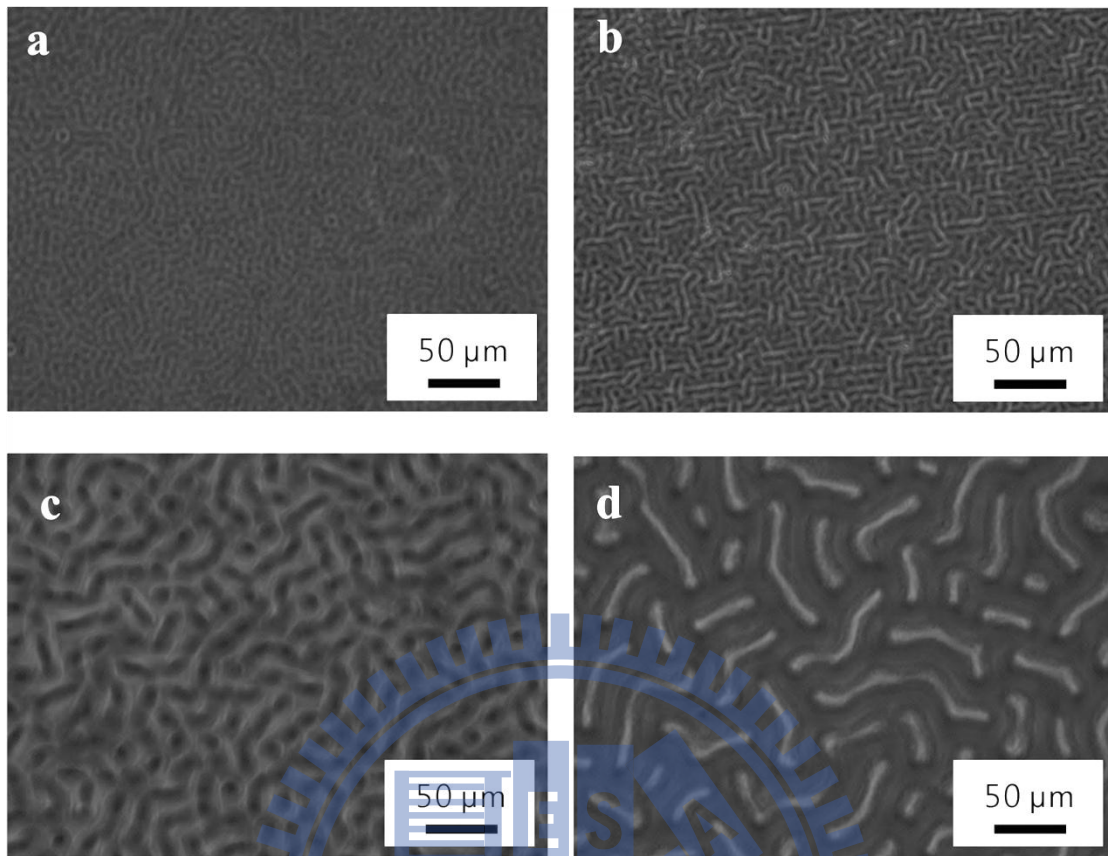


Figure 4.3 Optical microscopy images of PDMS through acid treatment. The acid solution was a mixture of sulfuric acid and nitric acid in the volume ratio of 1/1, etching with different treatment times of (a) 5 s, (b) 15 s, (c) 30 s, and (d) 60 s.

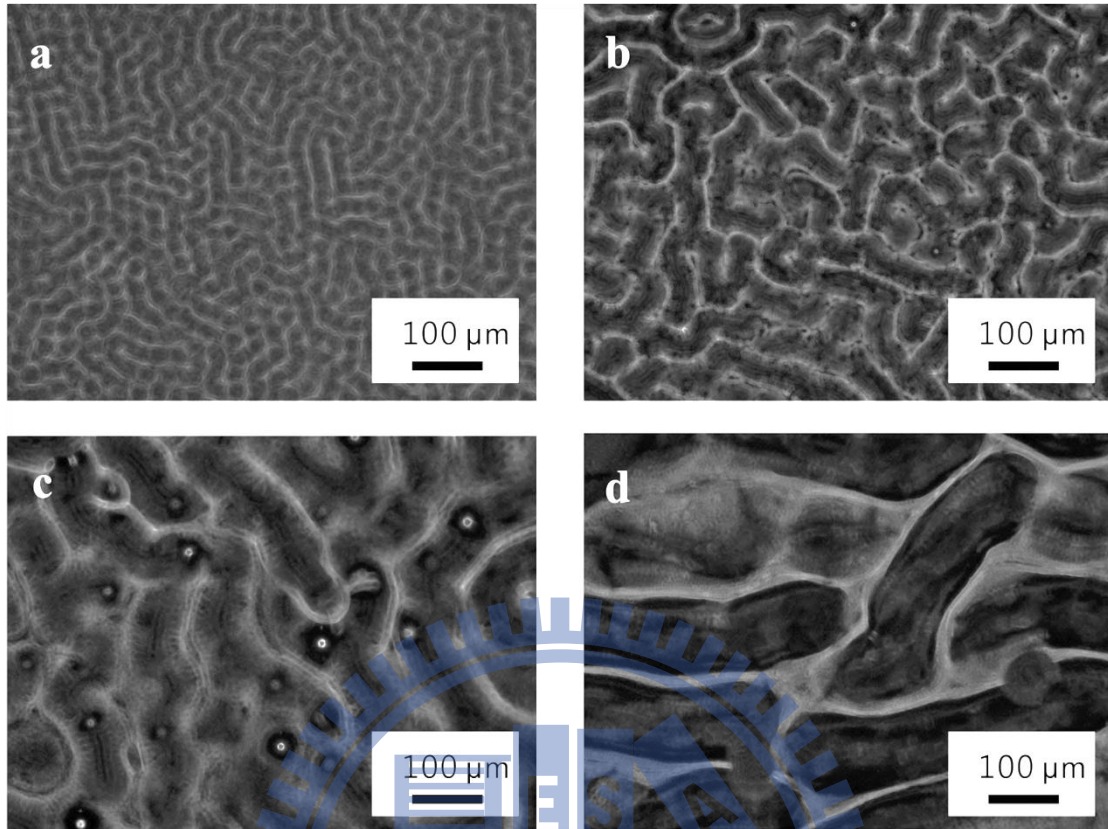


Figure 4.4 Optical microscopy images of PDMS through acid treatment. The acid solution was a mixture of sulfuric acid and nitric acid in the volume ratio of 2/1, etching with different treatment times of (a) 5 s, (b) 15 s, (c) 30 s, and (d) 60 s.

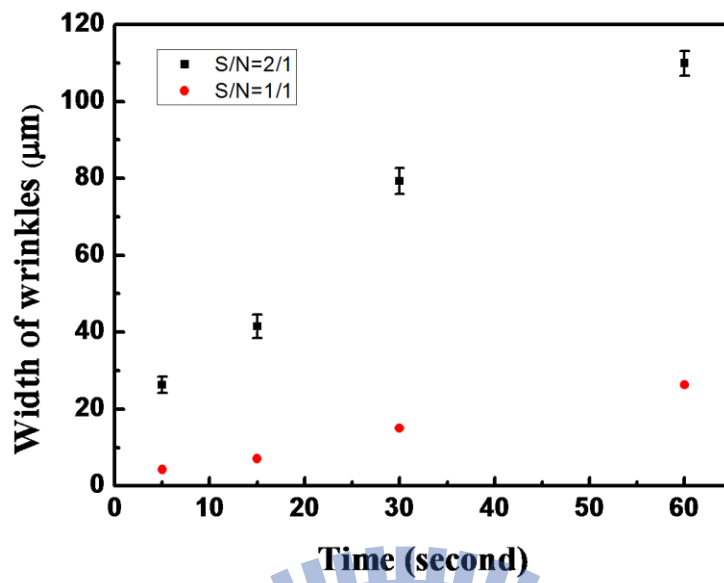
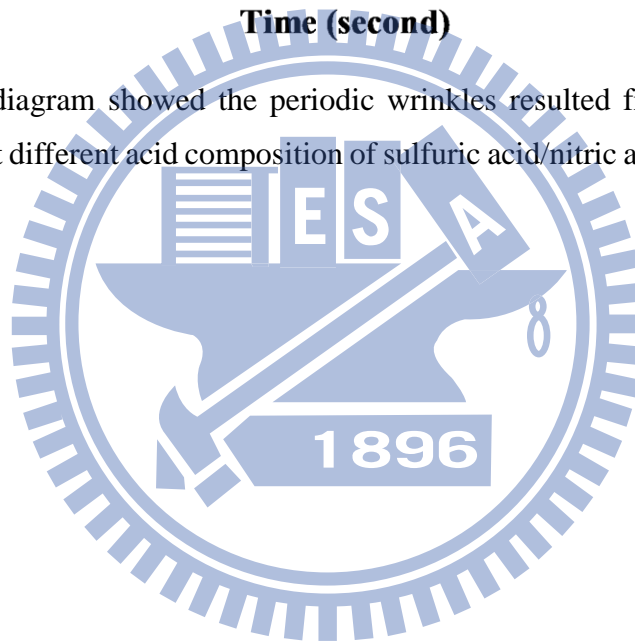


Figure 4.5 The diagram showed the periodic wrinkles resulted from the increasing immersion time at different acid composition of sulfuric acid/nitric acid = 1/1 and 2/1 in volume ratio.



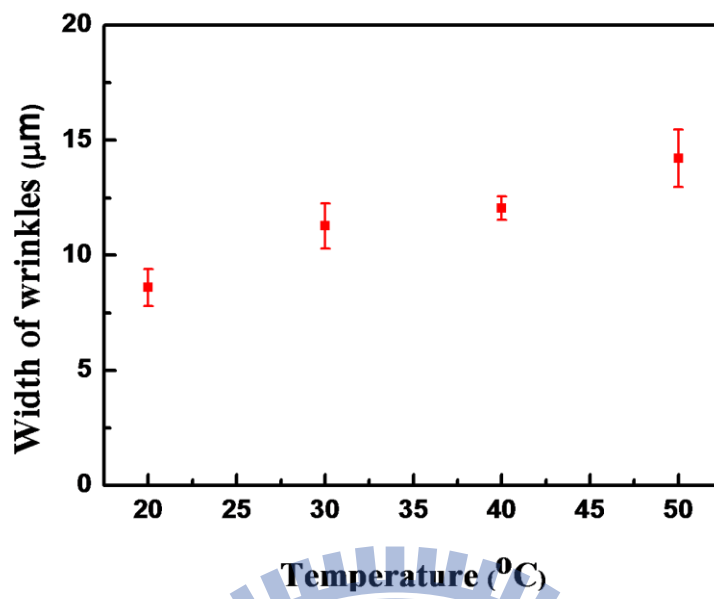
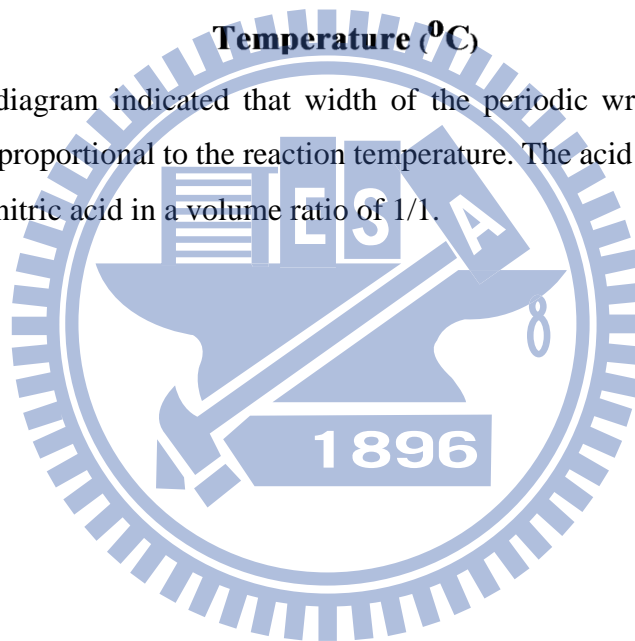


Figure 4.6 The diagram indicated that width of the periodic wrinkles at the same etching time was proportional to the reaction temperature. The acid was composed of sulfuric acid and nitric acid in a volume ratio of 1/1.



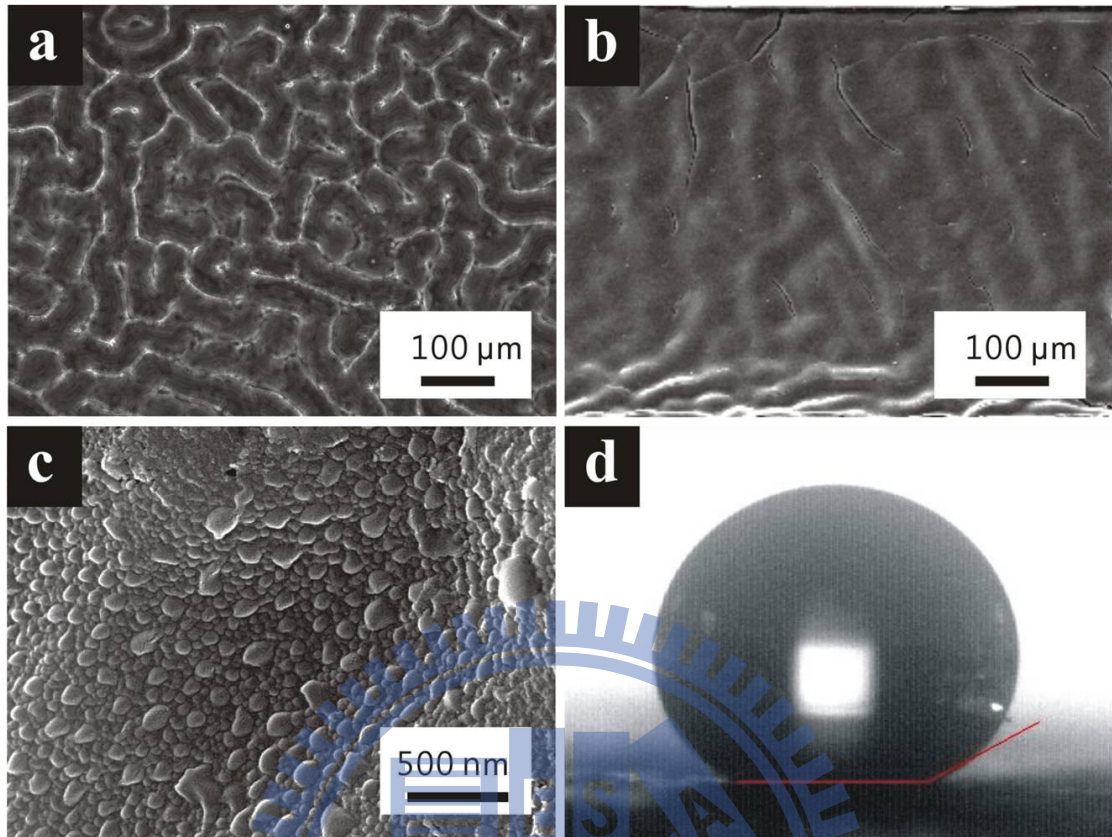


Figure 4.7 Plane PDMS treated with acid producing a superhydrophobic surface. (a) Optical microscope image of periodic wrinkles PDMS caused by acid corrosion. (b), (c) SEM images showing micro- and nano-structures on the sample respectively. (d) A 5 mg water droplet located on the superhydrophobic PDMS surface, showing a contact angle of 151.5° .

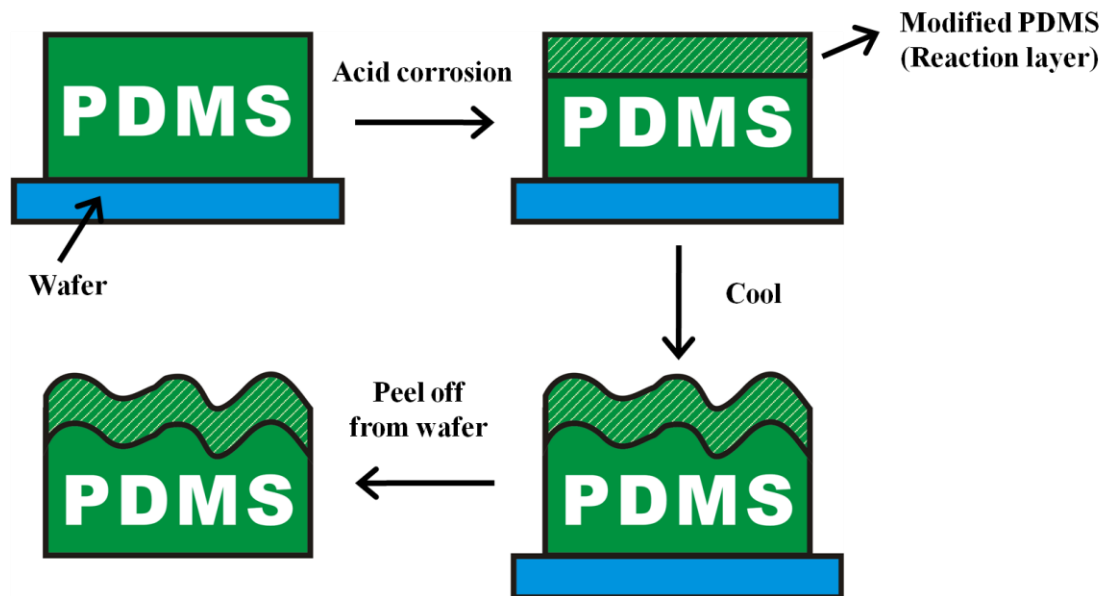
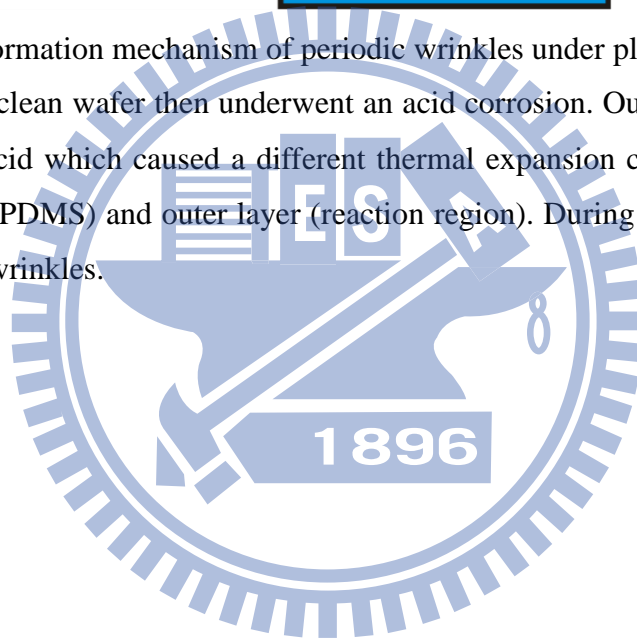


Figure 4.8 The formation mechanism of periodic wrinkles under plane PDMS. PDMS was fixed onto a clean wafer then underwent an acid corrosion. Outer layer of PDMS was reacted by acid which caused a different thermal expansion coefficient between inner layer (bulk PDMS) and outer layer (reaction region). During cooling process, it formed periodic wrinkles.



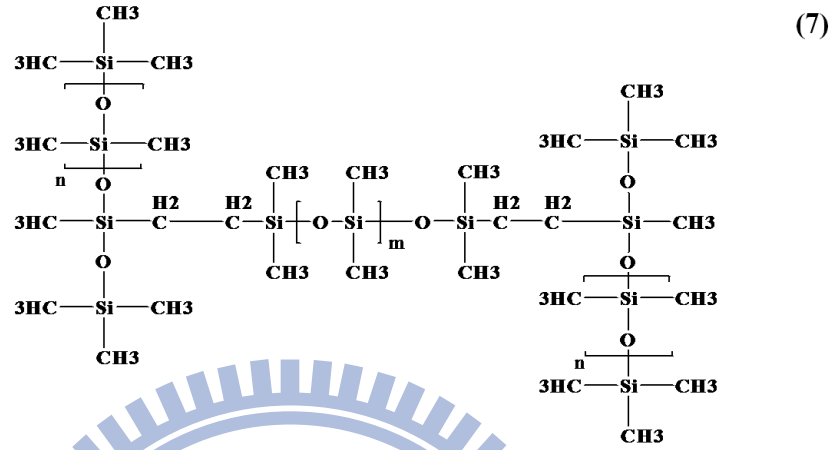
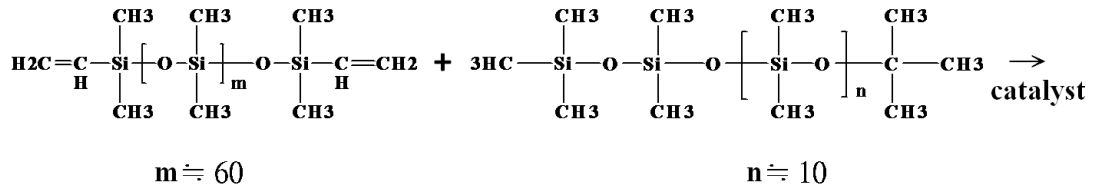
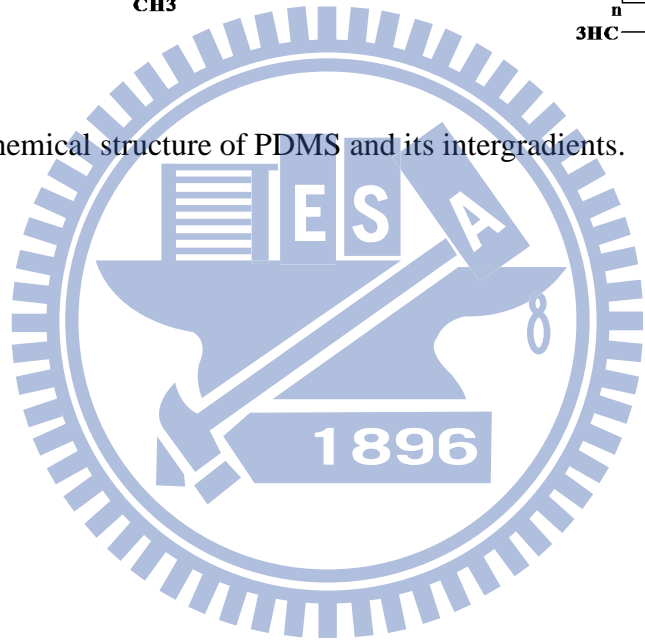


Figure 4.9 The chemical structure of PDMS and its intergradients.



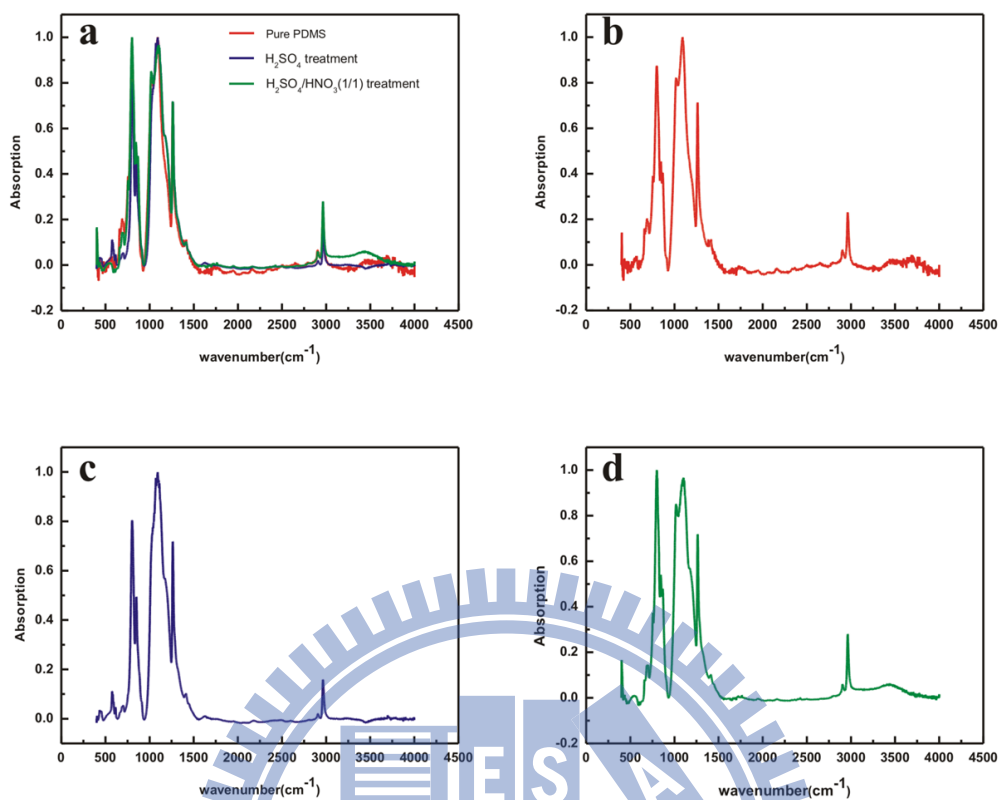


Figure 4.10 (a) The FTIR spectra of PDMS for different treatments. (b) No treatment. (c) Treated by pure sulfuric acid. (d) Treated by mixture acid, sulfuric acid/nitric acid = 1/1 in volume ratio.



Figure 4.11 (a)-(n) Images showed the contact angle changed from different condition solution, pH values changed from 1-14. The superhydrophobic property of the treated PDMS surface maintained as similar as the pure water. A high contact angle around 150° was revealed during the wide range of pH values.

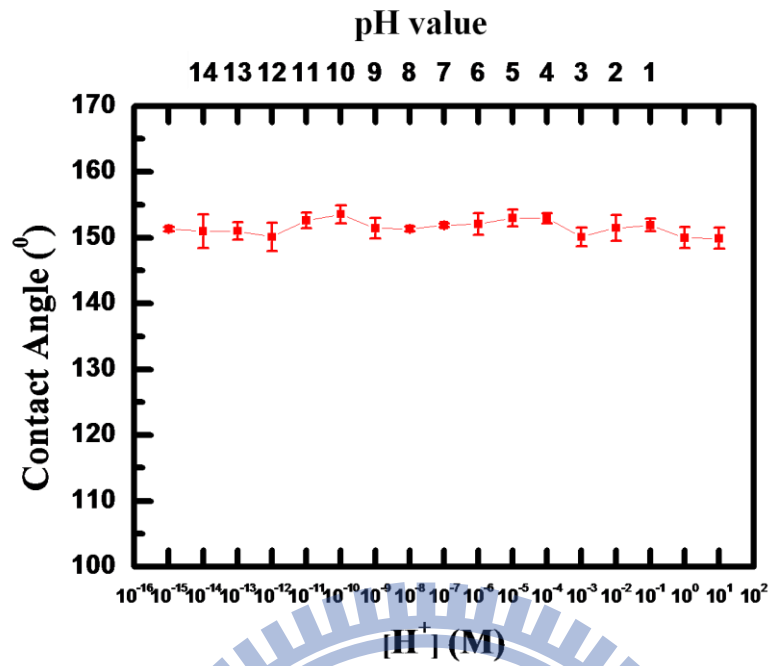
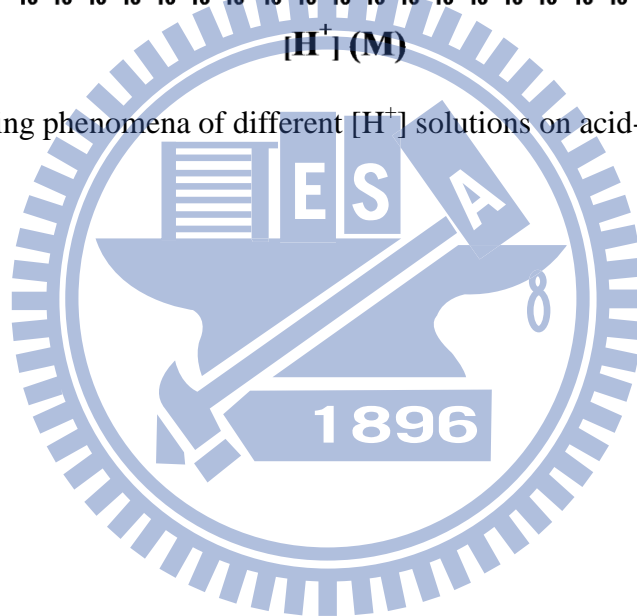


Figure 4.12 Wetting phenomena of different [H⁺] solutions on acid-treated PDMS.



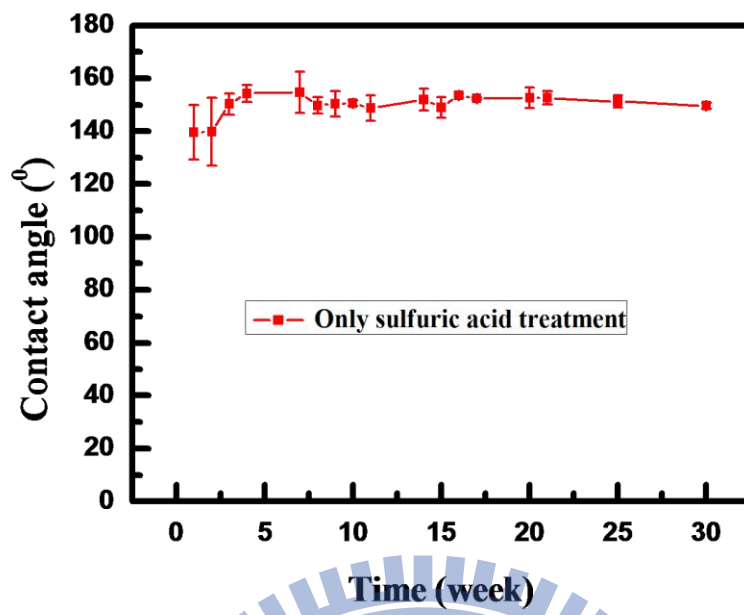
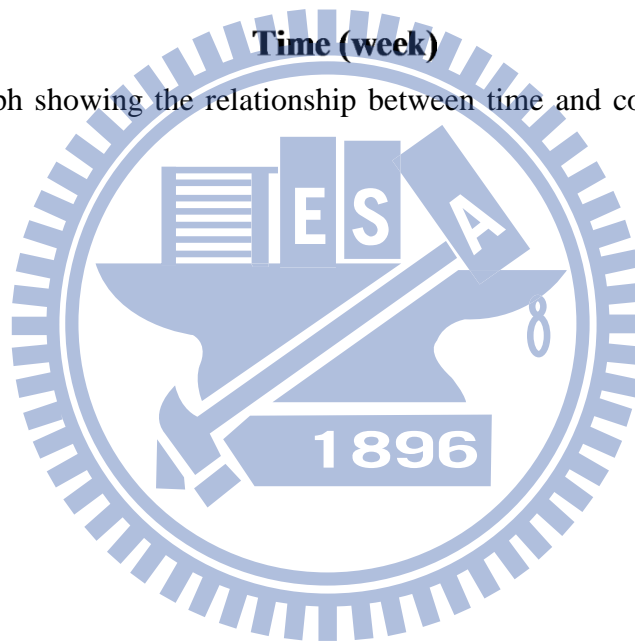


Figure 4.13 Graph showing the relationship between time and contact angle on the treated PDMS.



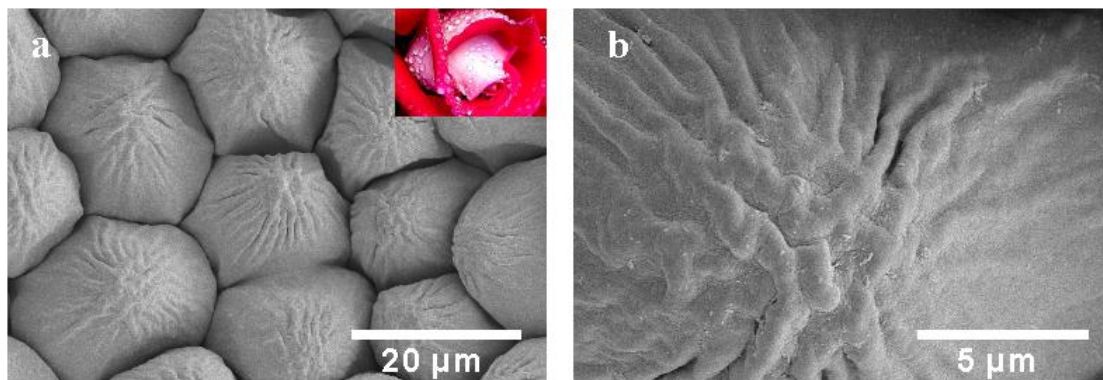


Figure 4.14 The SEM images of dehydrated rose petals. (a) The surface showed the large-scaled convex about 20~30 μm in width (b) The surface showed the sub-fold of approximately 800 nm in width.



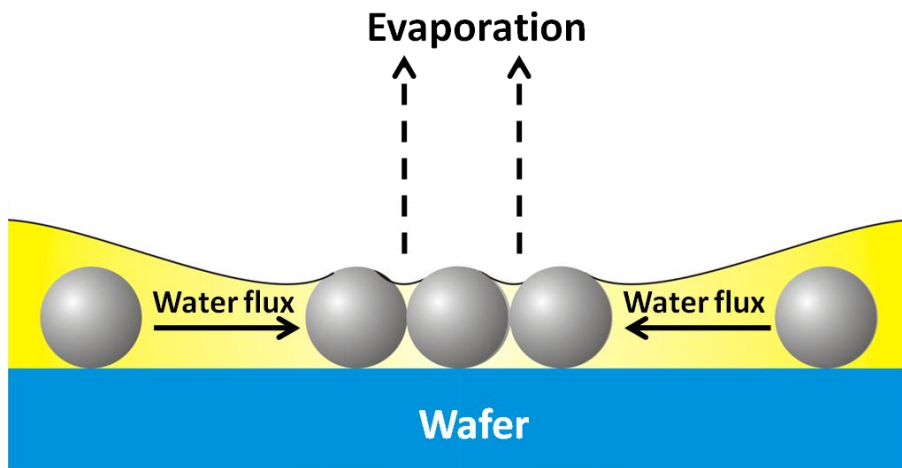
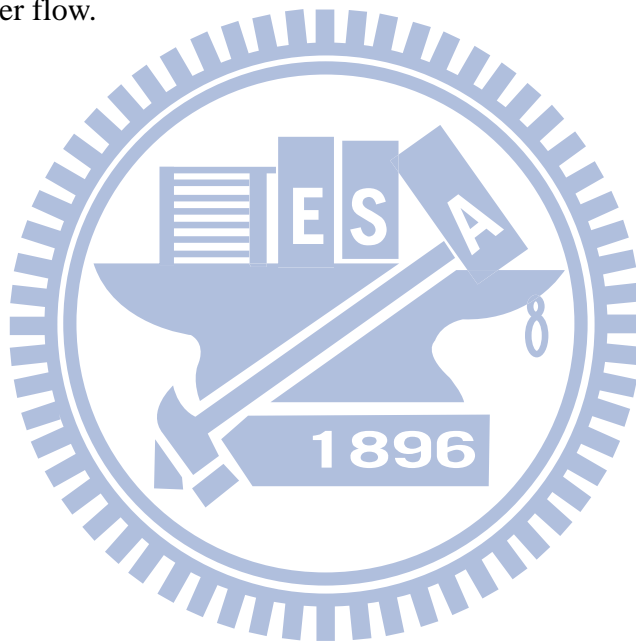


Figure 4.15 Scheme showed the formation of PS spheres assembled on a silicon wafer caused by the water flow.



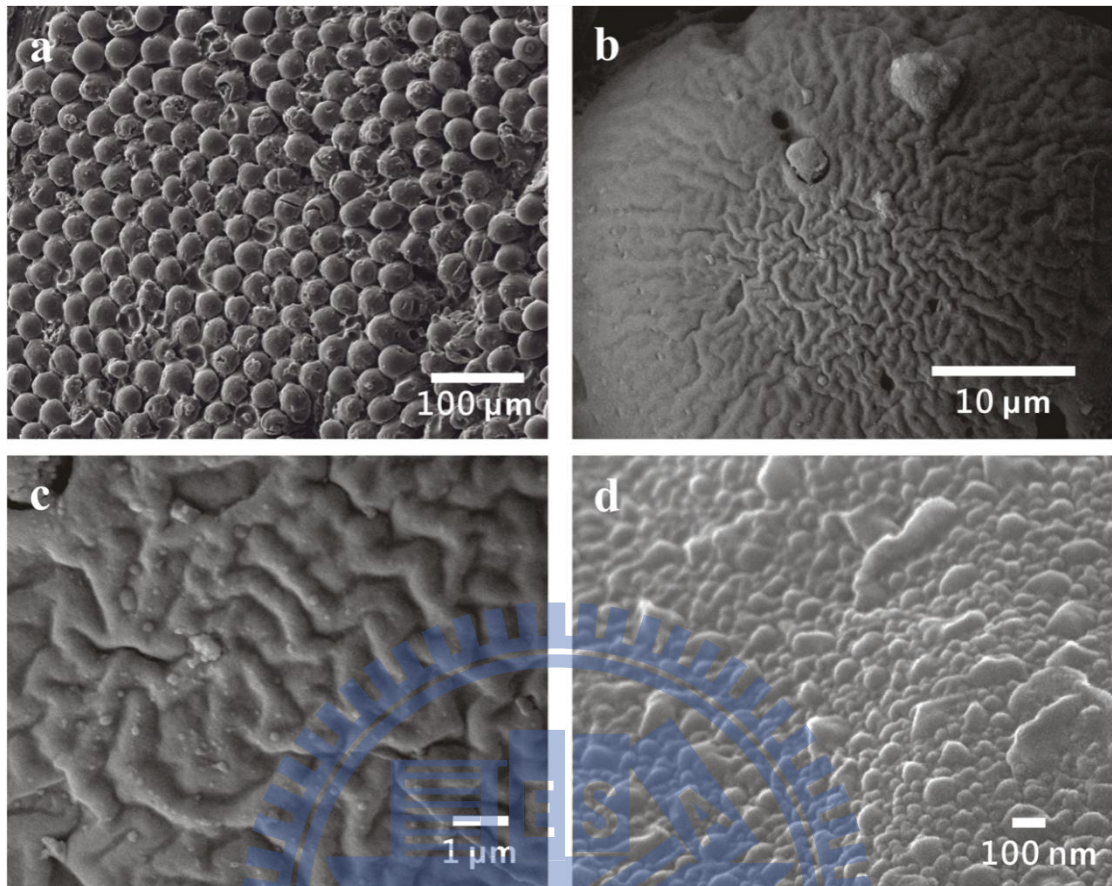


Figure 4.16 (a) The SEM image show the close-packed convex. (b), (c) Showing SEM images for the manufactured surface with the topography which was similar to the rose-petal (d) SEM image indicated the nanostructure of the surface.

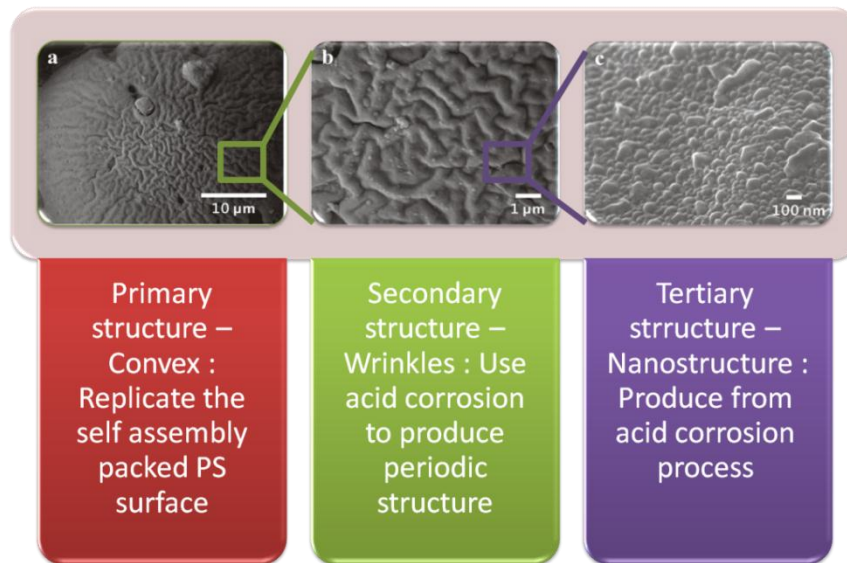
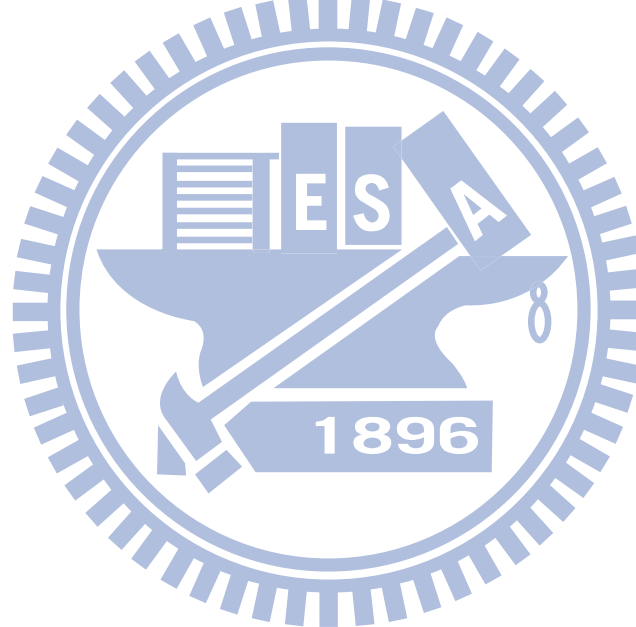


Figure 4.17 Scheme of the three level structures on PDMS.



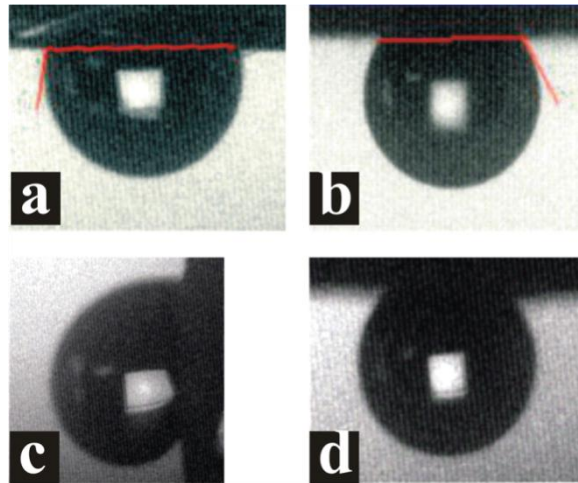


Figure 4.18 A 5 mg water droplet pinned on (a) a flat PDMS surface, (b) a PDMS with micro-scaled convex, and (c), (d) a PDMS surface with petal-like morphology when turning the surface vertically (90°) and upside (180°) respectively.

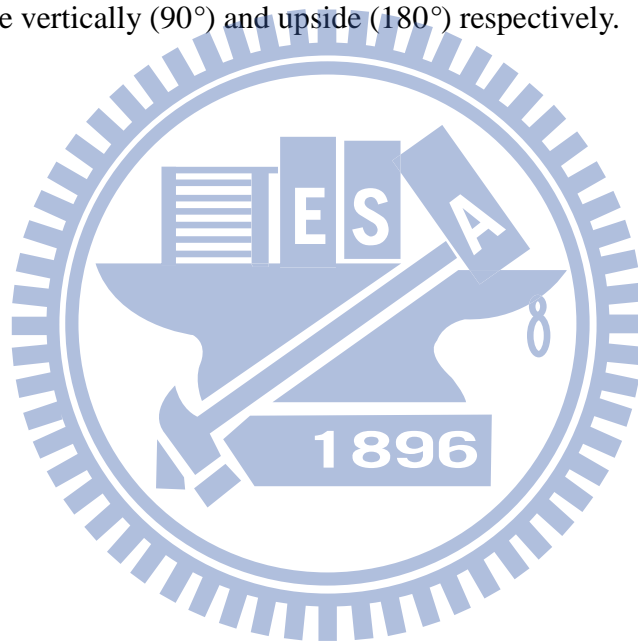
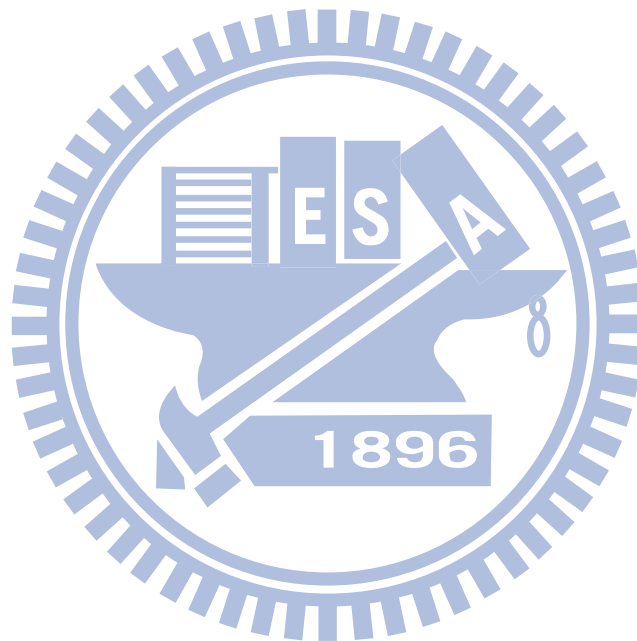




Figure 4.19 Water penetrate the microscale convex and partial wetting the upper part of nanoscale wrinkles.



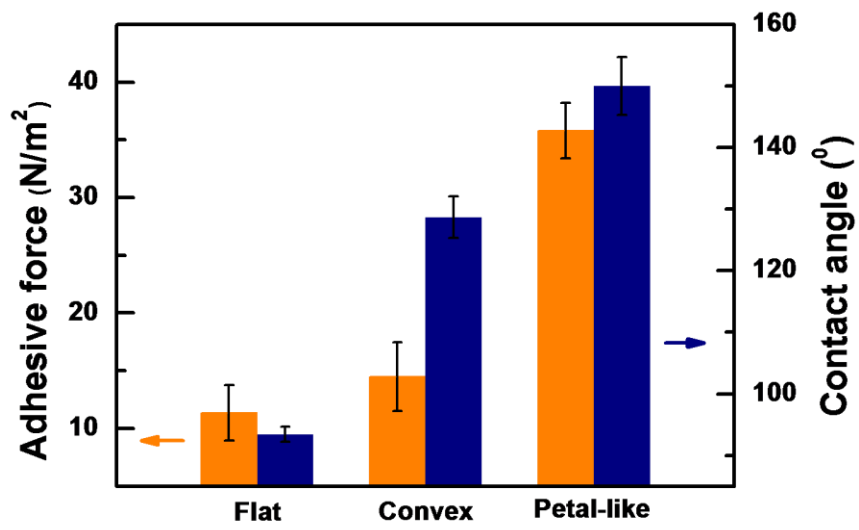


Figure 4.20 The graph of water contact angles and adhesive force between different morphology, flat, micro-scaled convex and petal-like topography.



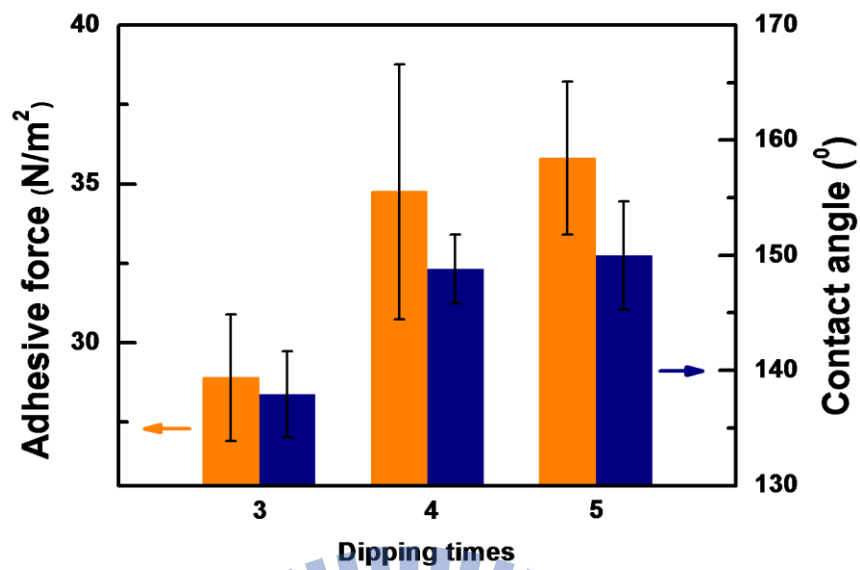


Figure 4.21 The histogram of water contact angles and adhesive forces on the petal-like surface changed with decanting times. Blue rectangles indicated that adhesive force increased from 28.9 N/m² to 35.8 N/m². Orange rectangles showed the contact angle changed from 137.9° to 150.1°.



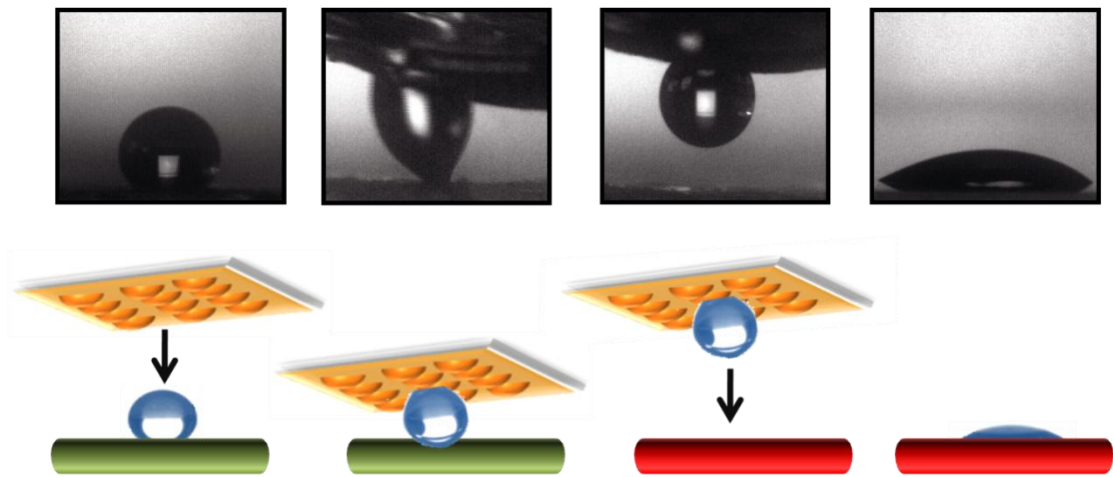


Figure 4.22 A 5 mg water droplet transported from a hydrophobic and non-sticky surface to a hydrophilic surface by the petal-like surface PDMS.



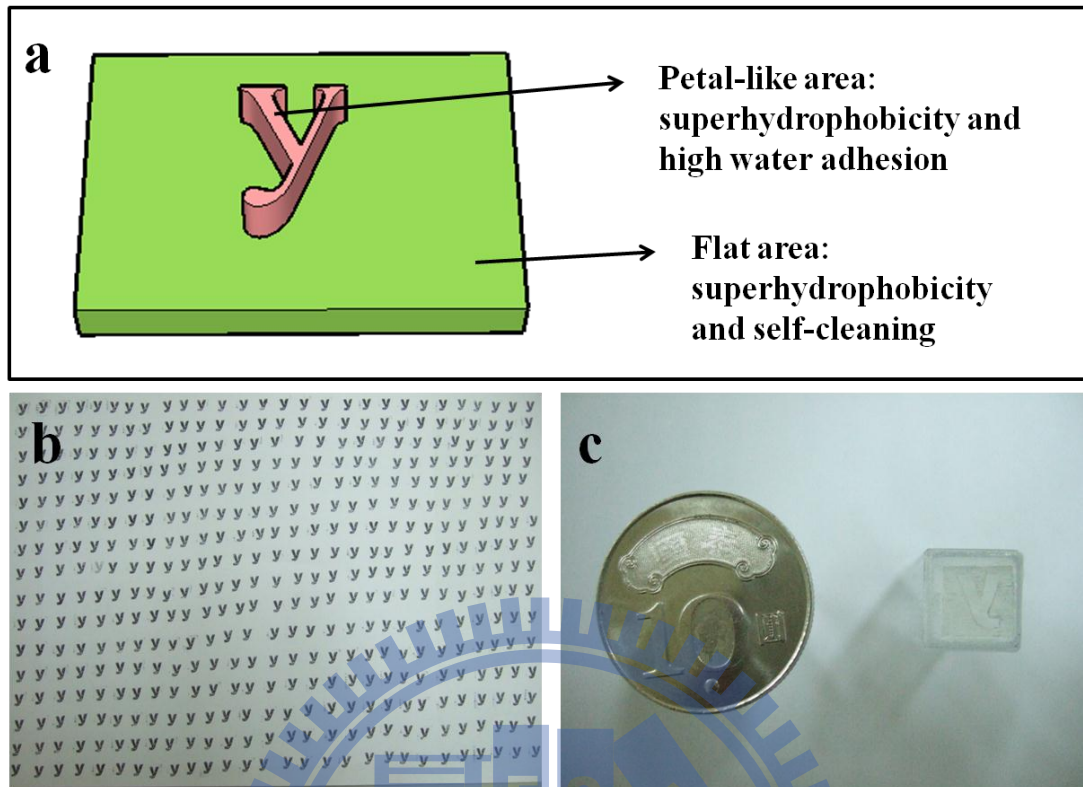


Figure 4.23 (a) Scheme indicated the two different superhydrophobic surfaces on the PDMS. (b) Several hundreds of patterns on the paper by using the fabricated PDMS stamp continuously. (c) The image showed the PDMS stamp remained cleaning after imprinting upon a paper with the stamp for several hundred times.

Chapter 5: Conclusions

We have investigated tantalum nanodot and nanocones arrays through the fundamental research. Artificial Moth-eye structures by using hollow-to-solid nanocones were successfully fabricated for high-performance AR coatings. Quasi-closely packed arrays of cone-like nanostructures are fabricated by the anodization of Al/Ta bilayers coated on substrates. We proposed the mechanism of formation of the hollow NCA due to the stress of gaseous O_2 . The porosity of the hollow nanostructures is calculatedly controlled by varying the deposited thickness of Ta film. The transmissions of the glass substrates coated with hollow NCA of 65.5% porosity reached greater than 97.8% over the whole visible range. Besides, the reflectivity was suppressed greatly in a broadband omnidirection and reached as low as 10% at an incident angle of 70° . In other cases of porosity, NCA coatings were also found as an efficient ARS on sapphire and AlN substrates. Good mechanical stability makes NCA suitable for protective coatings for optical transparency. The availability of the hollow nanostructures has allowed the design of artificial optical properties as new building blocks (e. g. diffractive layer, diffusers, or reflectors) in future photonic devices.

Moreover, we also have fabricated hollow TiO_2 nanocones under PAA featuring TiO_2 NTs within directly on FTO glass and used them as new working electrodes in DSSCs. By depositing a thin layer (15-nm-thick) of Ti on a FTO substrate prior to anodization, we obtained self-organized hollow TiO_2 nanocones, with improved contact between the FTO substrate and the overlaying Al, thereby solving the problems of delamination of an undesirable barrier. This more-stable PAA/FTO structure was highly suitable for use in subsequent sol-gel processing of $Ti(OiPr)_4$.

The novel structure combines two types of TiO₂ materials—0-D nanocones and 1-D NTs—to benefits from a large contact area, direct electron transport path, and slow recombination of electrons. The unique morphology provided a photocurrent of 5.15 mA/cm², an open circuit voltage of 0.64 V, and an IPCE peak of 26% from an 800-nm-thick NT array. The relatively short NT array results in a considerably lower photoabsorption than, for example, the current DSSC “gold standard” featuring a tens-of-micrometers-thick layer of TiO₂ NTs. We suspect that increasing the length of the NT array on the electrode might allow us to further improve the efficiencies of such DSSCs. The facile synthesis of this novel architecture may allow the design of new nanostructures for use as new building blocks in future electro-optical devices.

We successfully presented an approach to fabricate angled taper nanohair arrays as an excellent directional, reusable and water cleanable gecko-mimicking dry adhesive in large area. From Dahlquist’s criterion, an ideal taper nanohair of PUA that consist a length of 1.3 μm and a diameter of 380 nm was designed. By using taper PAA mold via decoupling two-step HA process reported firstly by us, taper nanohairs with slanted angle were fabricated. The angled taper nanohair did facilitate the stability and self-cleaning properties compared with pillar nanohairs while still maintain a great directional adhesion. Moreover, remarkably directional force exhibited by angled taper nanohair arrays is showing here with strong shear attachment (~8 N/cm²) in the gripping direction and easy releasing(~1.4 N/cm²) in the reverse direction (pulled against the angled direction of hairs). The smart adhesive presented here would enable the climbing robots, cleaning transport system such as LCD factory and non-residue sticker for future generation. A further study should be done on longer length or stiffer material to improve the adhesion capability against rough surfaces outside the laboratory.

Plane PDMS treated by the simple acid texture exhibited regular periodic

wrinkles whose periodicities were in a micro-scale. Two superhydrophobic surfaces with self-cleaning and high water adhesion were obtained. The resulting superhydrophobicity caused only by the topography changing instead of chemical modification. Owing to the silicon back bone in PDMS, the fabricated surface displayed mechanical stable superhydrophobicity under acidic and basic corrosive environments and a long duration. The complicated rose petal topography manufactured by duplicating the close-packed polystyrene beads and acid corrosion process. The petal-like surface of superhydrophobicity and high adhesive force for water we fabricated had three structural levels including micro-convexes, nano-wrinkles and nanostructures. The resulting micro-convex, provided high-water adhesive ability due to van der Waals interaction, while nano-wrinkles and nanostructures provided superhydrophobicity caused by the lotus effect. The unique property including superhydrophobicity and high-water adhesion was suitable for applying in liquid transportation. Unlike hairy type and tube type superhydrophobic surfaces, excessively strong adhesive force is disadvantageous to water-releasing. Furthermore, the fabricated material can use in future nonresidual imprint technique. We were firstly combined the “lotus effect” and “petal effect” to fabricate the nonresidual stamp. The stamp remained cleanly even though it was used for thousand times. From the point of applications, the technique we proposed is applicable in biotechnology, chemical engineering industry, and microfluidic devices.

Reference

Chapter 2

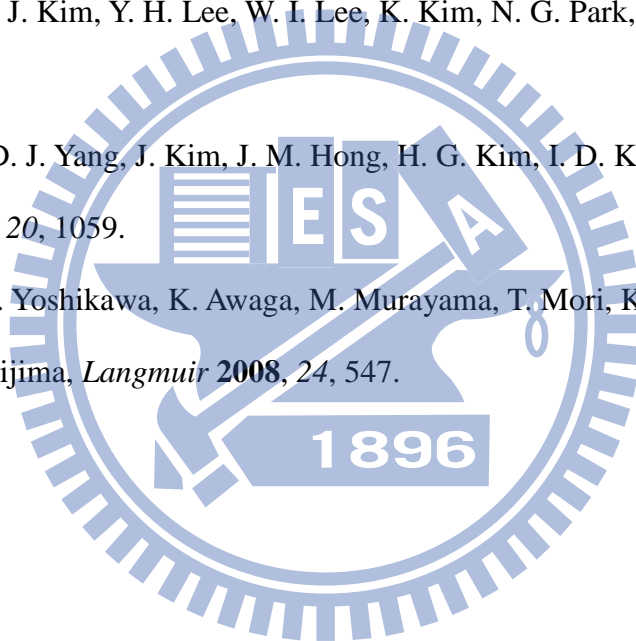
- [1] H. Masuda, K. Fukuda, *Science* **1995**, 268, 1466.
- [2] J. P. O'Sullivan, G. C. Wood, *Proc. R. Soc. London, Ser.* **1970**, 317, 511.
- [3] H. Masuda, F. Hasegawa, S. Ono, *J. Electrochem. Soc.* **1997**, 144, L127.
- [4] D. Crouse, Y. H. Lo, A. E. Miller, M. Crouse, *Appl. Phys. Lett.* **2000**, 76, 49.
- [5] S. Shingubara, O. Okino, Y. Murakami, H. Sakaue, T. Takahagi, *J. Vac. Sci. Technol.* **2001**, B19, 1901.
- [6] T. Iwasaki, T. Motoi, T. Den, *Appl. Phys. Lett.* **1999**, 75, 2044.
- [7] S. H. Jeong, H. Y. Hwang, K. H. Lee, Y. Jeong, *Appl. Phys. Lett.* **2001**, 78, 2052.
- [8] W. Hu, D. Gong, Z. Chen, L. Yuan, K. Saito, C. A. Grimes, P. Kichambare, *Appl. Phys. Lett.* **2001**, 79, 3083.
- [9] S. Z. Chu, K. Wada, S. Inoue, S. Todoroki, *J. Electrochem. Soc.* **2002**, 149, B321.
- [10] Y. L. Chueh, Z. Y. Fan, K. Takei, H. Ko, R. Kapadia, A. A. Rathore, N. Miller, K. Yu, M. Wu, E. E. Haller, A. Javey, *Nano Lett.* **2010**, 10, 520.
- [11] S. Chhajed, M. F. Schubert, J. K. Kim, E. F. Schubert, *Appl. Phys. Lett.* **2008**, 93, 251108.
- [12] A. Mozalev, M. Sakairi, I. Saeki, H. Takahashi, *Electrochim. Acta* **2003**, 48, 3155.
- [13] S. Z. Chu, S. Inoue, K. Wada, S. Hishita, K. Kurashima, *Adv. Funct. Mater.* **2005**, 15, 1343.
- [14] C. T. Wu, F. H. Ko, H. Y. Hwang, *Microelectron. Eng.* **2006**, 83, 1567.
- [15] R. S. Devan, W. D. Ho, J. H. Lin, S. Y. Wu, Y. R. Ma, P. C. Lee, Y. Liou, *Cryst. Growth Des.* **2008**, 8, 4465.

- [16] Y. Y. Liou, Z. W. Wei, L. R. Wang, C. C. Liu, C. C. Kuo, C. C. Jaing, C. C. Lee, *Opt. Rev.* **2009**, *16*, 176.
- [17] J. P. Hannon, N. V. Hung, G. T. Trammell, E. Gerdau, M. Mueller, R. Ruffer, H. Winkler, *Phys. Rev. B* **1985**, *32*, 5068.
- [18] H. Kikuta, H. Toyota, W. J. Yu, *Opt. Rev.* **2003**, *10*, 63.
- [19] P. Kunze, K. Hausen, *Nature* **1971**, *231*, 392.
- [20] S. J. Wilson, M. C. Hutley, *Opt. Acta* **1982**, *29*, 993.
- [21] S. A. Boden, D. M. Bagnall, *Appl. Phys. Lett.* **2008**, *93*, 133108.
- [22] J. Zhu, Z. Yu, G. Burkhard, C. M. Hsu, S. T. Connor, Y. Xu, Q. Wang, M. McGehee, S. Fan, Y. Cui, *Nano Lett.* **2009**, *9*, 279.
- [23] S. Y. Chuang, H. L. Chen, J. Shieh, C. H. Lin, C. C. Cheng, H. W. Liu, C. C. Yu, *Nanoscale* **2010**, *2*, 799.
- [24] Y. Li, J. Zhang, S. Zhu, H. Dong, Z. Wang, Z. Sun, J. Guo, B. Yang, *J. Mater. Chem.* **2009**, *19*, 1806.
- [25] Y. F. Huang, S. Chattopadhyay, Y. J. Jen, C. Y. Peng, T. A. Liu, Y. K. Hsu, C. L. Pan, H. C. Lo, C. H. Hsu, Y. H. Chang, C. S. Lee, K. H. Chen, L. C. Chen, *Nat. Nanotechnol.* **2007**, *2*, 770.
- [26] J. Shieh, C. H. Lin, M. C. Yang, *J. Phys. D: Appl. Phys.* **2007**, *40*, 2242.
- [27] P. C. Yu, C. H. Chang, C. H. Chiu, C. S. Yang, J. C. Yu, H. C. Kuo, S. H. Hsu, Y. C. Chang, *Adv. Mater.* **2009**, *21*, 1618.
- [28] J. Q. Xi, M. F. Schubert, J. K. Kim, E. F. Schubert, M. Chen, S. Y. Lin, W. Liu, J. A. Smart, *Nat. Photonics* **2007**, *1*, 176.
- [29] T. Lohmuller, M. Helgert, M. Sundermann, R. Brunner, J. P. Spatz, *Nano Lett.* **2008**, *8*, 1429.
- [30] Y. F. Li, J. H. Zhang, S. J. Zhu, H. P. Dong, F. Jia, Z. H. Wang, Z. Q. Sun, L. Zhang, Y. Li, H. B. Li, W. Q. Xu, B. Yang, *Adv. Mater.* **2009**, *21*, 4731.

- [31] S. Walheim, E. Schaffer, J. Mlynek, U. Steiner, *Science* **1999**, 283, 520.
- [32] M. Ibn-Elhaj, M. Schadt, *Nature* **2001**, 410, 796.
- [33] X. Li, J. P. Gao, L. J. Xue, Y. C. Han, *Adv. Funct. Mater.* **2010**, 20, 259.
- [34] M. S. Park, J. K. Kim, *Langmuir* **2005**, 21, 11404.
- [35] Z. Wu, J. Walish, A. Nolte, L. Zhai, R. E. Cohen, M. F. Rubner, *Adv. Mater.* **2006**, 18, 2699.
- [36] Y. Li, F. Liu, J. Q. Sun, *Chem. Commun.* **2009**, 19, 2730.
- [37] B. Oregan, M. Gratzel, *Nature* **1991**, 353, 737.
- [38] M. Gratzel, *Nature* **2001**, 414, 338.
- [39] M. Gratzel, *Inorg. Chem.* **2005**, 44, 6841.
- [40] L. M. Peter, *J. Phys. Chem. C* **2007**, 111, 6601.
- [41] M. Gratzel, *Acc. Chem. Res.* **2009**, 42, 1788.
- [42] C. Y. Chen, M. K. Wang, J. Y. Li, N. Pootrakulchote, L. Alibabaei, C. H. Ngocle, J. D. Decoppet, J. H. Tsai, C. Gratzel, C. G. Wu, S. M. Zakeeruddin, M. Gratzel, *ACS Nano* **2009**, 3, 3103.
- [43] T. Bessho, S. M. Zakeeruddin, C. Y. Yeh, E. W. G. Diau, M. Gratzel, *Angew. Chem.Int. Ed.* **2010**, 49, 6646.
- [44] L. M. Peter, N. W. Duffy, R. L. Wang, K. G. U. Wijayantha, *J. Electroanal. Chem.* **2002**, 524, 127.
- [45] N. Kopidakis, K. D. Benkstein, J. van de Lagemaat, A. J. Frank, *J. Phys. Chem. B* **2003**, 107, 11307.
- [46] M. Law, L. E. Greene, J. C. Johnson, R. Saykally, P. D. Yang, *Nat. Mater.* **2005**, 4, 455.
- [47] G. K. Mor, K. Shankar, M. Paulose, O. K. Varghese, C. A. Grimes, *Nano Lett.* **2006**, 6, 215.
- [48] K. Zhu, N. R. Neale, A. Miedaner, A. J. Frank, *Nano Lett.* **2007**, 7, 69.

- [49] O. K. Varghese, M. Paulose, C. A. Grimes, *Nat. Nanotechnol.* **2009**, *4*, 592.
- [50] L. L. Li, C. Y. Tsai, H. P. Wu, C. C. Chen, E. W. G. Diau, *J. Mater. Chem.* **2010**, *20*, 2753.
- [51] D. Kim, A. Ghicov, P. Schmuki, *Electrochem. Commun.* **2008**, *10*, 1835.
- [52] K. Zhu, T. B. Vinzant, N. R. Neale, A. J. Frank, *Nano Lett.* **2007**, *7*, 3739.
- [53] A. B. F. Martinson, J. W. Elam, J. T. Hupp, M. J. Pellin, *Nano Lett.* **2007**, *7*, 2183.
- [54] A. B. F. Martinson, J. W. Elam, J. Liu, M. J. Pellin, T. J. Marks, J. T. Hupp, *Nano Lett.* **2008**, *8*, 2862.
- [55] T. S. Kang, A. P. Smith, B. E. Taylor, M. F. Durstock, *Nano Lett.* **2009**, *9*, 601.
- [56] N. N. Bwana, *Curr. Appl. Phys.* **2009**, *9*, 104.
- [57] L. K. Tan, M. K. Kumar, W. W. An, H. Gao, *ACS Appl. Mater. Interfaces* **2010**, *2*, 498.
- [58] S. Z. Chu, K. Wada, S. Inoue, S. Todoroki, *Chem. Mater.* **2002**, *14*, 266.
- [59] T. R. B. Foong, A. Sellinger, X. Hu, *ACS Nano* **2008**, *2*, 2250.
- [60] P. A. Liu, V. P. Singh, S. Rajaputra, *Nanotechnology* **2010**, *21*, 115303.
- [61] N. Cabrera, N. F. Mott, *Rep. Prog. Phys.* **1949**, *12*, 163.
- [62] M. M. Crouse, A. E. Miller, D. T. Crouse, A. A. Ikram, *J. Electrochem. Soc.* **2005**, *152*, D167.
- [63] A. P. Li, F. Muller, A. Birner, K. Nielsch, U. Gosele, *J. Appl. Phys* **1998**, *84*, 6023.
- [64] D. J. Werder, R. R. Kola, *Thin Solid Films* **1998**, *323*, 6.
- [65] V. Sorganov, A. Mozalov, L. Lastochkina, *J. Appl. Spectro.* **1998**, *65*, 850.
- [66] C. T. Wu, F. H. Ko, H. Y. Hwang, *Microelectron. Eng.* **2006**, *83*, 1567.
- [67] P. L. Chen, C. T. Kuo, T. G. Tsai, B. W. Wu, C. C. Hsu, F. M. Pan, *Appl. Phys. Lett.* **2003**, *82*, 2796.

- [68] J. D. Sloppy, D. D. Macdonald, E. C. Dickey, *J. Electrochem. Soc.* **2010**, *157*, C157.
- [69] J. Oh, C. V. Thompson, *Adv. Mater.* **2008**, *20*, 1368.
- [70] C. T. Wu, F. H. Ko, C. H. Lin, *Appl. Phys. Lett.* **2007**, *90*, 171911.
- [71] P. Mardilovich, P. Kornilovitch, *Nano Lett.* **2005**, *5*, 1899.
- [72] C. H. Li, K. Jordens, G. L. Wilkes, *Wear* **2000**, *242*, 152.
- [73] C. T. Wu, C. H. Lin, C. Cheng, C. S. Wu, H. C. Ting, F. C. Chang, F. H. Ko, *Chem. Mater.* **2010**, *22*, 6583.
- [74] H. J. Koo, Y. J. Kim, Y. H. Lee, W. I. Lee, K. Kim, N. G. Park, *Adv. Mater.* **2008**, *20*, 195.
- [75] S. C. Yang, D. J. Yang, J. Kim, J. M. Hong, H. G. Kim, I. D. Kim, H. Lee, *Adv. Mater.* **2008**, *20*, 1059.
- [76] Y. Kondo, H. Yoshikawa, K. Awaga, M. Murayama, T. Mori, K. Sunada, S. Bandow, S. Iijima, *Langmuir* **2008**, *24*, 547.



Chapter 3

- [1] J. E. Gordon, *UK: Pelican–Penguin*. **1976**
- [2] S. Eustis, M. A. El-Sayed, *Chem. Soc. Rev.* **2006**, *35*, 209.
- [3] K. Autumn, Y. A. Liang, S. T. Hsieh, W. Zesch, W. P. Chan, T. W. Kenny, R. Fearing, R. J. Full, *Nature* **2000**, *405*, 681.
- [4] Y. Tian, N. Pesika, H. Zeng, K. Rosenberg, B. Zhao, P. McGuiggan, K. Autumn, J. Israelachvili, *Proc. Natl. Acad. Sci. USA* **2006**, *103*, 19320.
- [5] M. Sarikaya, C. Tamerler, A. K. Y. Jen, K. Schulten, F. Baneyx, *Nat. Mater.* **2003**, *2*, 577.
- [6] W. R. Hansen, K. Autumn, *Proc. Natl. Acad. Sci. USA* **2005**, *102*, 385.
- [7] K. Autumn, Y. A. Liang, S. T. Hsieh, W. Zesch, W. P. Chan, T. W. Kenny, R. Fearing, R. J. Full, *Nature* **2000**, *405*, 681.
- [8] H. Gao, X. Wang, H. Yao, S. Gorb, E. Arzt, *Mechan. Mater.* **2005**, *37*, 275.
- [9] K. Autumn, M. Sitti, Y. A. Liang, A. M. Peattie, W. R. Hansen, S. Sponberg, T. W. Kenny, R. Fearing, J. N. Israelachvili, R. J. Full, *Proc. Natl. Acad. Sci. USA* **2002**, *99*, 12252.
- [10] W. R. Hansen, K. Autumn, *Proc. Natl. Acad. Sci. USA* **2005**, *102*, 385.
- [11] A. K. Geim, S. V. Dubonos, I. V. Grigorieva, K. S. Novoselov, A. A. Zhukov, S. Y. Shapoval, *Nat. Mater.* **2003**, *2*, 461.
- [12] H. E. Jeong, S. H. Lee, P. Kim, K. Y. Suh, *Nano Lett.* **2006**, *6*, 1508.
- [13] C. Majidi, R. E. Groff, Y. Maeno, B. Schubert, S. Baek, B. Bush, R. Maboudian, N. Gravish, M. Wilkinson, K. Autumn, R. S. Fearing, *Phys. Rev. Lett.* **2006**, *97*, 076103.
- [14] T. Kim, H. E. Jeong, K. Y. Suh, H. H. Lee, *Adv. Mater.* **2009**, *21*, 2276.
- [15] L. Ge, S. Sethi, L. Ci, P. M. Ajayan, A. Dhinojwala, *Proc. Natl. Acad. Sci. USA*

2007, 104, 10792.

- [16] L. T. Qu, L. M. Dai, M. Stone, Z. H. Xia, Z. L. Wang, *Science* **2008**, 322, 238.
- [17] S. Kim, M. Spenko, S. Trujillo, B. Heyneman, D. Santos, M. R. Cutkosky, *IEEE Trans. Robotics* **2008**, 24, 65.
- [18] A. Mahdavi, L. Ferreira, C. Sundback, J. W. Nichol, E. P. Chan, D. J. D. Carter, C. J. Bettinger, S. Patanavanich, L. Chignozha, E. Ben-Joseph, A. Galakatos, H. Pryor, I. Pomerantseva, P. T. Masiakos, W. Faquin, A. Zumbuehl, S. Hong, J. Borenstein, J. Vacanti, R. Langer, J. M. Karp, *Proc. Natl. Acad. Sci USA* **2008**, 105, 2307.
- [19] W. K. Cho, I. S. Choi, *Adv. Funct. Mater.* **2008**, 18, 1089.
- [20] D. S. Kim, H. S. Lee, J. Lee, S. Kim, K. H. Lee, W. Moon, T. H. Kwon, *Microsys. Technol.* **2007**, 13, 601.
- [21] B. Yurdumakan, N. R. Raravikar, P. M. Ajayan, A. Dhinojwala, *Chem. Commun.* **2005**, 3799.
- [22] S. Kim, M. Sitti, C. Y. Hui, R. Long, A. Jagota, *Appl. Phys. Lett.* **2007**, 91, 161905.
- [23] A. D. Campo, C. Greiner, E. Arzt, *Langmuir* **2007**, 23, 3495.
- [24] A. Jagota, S. J. Bennison, *Integr. Comp. Biol.* **2002**, 42, 1140.
- [25] M. P. Murphy, B. Aksak, M. Sitti, *Small* **2009**, 5, 170.
- [26] B. Aksak, M. P. Murphy, M. Sitti, *Langmuir* **2007**, 23, 3322.
- [27] J. Lee, R. S. Fearing, K. Komvopoulos, *Appl. Phys. Lett.* **2008**, 93, 191910.
- [28] L. Qu, L. Dai, *Adv. Mater.* **2007**, 19, 3844.
- [29] C. T. Wirth, S. Hofmann, J. Robertson, *Diamond Relat. Mater.* **2008**, 17, 1518.
- [30] Y. Zhao, T. Tong, L. Delzeit, A. Kashani, M. Meyyappan, A. Majumdar, *J. Vac. Sci. Technol. B* **2006**, 24, 331.
- [31] R. N. Wenzel, *Ind. Eng. Chem.* **1936**, 28, 988.

- [32] D. Oner, T. J. McCarthy, *Langmuir* **2000**, *16*, 7777.
- [33] A. Lafuma, D. Quere, *Nat. Mater.* **2003**, *2*, 457.
- [34] R. Furstner, W. Barthlott, C. Neinhuis, P. Walzel, *Langmuir* **2005**, *21*, 956.
- [35] W. Barthlott, C. Neinhuis, *Planta* **1997**, *202*, 1.
- [36] K. L. Johnson, K. Kendall, A. D. Roberts, *Proc. R. Soc. A* **1971**, *324*, 301.
- [37] E. Arzt, S. Gorb, R. Spolenak, *Proc. Natl. Acad. Sci. USA* **2003**, *100*, 10603.
- [38] K. Autumn, A. Dittmore, D. Santos, M. Spenko, M. Cutkosky, *J. Exp. Biol.* **2006**, *206*, 3569.
- [39] B. X. Zhao, N. Pesika, H. B. Zeng, Z. S. Wei, Y. F. Chen, K. Autumn, K. Turner, J. Israelachvili, *J. Phys. Chem. B* **2009**, *113*, 3615.
- [40] N. J. Glassmaker, A. Jagota, C. Y. Hui, J. Kim, *J. R. Soc. Interface* **2004**, *1*, 23.
- [41] C. Y. Hui, A. Jagota, Y. Y. Lin, E. J. Kramer, *Langmuir* **2002**, *18*, 1394.
- [42] H. Yao, H. Gao, *J. Mech. Phys. Solids* **2006**, *54*, 1120.
- [43] H. Gao, H. Yao, *Proc. Natl. Acad. Sci. USA* **2004**, *101*, 7851.
- [44] F. Keller, M. S. Hunter, D. L. Robinson, *J. Electrochem. Soc.* **1953**, *100*, 411.
- [45] M. S. Hunter, P. Fowle, *J. Electrochem. Soc.* **1954**, *101*, 481.
- [46] G. E. Thompson, G. C. Wood, *Nature* **1981**, *290*, 230.
- [47] M. M. Lohregel, *Mater. Sci. Eng. R* **1993**, *11*, 243.
- [48] J. W. Diggle, T. C. Downie, C. W. Goulding, *Chem. Rev.* **1969**, *69*, 365.
- [49] G. E. Thompson, R. C. Furneaux, G. C. Wood, J. A. Richardson, J. S. Goode, *Nature* **1978**, *272*, 433.
- [50] G. C. Wood, J. P. O'Sullivan, *Electrochim. Acta* **1970**, *15*, 1865.
- [51] A. P. Li, F. Muller, A. Birner, K. Nielsch, U. Gosele, *J. Appl. Phys.* **1998**, *84*, 6023.
- [52] J. E. Houser, K. R. Hebert, *Nat. Mater.* **2009**, *8*, 415.
- [53] C. R. Martin, *Science* **1994**, *266*, 1961.

- [54] S. R. Nicewarner-Pena, R. G. Freeman, B. D. Reiss, L. He, D. J. Pena, I. D. Walton, R. Cromer, C. D. Keating, M. J. Natan, *Science* **2001**, *294*, 137.
- [55] S. B. Lee, D. T. Mitchell, L. Trofin, T. K. Nevanen, H. Soderlund, C. R. Martin, *Science* **2002**, *296*, 2198.
- [56] H. Masuda, F. Hasegawa, S. Ono, *J. Electrochem. Soc.* **1997**, *144*, L127.
- [57] H. Masuda, K. Fukuda, *Science* **1995**, *268*, 1466.
- [58] F. Li, L. Zhang, R. M. Metzger, *Chem. Mater.* **1998**, *10*, 2470.
- [59] S. Shingubara, K. Morimoto, H. Sakaue, T. Takahagi, *Electrochem. Solid-State Lett.* **2004**, *7*, E15.
- [60] K. Nielsch, J. Choi, K. Schwirn, R. B. Wehrspohn, U. Gosele, *Nano Lett.* **2002**, *2*, 677.
- [61] W. Lee, R. Ji, U. Gosele, K. Nielsch, *Nat. Mater.* **2006**, *5*, 741.
- [62] P. Csokan, C. C. Sc, *Electroplat. Met. Finish.* **1962**, *15*, 75.
- [63] E. Lichtenberger, A. Domony, P. Csokan, *Mechanics of Materials* **1960**, *11*, 701.
- [64] Y. Li, M. Zheng, L. Ma, W. Shen, *Nanotechnology* **2006**, *17*, 5101.
- [65] W. Lee, K. Schwirn, M. Steinhart, E. Pippel, R. Scholz, U. Gosele, *Nat. Nanotechnol.* **2008**, *3*, 234.
- [66] V. P. Parkhutik, V. I. Shershulsky, *J. Phys. D: Appl. Phys.* **1992**, *25*, 1258.
- [67] S. Z. Chu, K. Wada, S. Inoue, M. Isogai, A. Yasumori, *Adv. Mater.* **2005**, *17*, 2115.
- [68] T. Yanagishita, K. Yasui, T. Kondo, Y. Kawamoto, K. Nishio, H. Masuda, *Chem. Lett.* **2007**, *36*, 530.
- [69] W. Lee, R. Ji, U. Gosele, K. Nielsch, *Nat. Mater.* **2006**, *5*, 741.
- [70] K. Autumn, C. Majidi, R. E. Groff, A. Dittmore, R. Fearing, *J. Exp. Biol.* **2006**, *209*, 3558.
- [71] N. J. Glassmaker, A. Jagota, C. Y. Hui, J. Kim, *J. R. Soc. Interface* **2004**, *1*, 23.

[72] C. Y. Hui, A. Jagota, Y. Y. Lin, E. J. Kramer, *Langmuir* **2002**, *18*, 1394.

[73] H. Yao, H. Gao, *J. Mech. Phys. Solids* **2006**, *54*, 1120.

[74] H. J. Gao, H. M. Yao, *Proc. Natl. Acad. Sci. USA* **2004**, *101*, 7851.



Chapter 4

- [1] H. C. Von Baeyer, *Sciences-New York* **2000**, 40, 12.
- [2] R. Blossey, *Nat. Mater.* **2003**, 2, 301.
- [3] W. Barthlott, C. Neinhuis, *Planta* **1997**, 202, 1.
- [4] N. A. Patankar, *Langmuir* **2003**, 19, 1249.
- [5] Z. Yoshimitsu, A. Nakajima, T. Watanabe, K. Hashimoto, *Langmuir* **2002**, 18, 5818.
- [6] D. Quere, *Physica A* **2002**, 313, 32.
- [7] M. H. Sun, C. X. Luo, L. P. Xu, H. Ji, O. Y. Qi, D. P. Yu, Y. Chen, *Langmuir* **2005**, 21, 8978.
- [8] K. Koch, B. Bhushan, W. Barthlott, *Soft Matter* **2008**, 4, 1943.
- [9] G. Ibarz, L. Dahne, E. Donath, H. Mohwald, *Adv. Mater.* **2001**, 13, 1324.
- [10] I. Bontidean, A. Kumar, E. Csoregi, I. Y. Galaev, B. Mattiasson, *Angew. Chem. Int. Ed.* **2001**, 40, 2676.
- [11] R. Furstner, W. Barthlott, C. Neinhuis, P. Walzel, *Langmuir* **2005**, 21, 956.
- [12] A. Lafuma, D. Quere, *Nat. Mater.* **2003**, 2, 457.
- [13] B. Bhushan, Y. C. Jung, K. Koch, *Langmuir* **2009**, 25, 3240.
- [14] I. P. Parkin, R. G. Palgrave, *J. Mater. Chem.* **2005**, 15, 1689.
- [15] J. De Coninck, M. J. de Ruijter, M. Voue, *Curr. Opin. Colloid Interface Sci.* **2001**, 6, 49.
- [16] T. Onda, S. Shibuichi, N. Satoh, K. Tsujii, *Langmuir* **1996**, 12, 2125.
- [17] M. Nosonovsky, B. Bhushan, *Adv. Funct. Mater.* **2008**, 18, 843.
- [18] P. G. de Gennes, F. Brochard-Wyart, D. Quere, *Capillarity and Wetting Phenomena-Drops, Bubbles, Pearls, Waves*; Springer: New York, 2002; p 216.
- [19] R. N. Wenzel, *Ind. Eng. Chem.* **1936**, 28, 988.

- [20] A. Cassie, S. Baxter, *Trans. Faraday Soc.* **1944**, *40*, 546.
- [21] L. Feng, Y. Zhang, J. Xi, Y. Zhu, N. Wang, F. Xia, L. Jiang, *Langmuir* **2008**, *24*, 4114.
- [22] J. Xi, L. Jiang, *Ind. Eng. Chem. Res.* **2008**, *47*, 6354.
- [23] L. Feng, S. Li, Y. Li, H. Li, L. Zhang, J. Zhai, Y. Song, B. Liu, L. Jiang, D. Zhu, *Adv. Mater.* **2002**, *14*, 1857.
- [24] (a) T. Sun, L. Feng, X. Gao, L. Jiang, *Acc. Chem. Res.* **2005**, *38*, 644. (b) X. Feng, L. Jiang, *Adv. Mater.* **2006**, *18*, 3063.
- [25] S. T. Wang, Y. L. Song, L. Jiang, *J. Photochem. Photobiol. C* **2007**, *8*, 18.
- [26] M. Callies, D. Quere, *Soft Matter* **2005**, *1*, 55.
- [27] X. Zhang, F. Shi, J. Niu, Y. Jiang, Z. Wang, *J. Mater. Chem.* **2008**, *18*, 621.
- [28] P. Roach, N. J. Shirtcliffe, M. I. Newton, *Soft Matter* **2008**, *4*, 224.
- [29] L. Gao, T. J. McCarthy, *J. Am. Chem. Soc.* **2006**, *128*, 9052.
- [30] Y. C. Jung, B. Bhushan, *Nanotechnology* **2006**, *17*, 4970.
- [31] Z. Yoshimitsu, A. Nakajima, T. Watanabe, K. Hashimoto, *Langmuir* **2002**, *18*, 5818.
- [32] X. Song, J. Zhai, Y. Wang, L. Jiang, *J. Phys. Chem. B* **2005**, *109*, 4048.
- [33] M. Jin, X. Feng, L. Feng, T. Sun, J. Zhai, T. Li, L. Jiang, *Adv. Mater.* **2005**, *17*, 1977.
- [34] Y. Zheng, X. F. Gao, L. Jiang, *Soft Matter* **2007**, *3*, 178.
- [35] L. Gao, T. J. McCarthy, *Langmuir* **2006**, *22*, 2966.
- [36] X. F. Gao, X. Yao, L. Jiang, *Langmuir* **2007**, *23*, 4886.
- [37] Z. Cheng, L. Feng, L. Jiang, *Adv. Funct. Mater.* **2008**, *18*, 3219.
- [38] X. Hong, X. F. Gao, L. Jiang, *J. Am. Chem. Soc.* **2007**, *129*, 1478.
- [39] D. Huh, A. H. Tkaczyk, J. H. Bahng, Y. Chang, H. Wei, J. B. Grotberg, C. J. Kim, K. Kurabayashi, S. Takayama, *J. Am. Chem. Soc.* **2003**, *125*, 14678.

- [40] W. Satoh, H. Hosono, H. Suzuki, *Anal. Chem.* **2005**, *77*, 6857.
- [41] N. Yoshida, Y. Abe, H. Shigeta, A. Nakajima, H. Ohsaki, K. Hashimoto, T. Watanabe, *J. Am. Chem. Soc.* **2006**, *128*, 743.
- [42] P. Dubois, G. Marchand, Y. Fouillet, J. Berthier, T. Douki, F. Hassine, S. Gmouh, M. Vaultier, *Anal. Chem.* **2006**, *78*, 4909.
- [43] K. A. Wier, T. J. McCarthy, *Langmuir* **2006**, *22*, 2433.
- [44] N. Zhao, Q. Xie, X. Kuang, S. Wang, Y. Li, X. Lu, S. Tan, J. Shen, X. Zhang, Y. Zhang, J. Xu, C. C. Han, *Adv. Funct. Mater.* **2007**, *17*, 2739.
- [45] A. Lafuma, D. Quere, *Nat. Mater.* **2003**, *2*, 457.
- [46] D. Quere, A. Lafuma, J. Bico, *Nanotechnology* **2003**, *14*, 1109.
- [47] Y. Lai, X. F. Gao, H. Zhuang, J. Huang, C. Lin, L. Jiang, *Adv. Mater.* **2009**, *21*, 3799.
- [48] J. B. West, *J. Appl. Physiol.* **1999**, *87*, 1543.
- [49] S. Boduroglu, M. Cetinkaya, W. J. Dressick, A. Singh, M. C. Demirel, *Langmuir* **2007**, *23*, 11391.
- [50] J. Xi, L. Jiang, *Ind. Eng. Chem. Res.* **2008**, *47*, 6354.
- [51] N. Bowden, S. Brittain, A. G. Evans, J. W. Hutchinson, G. M. Whitesides, *Nature* **1998**, *393*, 146.
- [52] H. M. Whitney, L. Chittka, T. J. A. Bruce, B. J. Glover, *Current Biology* **2009**, *19*, 1.
- [53] N. D. Denkov, O. D. Velev, P. A. Kralchevsky, I. B. Ivanov, H. Yoshimura, K. Nagayama, *Nature* **1993**, *361*, 26.
- [54] L. Feng, Y. Zhang, J. Xi, Y. Zhu, N. Wang, F. Xia, L. Jiang, *Langmuir* **2008**, *24*, 4114.